



**A new broadband, interferometric scanning near-field
spectroscopy technique for probing the time-domain
response of single nanoparticles**

An der Fakultät für Mathematik und Naturwissenschaften
der Carl von Ossietzky Universität Oldenburg
zur Erlangung des Grades und Titels eines
Doktors der Naturwissenschaften (Dr. rer. nat)
im Fach Physik
Dissertation

von

Frau Jinxin Zhan

geboren am 19.03.1989 in Shanxi, China

Gutachter:

Prof. Dr. Christoph Lienau, Carl von Ossietzky Universität Oldenburg

Weitere Gutachter:

Prof. Dr. Volker Deckert, Friedrich-Schiller-Universität Jena

Tag der Disputation: 15.09.2023

Abstract

This thesis focuses on investigating the localized mode profile, complex near-field response function, and field dynamics of individual dielectric nanostructures. The experiment is realized by a scattering-type scanning near-field optical microscope (s-SNOM) combined with spectral interferometry: the incident broad bandwidth light is divided in two paths by a beam splitter. One is focused to a vibrating tip (typically at around 30 kHz) in the vicinity of the sample, denoted as sample arm, and the other is reflected by a mirror denoted as the reference arm. The tip scattered field and the broadband reference field combine at the beam splitter, and the interference is directly measured in spectral domain by a fast line camera detector with a capture frequency that is faster than the typical 30 kHz tip modulation.

We firstly investigate the optical properties of nanostructures of antimony sulfide (Sb_2S_3), a direct-bandgap semiconductor material that has recently sparked considerable interest as a thin film solar cell absorber. Fabrication from a nanoparticle ink solution and two- and three-dimensional nanostructuring with pattern sizes down to 50 nm have recently been demonstrated. Insight into the yet unknown nanoscopic optical properties of these nanostructures is highly desired for their future applications in nanophotonics. We implement a spectrally broadband scattering-type near-field optical spectroscopy technique to study individual Sb_2S_3 nanodots with a 20-nm spatial resolution, covering the range from 700 to 900 nm. We show that in this below-bandgap range, the Sb_2S_3 nanostructures act as high-refractive-index, low-loss waveguides with mode profiles close to those of idealized cylindrical waveguides, despite a considerable structural disorder. In combination with their high above-bandgap absorption, this makes them promising candidates for applications as dielectric metamaterials, specifically for ultrafast photoswitching.

Metallic, semiconducting and dielectric nanoparticles form outstanding tools for localizing light on the nanoscale. Their optical shape resonances confine light in certain localized modes and in spectral regions, largely tunable by varying the size, shape or composition of the particle. Often, the lifetimes of the optical resonance of those particles are so short, in the range of few femtoseconds, that direct time-resolved measurements of their

localized optical near-fields are highly challenging. Here, we employ the broad-bandwidth interference SNOM to reconstruct the complex response function of a single nanostructure in the time domain and with nanometer-spatial resolution. We demonstrate this approach by analyzing single MAPbI₃ perovskite nanoparticles, promising new candidates for nanoscale light sources. Their optical spectra are expected to feature distinct Fano resonances, arising from the coupling of excitons to the Mie resonances of the particles. Here, we provide direct evidence for these Fano resonances by measuring amplitude and phase of their local optical near-field with high spatial and spectral resolution. Our technique provides a general approach for measuring the response functions of nanostructures in the visible and near-infrared spectral range with femtosecond temporal and nanometer spatial resolution.

Key words: near-field spectroscopy, scattering-type near-field optical microscopy, local density of state, Fano resonance, field dynamics

1 Introduction	1
2 Theoretical background	9
2.1 Optical antenna	9
2.1.1 Rayleigh scattering and Mie scattering	10
2.1.2 Dielectric function of metallic and dielectric material	14
2.1.3 Metallic and dielectric optical antenna	16
2.2 Optical waveguide	19
2.3 Optical local density of state	24
2.3.1 Scanning tunneling microscope	24
2.3.1.1 Tunneling a rectangular potential barrier	25
2.3.1.2 Tunneling current	27
2.3.2 Optical LDOS	30
2.4 Point dipole model	34
2.5 Homodyne and Heterodyne detection	43
3 Experimental setup and data processing	47
3.1 Overview over the optical setup	47
3.2 Tip fabrication and vibration	49
3.3 Tuning fork	52
3.4 Near-field spectroscopy with homodyne detection	54
3.4.1 Fast camera data	54
3.4.2 Spectral interference simulation	56
3.4.3 Experimental spectral data processing	64
3.4.4 Demodulated spectral interferogram	66
4 Spatial and spectral mode mapping of a dielectric nanodot	71
4.1 Sample preparation	71
4.2 Near-field imaging	73
4.2.1 Near-field contrast	73

4.2.2 Spatial resolution	77
4.2.3 Influence of surface roughness	78
4.2.4 Calculation of eigen modes in Sb_2S_3 nanodot	80
4.3 Spectral response of Sb_2S_3 waveguide modes	86
4.3.1 Near-field spectrum and dipole model simulation	87
4.3.2 Spatially resolved near-field spectrum	91
5 Time-domain response of single Halide Perovskite nanoparticles	99
5.1 Sample preparation	99
5.2 Near-field spectra	104
5.2.1 Measurement results	104
5.3.3 Fano interference in a MAPbI_3 nanoparticle	113
6 Conclusion and Outlook	123

1 Introduction

The beauty of light is ascribable to the fact that its energy lies in the energy range of electric and vibrational transitions in matter.¹ This enables optical techniques that are not restricted to imaging, but that also enable studying structural and dynamic properties of materials by analyzing the interaction between light and matter. Additional advantages of optical techniques, such as sensitivity, flexibility, and relatively low cost, brought about a rapid development of optical spectroscopy. However, traditional optical techniques can not satisfy the demand of exploring nanoscale objects due to the diffraction limit, and the characterization of the spectral properties of single nanostructures or hybrid nanosystems is far out of reach with today's possibilities. Nanoplasmonics, i. e., studying the electromagnetic response of metal nanostructures, is a rapidly growing field of research. On the one hand, the realization and design of metallic nanostructures with tunable plasmon resonances, as well as tuning the dynamics of surface plasmon polariton excitations have great potential for creating nano-optical devices with novel functionalities. On the other hand, dielectric nanostructures offer an alternative means to light manipulation on a spatial scale of a few to hundred nanometers, such as Rayleigh or Mie scattering by small particles or waveguiding in switchable semiconductor nanostructures. All these processes call for an optical spectroscopy with nanometer scale spatial resolution.

In traditional optical microscopy, the spatial resolution is limited by the wavelength of light, as formulated by Abbe:²

$$d = 0.61\lambda/n \sin(\theta) \quad (1)$$

Abbe's equation states that the minimum resolvable distance, d , is on the order of half of the incident light wavelength λ . $n \sin(\theta)$ is the numerical aperture (NA) of the used focusing objective and can be optimized to 1.4 by operating in a high-refractive-index medium such as oil. Altogether, for light in the visible spectral range, the spatial resolution of an optical microscope can, in principle, be optimized to about 200 nm.

The fundamental reason for this limitation lies in Fourier optics. According to the uncertainty principle, the lateral size of a particle, Δr_{\parallel} , and its wave vector spectrum Δk_{\parallel} fulfill:

$$\Delta r_{\parallel} \geq \frac{1}{2 \Delta k_{\parallel}} \quad (2)$$

It means that a smaller lateral size of a particle corresponds to a wider spread of its wave vector spectrum along the same dimension. Since the wave vector components are limited by $k = \sqrt{k_{\parallel}^2 + k_{\perp}^2} = 2\pi/\lambda$, a large lateral wave vector signifies a squeezed orthogonal component. When a particle is small in lateral direction (r_{\parallel} is a few or several tens of nanometers), its wave vector spectrum in the relevant direction, k_{\parallel} , will even exceed k . In this case, the associated k_{\perp}^2 becomes negative, resulting in an imaginary perpendicular wave vector k_{\perp} . Such a wave is bound to the surface of the particle and decays quickly away from the surface. This evanescent wave does not propagate, therefore is not detectable in the signal collected in conventional microscopy. Instead, one way to access this information is bringing a probe close enough to the surface to access the near field within its decay length.

Scanning near-field optical microscopy (SNOM) makes use of this principle to provide an option to construct nanoscale images using near-field light. The possibility was firstly raised by Synge in 1928.³ He proposed to produce a minute aperture with a diameter much smaller than wavelength of the light, and illuminate it from the backside. The so created new light source, whose dimension is determined by the aperture size, is then placed at a very close distance above the sample. The aperture-sample distance is kept constant, while the aperture is raster-scanned across the sample and the reflected or transmitted light is recorded, enabling surface imaging. In the described scheme, the lateral resolution would be determined by the aperture size rather than the wavelength of the light. However, neither fabricating such a minute aperture nor controlling the small aperture-sample distance was realizable at that time. Synge's idea was not experimentally verified until the end of the 19th century. Benefiting from tremendous progress in nanotechnology and from the invention of scanning probe microscopy,⁴ the

first subwavelength images with visible light were reported in 1984 independently by Lewis *et al.* and Pohl *et al.* almost at the same time.^{5, 6} Following the subsequent experimental realization of aperture SNOM,⁷⁻⁹ a great amount of high resolution measurements was implemented, which more importantly discovered previously unknown properties in the new sub-wavelength dimension for various samples. In 1993, a single dye molecule was imaged, and the dipole transition orientation was studied.¹⁰ Soon after that, the emission of single molecules was observed,¹¹ and single molecule dynamics were probed¹².

The above described first near-field images were achieved with aperture probes, glass fibers that are manufactured to a sharp tip and often covered with a metal film with a nanometer-sized opening for light transmission. These aperture tips, however, impose a significant limitation due to their finite aperture size and light transmission. To relieve that limitation, an alternative scheme of apertureless SNOM system (or scattering SNOM (sSNOM)) was demonstrated by utilizing a nanoscaled scattering tip instead of an aperture tip.¹³⁻¹⁷ Metallic tips are preferentially used because of their high scattering cross section, excellent light confinement, and field enhancement characteristics. The most common application of sSNOM is to plasmonic nanostructures and metamaterials, where they are used for nanoscale visualization of field and charge distributions.¹⁸⁻²⁸ Owing to the broad in-plane momentum range of the tip dipole, different surface polariton properties can be inferred from sSNOM measurements, such as the dispersion of polaritons in van der Waals crystals, or the anisotropy of phonon polaritons.²⁹⁻³⁴ Besides plasmonic nanostructures, sSNOM has been applied to mapping the evanescent field distribution of a multitude of dielectric samples, such as waveguides and microresonators,^{35, 36} photonic crystal microcavities,³⁷ and, more recently, all-dielectric nanostructures.^{38, 39}

Despite the remarkable performance improvement of sSNOM, however, there remains a challenge due to the near-field light scattered from the small tip being dominated by a large background signal. This undesired background light may originate from the tip shaft or the sample and therefore it may cause artefacts in the detected signal and complicate retrieval of information from the sample. In principle, the background signal can be largely

avoided by employing adiabatic nanofocusing to SNOM.⁴⁰⁻⁴⁵ This technique is an active topic of current research and first applications in broadband light scattering and time-resolved spectroscopy are currently pursued in different laboratories,^{40, 46} however, it's not widely employed because its application is difficult. In a more common approach, the near-field signal is modulated by oscillating the metal tip with a frequency in the 10-kHz-range.⁴⁷ Due to the highly nonlinear dependence of the scattered near-field signal on the tip-sample distance, higher harmonics of the modulation frequency are found in the signal. Even though the near-field-to-background ratio is improved by demodulating at higher harmonics, a complete suppression of the unwanted background is challenging. Generally, the light field components that are scattered from the near field, from the tip apex and from the tip shaft interfere and lead to the detection of a mixed intensity signal that cannot be disentangled, because mixing occurs at the electric field level.⁴⁸⁻⁵⁰ In order to enable such discrimination of the different contributions to the signal and to eliminate the background signal, amplification of the near-field signal by mixing of the scattered signal with a well-controlled reference wave was introduced. A simple way to achieve such amplification is by homodyne mixing via a stable Michelson interferometer.

As the spatial resolution was improved to the nanometer scale, broadband spectroscopy combined with sSNOM also gained great popularity. Infrared (IR) near-field spectroscopy has been broadly applied to extract chemical and structural information in the last decades.⁵¹⁻⁵⁷ However, in the visible spectral range broad-bandwidth near-field spectroscopy remains challenging. this requires efficient background suppression based on tip-sample distance modulation and near-field enhancement using homodyne or heterodyne mixing.^{47-50, 58} In this work, I propose and experimentally demonstrate a scanning near-field optical spectroscopy technique with an interferometrical detection scheme over a broad bandwidth in the visible/near-infrared, and I obtain nearly background-free near-field spectra in the spectral range from 720 to 900 nm. This new method is applied to the investigation of two typical high-refractive-index nanostructures, namely isolated stibnite (antimony sulfide, Sb_2S_3) nanodots and halide perovskite nanoparticles MAPbI_3 .

Very recently, nanoparticles of high-index dielectric materials have gained attention, because they offer an alternative means to light manipulation well below the diffraction limit.⁵⁹ Compared to metallic nanoparticles, they show reduced Ohmic losses at visible frequencies and they often are compatible with complementary metal oxide semiconductor (CMOS) fabrication processes, which makes them favorable candidates for some integrated optical devices like waveguides in photonic circuitry. Instead of free electrons and electric fields concentrating at metal-dielectric interfaces, in all-dielectric nanoparticles electric dipoles and low-order multipoles give rise to Mie-type resonances and concurrent spatial light localization. Recent investigations of high-index dielectric nanoparticles arose in particular due to their capability of supporting dielectric as well as magnetic resonances, which can interfere and create unusual spatial and spectral scattering patterns and which may become a key for realizing devices and surfaces with novel optical properties⁵⁹⁻⁶². For example, stibnite (antimony sulfide, Sb_2S_3) is currently gaining increasing attention as an emerging photovoltaic material.^{63, 64} The combination of a direct bandgap and a high absorption coefficient leads to considerable photoconductivity, enabling applications in optoelectronics.⁶⁵ Power conversion efficiencies of up to 7.5% have been demonstrated for an Sb_2S_3 -sensitized heterojunction solar cell.⁶⁶ As recently demonstrated, nanopatterning via direct electron beam lithography (EBL) writing enables the creation of 2D and 3D nanometric structures of various shapes.⁶⁵ The availability of easy structuring, together with the possibility of changing the refractive index on an ultrafast time scale by injecting free carriers, makes the material an interesting candidate for the realization of photoswitchable metasurfaces.⁶⁷

As a second example of dielectric nanoparticles with intriguing properties, we turn to halide perovskite nanocrystals. These hybrid perovskites support excitonic states at room temperature, have refractive indices ($n = 2-3$) high enough for the efficient excitation of Mie resonances, combined with low losses at the exciton wavelength, a chemically tunable band gap,⁶⁸ high defect tolerance,⁶⁹ and a high quantum yield (more than 30%⁷⁰) of photoluminescence. These properties make them extremely interesting candidates for effective nanoscale light sources.

Using our nano-spectroscopy, I found that in the below-bandgap range, the Sb_2S_3 nanostructures act as high-refractive-index, low-loss waveguides with mode profiles close to those of idealized cylindrical waveguides. In the above-bandgap range of the hybrid perovskite nanoparticles, the exciton is found to be coupled to the geometry-driven Mie resonance, displaying a Fano-shaped resonance. Using the interferometric spectroscopy approach developed in this these, the amplitude as well as the phase of the Fano-type resonance are retrieved.

Outline

This thesis is organized as follows:

Chapter 1 gives a brief introduction of nano-optics near-field spectroscopy background.

Chapter 2 covers the theoretical background in three aspects. From the material point of view, optical properties of two common categories of nanostructures, optical antenna and waveguide, are discussed. Concerning the relationship between SNOM measurement and sample property, near-field signal explanation methods, optical Local Density of State (LDOS) and dipole model, are outlined. At last, we introduce the working principle, on the field level, of homodyne and heterodyne based SNOM technique.

Chapter 3 presents the home built experimental setup. We employ a scattering SNOM scheme and a gold tip as the near-field prober. Based on this, a homodyne interferometry is incorporated to achieve spectrally broadband scattering-type near-field optical spectroscopy in visible range. Wherein the spectrum demodulation from a fast line camera recording is carefully discussed. Moreover, we propose another approach to near-field spectrum realized by Fourier spectroscopy, and compared performances of two approaches.

Chapter 4 and chapter 5 discuss the broad bandwidth near-field spectroscopy application on dielectric nanostructures. In chapter 4, eigen modes of individual Sb_2S_3 nanodot are observed with 10 nm spatial resolution by the near-field imaging, which is demonstrated to resemble the low order waveguide modes of a cylindrical optical fiber. Moreover, the spectral mode properties are explored by the near-field spectroscopy. These modes are seen across the entire bandwidth of our laser. Chapter 5 employ our SNOM technique combined with spectral interference technique to resolve the time structure of optical near-fields from the hot spots of a single MAPbI_3 perovskite nanoparticle with high spatial resolution. Here, we provide direct evidence for a Fano resonance of individual MAPbI_3 nanoparticles by measuring amplitude and phase of their local optical near-field with high spatial and spectral resolution. We identify a destructive interference dip in the time

structure of the reconstructed optical near-field as the distinct signature of these Fano resonances.

Chapter 6 briefly summarizes the results and gives a outlook on future applications of the work.

2 Theoretical background

This chapter introduces a theoretical description of the optical response of two kinds of nanoparticles to light in free space and in a SNOM system, and then describes the technical reconstruction of nanostructural information from sSNOM signal. To describe the optical property of a nanoparticle, Maxwell's equations for electric and magnetic field vectors are generally solved under certain boundary condition and constitutive relations.⁷¹ Accordingly, the basic properties of two types of nanostructures, dielectric optical antenna and cylindrical waveguide, are discussed. In weak probe-sample coupling regime, the scattered near-field signal is supposed to probe the optical local density of state in the nanoparticle region which is mainly the superposition of eigen modes. For particles close to probe size scale, point-dipole model is more suitable to describe the probe and sample near-field interaction, in which the coupling system response is analytically formulated. At last, from technical point of view, we will analyze the signal on the field level to identify the near-field and background-field signal contributions for a typical sSNOM and sSNOM combined with homodyne and heterodyne interferometry.

2.1 Optical antenna

Optical antenna, as an analogy of antenna in radio wave or microwave regime, refers to structures efficiently concentrating free-space light wave into a nanoscale volume, and are constructed from subwavelength scale structures. The conventional ways to manipulate light is realized by altering its phase, amplitude, and polarization using lens, prism, and birefringent or diffractive elements. All these means shape optical wave fronts using the propagation effect, therefore cannot surpass diffraction limit to control fields in subwavelength scale. In contrast, the optical antenna structure provides efficient means to manipulate light at the nanoscale. These nanostructures have been demonstrated to be able to enhance spectroscopic techniques, such as surface-enhanced Raman scattering (SERS)⁷²⁻⁸² and enhanced fluorescence spectroscopy,⁸³⁻⁹⁷ strong coupling,^{98, 99} ultrafast emission,¹⁰⁰⁻¹⁰² photovoltaics,^{103, 104} photodetection,¹⁰⁵ and biosensors.^{106, 107}

To fundamentally understand the optical response of nano-antennas, we need to study the scattering of electromagnetic waves by a structure. As stated in [38], the underlying physics of scattering is the same for all systems.¹⁰⁸ Matter is composed of discrete electric charges: electrons and protons. When an obstacle is illuminated by an electromagnetic wave, electric charges in the obstacle are driven into oscillatory motion by the electric field of the incident wave. The accelerated electric charges then radiate electromagnetic energy in all directions. The scattering of electromagnetic waves by an obstacle is the superposition of incident wave and the re-radiated wave:

$$\text{Scattering} = \text{excitation} + \text{reradiation}$$

In addition to reradiating electromagnetic energy, the excited elementary charges may transform part of the incident electromagnetic energy into other forms, which is absorption.¹⁰⁸

2.1.1 Rayleigh scattering and Mie scattering

Literally, the scattering of light includes elastic scattering and inelastic scattering. Elastic scattering means that the wavelength of the scattered light is not changed in comparison to the incident light. It is categorized in terms of two theoretical frameworks, Rayleigh scattering and Mie scattering. Rayleigh scattering¹⁰⁹⁻¹¹¹ (named after John William Strutt, 3rd Baron Raileigh) refers to the elastic scattering of light from single atomic and molecular particles whose diameter is much smaller than wavelength of light. In contrast, Mie scattering¹¹² occurs when the scattering particle size is comparable to light wavelength. A parameter for distinguishing two kinds of particles is given by $\alpha = \frac{2\pi a}{\lambda}$, where a is the circumference of a particle and λ is the wavelength of incident radiation in the medium. The criterion for Rayleigh scattering is $\alpha \ll 1$, and for Mie scattering is $\alpha \gg 1$. The specific scattering coefficient of a sphere has been discussed in a variety of books such as [Kerker Milton, 1969, Bohren and Huffman, 1983, Kreibig and Vollmer, 1995]. Here we illustrate the basic deduction clue and the main conclusions.¹⁰⁸

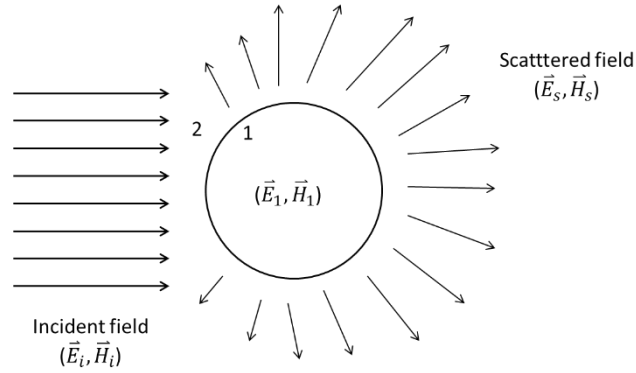


Figure 2.1 The incident field \vec{E}_i, \vec{H}_i gives rise to a field inside a sphere \vec{E}_1, \vec{H}_1 and a scattered field \vec{E}_s, \vec{H}_s in the surrounding medium.

For simplicity, we take a spherical particle as the scatterer and discuss the Maxwell's equations in x dimension. The problem is sketched in figure 2.1: A spherical particle with specified size, shape, and optical properties is embedded in a homogeneous medium. When illuminated by a polarized monochromatic wave, determine the electromagnetic field scattered by the sphere.

The incident field is denoted by (\vec{E}_i, \vec{H}_i) , and the scattered field is (\vec{E}_s, \vec{H}_s) , where $\vec{E}_i = E_0 e^{i(\vec{k} \cdot \vec{x} - \omega t)}$ and $\vec{H}_i = H_0 e^{i(\vec{k} \cdot \vec{x} - \omega t)}$ with k and ω are wave vector and light wave frequency in medium. Firstly, the fields satisfy the Maxwell equation:

$$\nabla \cdot \vec{E} = 0 \quad (2.1)$$

$$\nabla \cdot \vec{H} = 0 \quad (2.2)$$

$$\nabla \times \vec{E} = i\omega\mu\vec{H} \quad (2.3)$$

$$\nabla \times \vec{H} = -i\omega\varepsilon\vec{E} \quad (2.4)$$

where the permittivity ε and the permeability μ are continuous. Applying $\nabla \times$ to equation (2.3) and (2.4) yields

$$\nabla \times (\nabla \times \vec{E}) = i\omega\mu\nabla \times \vec{H} = \omega^2\varepsilon\mu\vec{E}$$

$$\nabla \times (\nabla \times \vec{H}) = -i\omega\varepsilon\nabla \times \vec{E} = \omega^2\varepsilon\mu\vec{H}$$

Provided the vector identity

$$\nabla \times (\nabla \times \vec{A}) = \nabla \cdot (\nabla \cdot \vec{A}) - \nabla^2 \vec{A}$$

We obtain

$$\nabla^2 \vec{E} + k^2 \vec{E} = 0, \quad \nabla^2 \vec{H} + k^2 \vec{H} = 0 \quad (2.5)$$

Namely the wave equation

$$\nabla^2 \psi + k^2 \psi = 0 \quad (2.6)$$

The solutions of this equation are determined by the boundary condition in specific system. In this problem, the field undergoes discontinuous environment when crossing the boundary between sphere and medium. The boundary condition on the fields is that the tangential components are supposed to be continuous on the interface between two media:

$$\begin{aligned} [\vec{E}_2(x) - \vec{E}_1(x)] \times \hat{n} &= 0 \\ [\vec{H}_2(x) - \vec{H}_1(x)] \times \hat{n} &= 0 \end{aligned} \quad (2.7)$$

where $\vec{E}_1(x)$ and $\vec{E}_2(x)$ are field inside particle and in the surrounding medium, x is on the particle surface S , \hat{n} is pointing outward normal to S .

In spherically symmetric problems, it is more convenient to choose functions ψ that satisfy the wave equation written in spherical polar coordinates r, θ, ϕ .

$$\frac{1}{r^2} \frac{\partial}{\partial r} \left(r^2 \frac{\partial \psi}{\partial r} \right) + \frac{1}{r^2 \sin \theta} \frac{\partial}{\partial \theta} \left(\sin \theta \frac{\partial \psi}{\partial \theta} \right) + \frac{1}{r^2 \sin^2 \theta} \frac{\partial^2 \psi}{\partial \phi^2} + k^2 \psi = 0 \quad (2.8)$$

and the boundary conditions are

$$\begin{aligned} E_{i\theta} + E_{s\theta} &= E_{1\theta}, & E_{i\phi} + E_{s\phi} &= E_{1\phi} \\ H_{i\theta} + H_{s\theta} &= H_{1\theta}, & H_{i\phi} + H_{s\phi} &= H_{1\phi} \end{aligned} \quad (2.9)$$

Constructing solutions of Maxwell equations (2.8) that satisfy the boundary conditions (2.9) results in the scattered field:¹¹³

$$\vec{E}_S = \prod_{n=1}^{n=\infty} i^n E_i \sqrt{(2n+1)(ia_n \vec{N}_m)} - b_n \vec{M}_m \quad (2.10)$$

where n is the multipole order (i.e., $n=1$ stands for dipole mode, 2-quadrupole etc.) for scattering elements and it is terminated according to the convergence criterion $n = x + 4\sqrt[3]{x} + 2$ with $x = \frac{2\pi r}{\lambda}$, as proposed in [Bohren and Huffman, 1983]. E_i is the incident electric field strength, and Mie coefficients a_n, b_n depend on particle size and material coefficients for electric and magnetic multipole modes. Given a typical system, once the Mie coefficients are known, the scatterer optical response is supposed to be uncovered. The expression of total scattering cross section of a sphere for a plane wave is given by:

$$C_{sca} = \frac{P_{sct}}{I_i} = \frac{2\pi}{k^2} \sum_{n=1}^{\infty} (2n+1)(|a_n|^2 + |b_n|^2) \quad (2.11)$$

Where P_{sct} is the scattered light power, I_i is the incident light intensity. If the permeability of the particle and the surrounding medium to be the same ($\mu_1 = \mu_2$), the coefficients can be derived from the following expressions:

$$a_n = \frac{\psi_n(x)\psi'_n(mx) - m\psi'_n(x)\psi_n(mx)}{\xi_n(x)\psi'_n(mx) - m\xi'_n(x)\psi_n(mx)} \quad (2.12)$$

$$b_n = \frac{\psi_n(mx)\psi'_n(x) - m\psi_n(x)\psi'_n(mx)}{\psi_n(mx)\xi'_n(x) - m\xi_n(x)\psi'_n(mx)} \quad (2.13)$$

where m is the complex refractive index, $x = \frac{2\pi r}{\lambda}$ is the size parameter given λ is the wavelength of the radiation and r is the radius of the sphere, prime denotes a derivation with respect to the argument in parentheses. The Functions $\psi_n(x)$ and $\xi_n(x)$ are Riccati-Bessel functions defined in terms of the spherical Bessel function of the first kind, $J_n(x)$, and the spherical Hankel function of the first kind, $H_n^{(1)}(x)$.¹¹⁴

$$\psi_n(x) = xj_n(x) = \sqrt{\frac{\pi x}{2}} J_{n+\frac{1}{2}}(x) \quad (2.14)$$

$$\xi_n(x) = xh_n(x) = -\sqrt{\frac{\pi x}{2}} H_{n+\frac{1}{2}}^{(1)}(x) \quad (2.15)$$

On the other hand, for the case that the particle is much smaller than the wavelength of incident light, the Rayleigh scattering cross section is proportional to the absolute square of particle polarizability:

$$C_R = \frac{k^4}{6\pi} |\alpha|^2 \quad (2.16)$$

where α is the polarizability of the particle and k is the wave vector in the medium. For a nanosphere with polarizability of $4\pi r^2 \frac{\varepsilon-1}{\varepsilon+2}$, the scattering cross section is given as $\left(\frac{8\pi}{3}\right) \left(\frac{2\pi m_0}{\lambda}\right)^4 r^6 \left(\frac{\varepsilon-1}{\varepsilon+2}\right)^2$, where m_0 and ε_0 are the refractive index and permittivity of medium, r and ε are the radius and permittivity of nanosphere. Accordingly, Mie theory may be used to describe most spherical particle scattering systems, including Rayleigh scattering. However, Rayleigh scattering theory is generally preferred if applicable because of the complexity of the Mie scattering formulation.

2.1.2 Dielectric function of metallic and dielectric material

Dielectric function describes the electric polarizability response of material to external electric field, denoted by the Greek letter ε . It can be experimentally determined via complex refractive index of the medium, $\tilde{n}(\omega) = n(\omega) + i\kappa(\omega)$, defined as $\tilde{n} = \sqrt{\varepsilon}$. As previously stated, an applied electromagnetic field drives the positive and negative charges in material oscillating. Since the nucleus of atom is much more massive than the electrons, the oscillation resembles conduction electrons moving against a background of heavy immobile ions. Hence, the optical response of material can be treated as an electron-spring model.

In metallic structures, electrons can more or less freely move under the influence of applied electric fields. Therefore, they are considered as ideal gas in the Drude model, therein the dielectric function of metal is approximated as:¹¹⁵

$$\varepsilon_{Drude} = \varepsilon_{\infty} - \frac{\omega_p^2}{\omega^2 - i\omega\gamma} \quad (2.17)$$

Where the plasma frequency $\omega_p = \sqrt{\frac{Ne^2}{m\varepsilon_0}}$ is a function of electron density N , as well as the effective mass m , and the vacuum dielectric function ε_0 . Their motion is damped via collisions occurring with a characteristic collision frequency $\gamma = \frac{1}{\tau}$ (τ is the relaxation time of electron gas). It is noteworthy that the Drude model is proposed under free-electron approximation, which means it's adequate when electrons from filled band are not excited

to higher bands. Once interband transition occurs, it cannot provide a good fit to the experimental data such as gold at the visible range.

Figure 2.2 displays measured values (blue circles) of the real and imaginary components for gold dielectric function from [Johnson and Christy, 1972].¹¹⁶ The black curve, fitted by the Drude model with parameters presented in previous publication¹¹⁷ shows clear mismatch with the experimental data at high frequencies, especially for the imaginary part because the Drude model considerably underestimates losses in the visible.

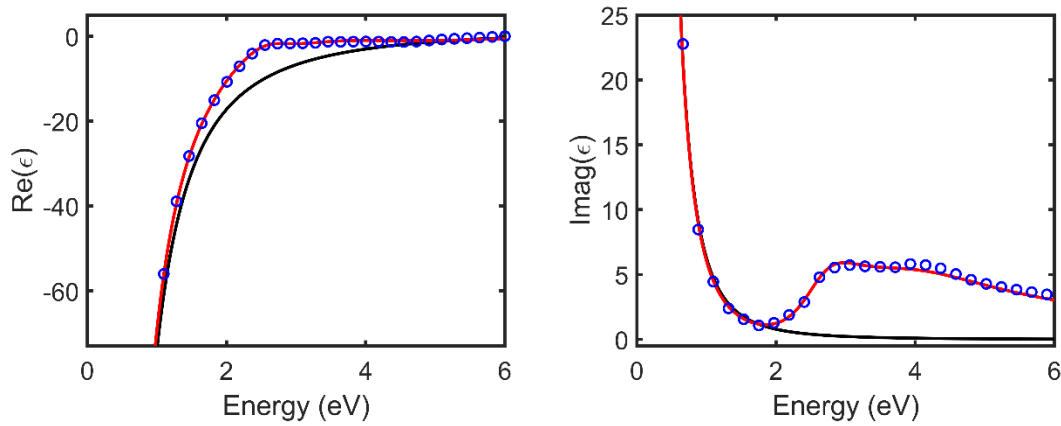


Figure 2.2 Dielectric function $\varepsilon(\omega)$ of gold from the literature values (blue circle) fitted by Drude model (black line) and Drude-Lorentz model (red line).

The limitation of Drude model in visible range can be overcome by incorporating a separated interband (bound-electron) expression. The interband transition effect can be described by means of a Lorentz component, leading to the Drude-Lorentz model

$$\varepsilon_{D-L} = \varepsilon_{Drude} + \sum_{k=1}^l \frac{\omega_p^2}{\omega_l^2 - \omega^2 - i\omega\gamma_l} \quad (2.18)$$

Where l is the number of Lorentz resonances, ω_l and γ_l are the plasma frequency and damping frequency for the bound electrons. The gold dielectric function calculate by the extended Drude model matches the measured data much better as presented in figure 2.2.

For semiconductors that have a negligible free carrier density, their dielectric function in the visible and ultraviolet range is dominated by interband transitions, while the Drude

contribution is neglectable. Therefore, they can be constructed by linear combinations of several Lorentzian resonances:

$$\varepsilon_L = \varepsilon_\infty + \sum_{k=1}^l \frac{\omega_p^2}{(\omega)_l^2 - \omega^2 - i\omega\gamma_l} \quad (2.19)$$

For example, the crystalline silicon (Si) dielectric function measurement data (blue curve) is perfectly fitted according to equation (2.19) as shown in figure 2.3. The fitting parameters are invoked in [48]. Here 5 resonances ($l=5$) are included and the phases of all 5 poles are close to $\frac{\pi}{2}$, corresponding to a classical damped Lorentz oscillator, such as a spring.

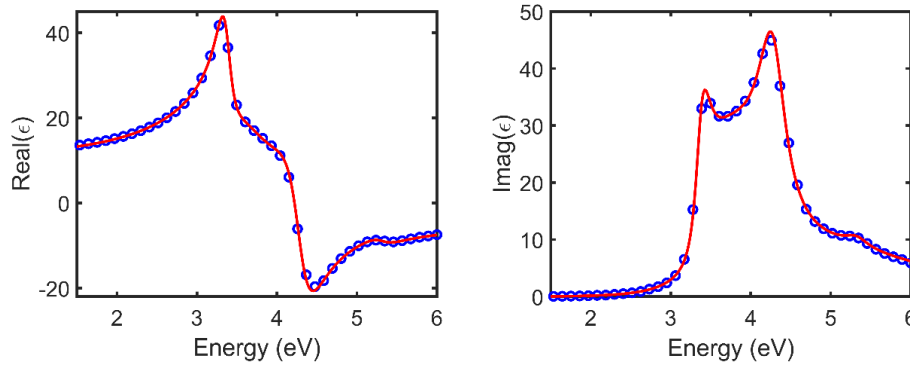


Figure 2.3 Dielectric function $\varepsilon(\omega)$ of Si (red curve) fitted by Lorentz model (blue circles) with parameters from previous publication.

2.1.3 Metallic and dielectric optical antenna

Typically, optical antennas are based on metals (Au and Ag) owing to their radiation less energy transport and spatial field confinement properties of SPPs. However, such metallic materials have high losses at optical frequencies. Together with the limited electric field enhancement,^{118, 119} new materials of high-index dielectric nanostructures with improved plasmonic properties have been proposed. These structures can facilitate light manipulation, and offer very low optical losses, moreover, support both electric and magnetic resonant response. Here we compare the scattering cross section of plasmonic, and high-index dielectric nanoparticle as shown in figure 2.4. The calculation is based on

the Mie scattering coefficient equations from equation (2.11) - (2.15) and the involved material properties are discussed in part 2.1.2.

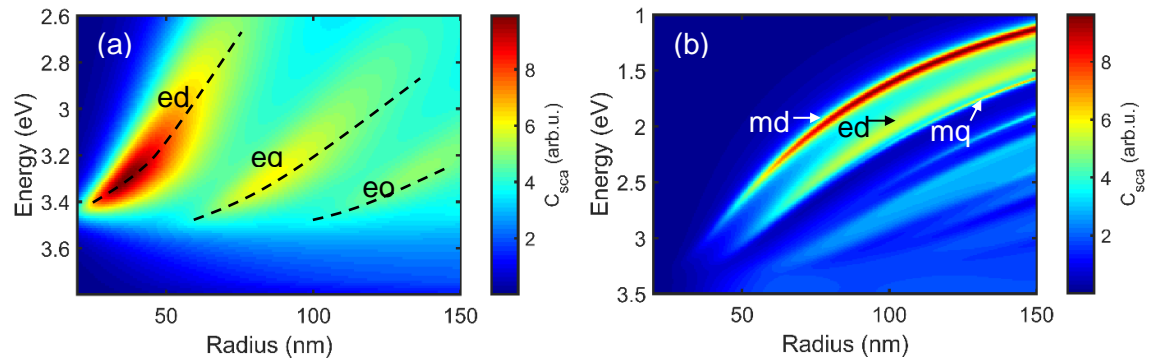


Figure 2.4 Total scattering cross section of (a) Ag nanosphere and (b) Si nanosphere, depending on radius and incident light energy.¹²⁰

Scattering coefficient diagram of Ag and Si nanoparticle is presented as function of their radius and incident light energy. For an Ag nanoparticle with diameter below 140 nm and in the energy range of 2.6 eV to 3.8 eV, there is resonant mode of electric dipole (ed), electric quadrupole (eq), and electric octupole (eo). All resonances demonstrate a red shift with increasing nanoparticle radius from 20 nm to 150 nm. On the other hand, the high-index dielectric Si nanoparticle supports both electric and magnetic resonance. Magnetic mode also displays smooth spectral red-shift with increase of particle size.

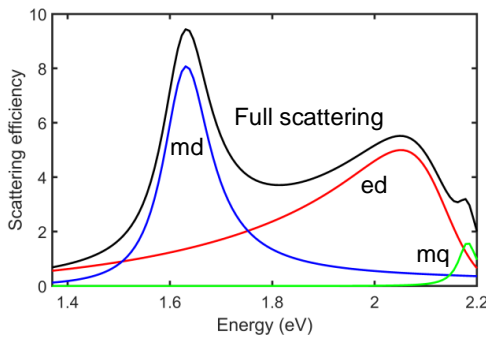


Figure 2.5 Scattering spectrum from a free-standing Si sphere with a radius of 100 nm calculated by Mie theory, with the overall scattering efficiency (black curve) and the

contributions of the electric dipole (red) and magnetic dipole (blue) and quadrupole (green) modes.^{120, 121}

For the dielectric material, as the main concern in this work, figure 2.5 illustrates the scattering spectrum of a Si particle with diameter of 100 nm (black curve). The overall spectrum can be further decomposed into several Mie resonant modes, namely the magnetic dipole (blue curve), electric dipole (red curve), and magnetic quadrupole (green curve).^{120, 121}

Concerning the dissipative losses of metallic and dielectric nanostructures, we also calculate the absorption cross section of Ag nanoparticle and Si nanoparticle according to Equation (2.20) and (2.21).^{108, 122, 123} A significant less absorption strength of Si nanoparticle can be seen in Figure 2.6 in comparison to Au nanoparticle, and the absorption of Si rapidly decreases as the light energy is reduced because of the lower loss away from the main absorption band.

$$C_{ext} = \frac{2\pi}{k^2} \sum_{n=1}^{n=\infty} (2n+1) \text{Re}(a_n + b_n) \quad (2.20)$$

$$C_{abs} = C_{ext} - C_{sct} \quad (2.21)$$

Where C_{ext} and C_{abs} are extinction and absorption cross sections of a particle.

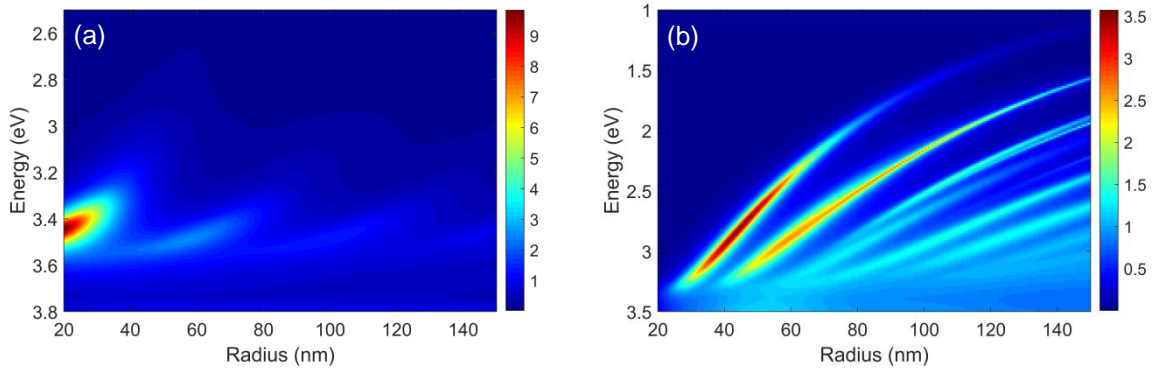


Figure 2.6 Total absorption cross section of (a) Ag nanosphere and (b) Si nanosphere, depending on radius and incident light energy.

2.2 Optical waveguide

Waveguide nanostructures are also an approach to manipulate light. This paragraph discusses the wave propagation in a simple form of waveguide, step index optical fiber. Its structure is sketched in figure 2.7. A light-conducting fiber core with circular cross-section is surrounded by ring-shaped cladding area, forming a refractive index profile:

$$n(r) = \begin{cases} n_K & r < a \\ n_M & a < r < \frac{D}{2} \end{cases}$$

In order to realize light confinement, the refractive index of cladding material n_M is about a few percent smaller than that of the core n_K , satisfying the total internal reflection condition.

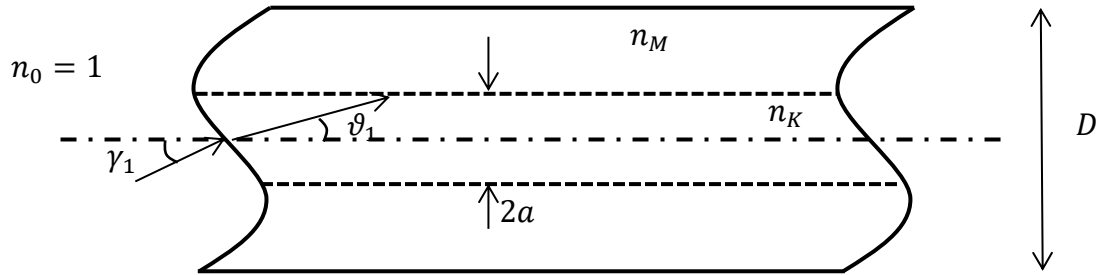


Figure 2.7 schematic of a step index fiber. The index 'K', 'M' and 'O' denotes the quantity of core, cladding, and vacuum, respectively.

In this geometry, we take the wave equation (2.6) in cylindrical coordinates r, ϕ, z , and the wave propagation is in z direction

$$\frac{1}{r} \frac{\partial}{\partial r} \left(r \frac{\partial}{\partial r} E \right) + \frac{1}{r^2 \partial \phi^2} E + \frac{\partial^2}{\partial z^2} E = -k^2 \frac{\partial^2}{\partial t^2} E \quad (2.22)$$

It can be sorted as¹²⁴

$$-\frac{1}{\phi} \frac{\partial^2}{\partial \phi^2} \Phi = \frac{1}{\mathcal{R}} \left(r^2 \frac{\partial^2}{\partial r^2} \mathcal{R} + r \frac{\partial}{\partial r} \mathcal{R} + r^2 (k^2 - \beta^2) \mathcal{R} \right) \quad (2.23)$$

with the electric field $E = \mathcal{R}(r)\Phi(\phi)$. β is named as propagation constant, which is the longitudinal component of wave vector. Clearly, the two variables ϕ and r of optical field

stand separately in two sides of the function and must be equal to some constant, l^2 for instance. Therefore, we get two equations of function $\Phi(\phi)$ and $\mathcal{R}(r)$:

$$\frac{\partial^2}{(\partial\phi^2)}\Phi + l^2\Phi = 0 \quad (2.24)$$

$$r^2 \frac{\partial^2}{\partial r^2} \mathcal{R} + r \frac{\partial}{\partial r} \mathcal{R} + (\kappa^2 r^2 - l^2) \mathcal{R} = 0 \quad (2.25)$$

with $\kappa^2 = k^2 - \beta^2$. Recall the introduction of β as longitudinal wave vector, κ is therefore the transversal component of wave vector k .

Apparently, the equation (2.25) has the form of Bessel's differential equation where l is the order of the Bessel equation. For a specific l , it is solved by:

$$\mathcal{R} = \begin{cases} c_1 J_l(\kappa r) + c_2 N_l(\kappa r) & (\kappa r)^2 \geq 0 \\ c_3 I_l(\kappa r) + c_4 K_l(\kappa r) & (\kappa r)^2 < 0 \end{cases} \quad (2.26 \text{ a})$$

where J_l , N_l , I_l , K_l are Bessel functions, $(\kappa r)^2 < 0$ corresponds to an imaginary wave vector component in fiber cross section, representing the evanescent wave in cladding, and the relationship of $k_K^2 - \beta^2 \geq 0$ in core and $k_M^2 - \beta^2 < 0$ in cladding, implies that $k_K \geq \beta > k_M$.

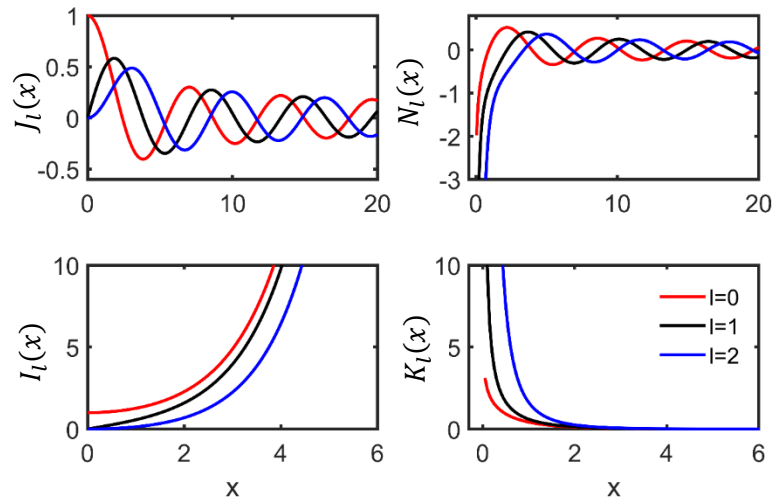


Figure 2.8 Plot of Bessel function of the first kind J_l and second kind Y_l , as well as modified Bessel function of the first kind I_l and second kind K_l for integer orders $l = 1, 2, 3$.

Figure 2.8 illustrates four Bessel functions for low orders. Both J_l and N_l display oscillating line shape and I_l , K_l are exponentially increasing or decreasing function. Physically speaking, we do not expect an electric field amplitude to have singularities. However, N_l has singularity at origin ($x=0$), and J_l is infinite as x increases, therefore the coefficient of N_l in the core, I_l in the cladding are supposed to be eliminated. Moreover, J_l is finite at the origin ($x=0$) for integer number l , otherwise it is a multivalued function with singularity at 0. Hence, l must be an integer number. Overall, the solution $\mathcal{R}(r)$ holds the form of either Bessel function J_l in core or modified Hankel function K_l in cladding:

$$\mathcal{R} = \begin{cases} c_1 J_l(\kappa r) & r \leq a \\ c_4 K_l(\kappa r) & r > a \end{cases} \quad (2.26 \text{ b})$$

To this point, we may seek the solutions. Because the equation (2.24) has general solution of

$$\Phi = c_0 \cos(l\phi + \phi_0) \quad (2.27)$$

Where c_0 and ϕ_0 are constant. Φ and $\frac{\partial \Phi}{\partial \phi}$ must be continuous at ϕ_0 and $\phi_0 + 2\pi$.

the solution of the wave equation for a step index fiber is given by

$$\begin{aligned} E_K &= C_K J_l\left(\frac{ur}{a}\right) \cos(l\phi + \phi_0) & r \leq a \\ E_M &= C_M K_l\left(\frac{wr}{a}\right) \cos(l\phi + \phi_0) & r > a \end{aligned} \quad (2.28)$$

Here $u = \kappa_K a$ and $w = \kappa_M a$ are real positive quantities. Combing the boundary condition that solutions are continuous at $r = a$:

$$\begin{aligned} E_K(r = a) &= E_M(r = a) \\ \frac{\partial}{\partial r} E_K(r = a) &= \frac{\partial}{\partial r} E_M(r = a) \end{aligned} \quad (2.29)$$

the characteristic relation determining solutions of the wave equation in a step index fiber is obtained:

$$\frac{J_l(u)}{u J_{l+1}(u)} = \frac{K_l(w)}{w K_{l+1}(w)} \quad (2.30)$$

For a given a system with known a, n_K, n_M , the propagation of light can be described numerically from Equation (2.30). It has multiple solutions that are numbered with $l = 1, 2, 3, \dots$. Adopting the terminology that was introduced for fiber modes in 1971 by Gloge,¹²⁵ These are LP₀₁, LP₁₁, LP₀₂, and LP₂₁ modes strongly localized within the waveguide. Here, the first index indicates the number of pairs of nodes of the electric field strength in the azimuthal coordinate, and the second index gives the number of nodes in the radial direction, including the approach toward zero for large radii. Before we discuss the mode profile for different value of l , the parameters we introduced are summarized in table 1, which are also universally used in literatures.

Table 1

	Definition
Longitudinal wave vector	$k_K \geq \beta > k_M$
Transversal wave vector	$\kappa = \sqrt{k^2 - \beta^2}$
Core parameter	$u = a \sqrt{k_0^2 n_K^2 - \beta^2}$
Cladding parameter	$w = a \sqrt{\beta^2 - k_0^2 n_M^2}$
Fiber parameter	$V = u^2 + w^2 = ak_0 \sqrt{n_K^2 - n_M^2}$

Now we take a numerical example of a step index fiber with radius of 1 μm and $n_K = 2$, $n_M = 1.4$. The calibrated electric field distributions of four typical modes for an incident light wavelength of 900 nm are displayed in figure 2.9. For mode LP₀₁, the distribution is rotationally invariant, and on any circular path around the center one would find a constant field amplitude. For mode LP₁₁ and LP₁₃, the field amplitude will vary according to a sinusoidal function of the azimuthal angle. There is a positive lobe and a negative lobe, and the algebraic sign indicates the phase of the field. Thus, in one lobe the field

oscillates in opposite phase to the other. For mode LP_{42} , a circular path would run through four full periods of the sine function. The electric field pattern then resembles a four-leafed clover. Again, each pair of leaves in opposite positions has the same phase while the other pair has opposite phase.

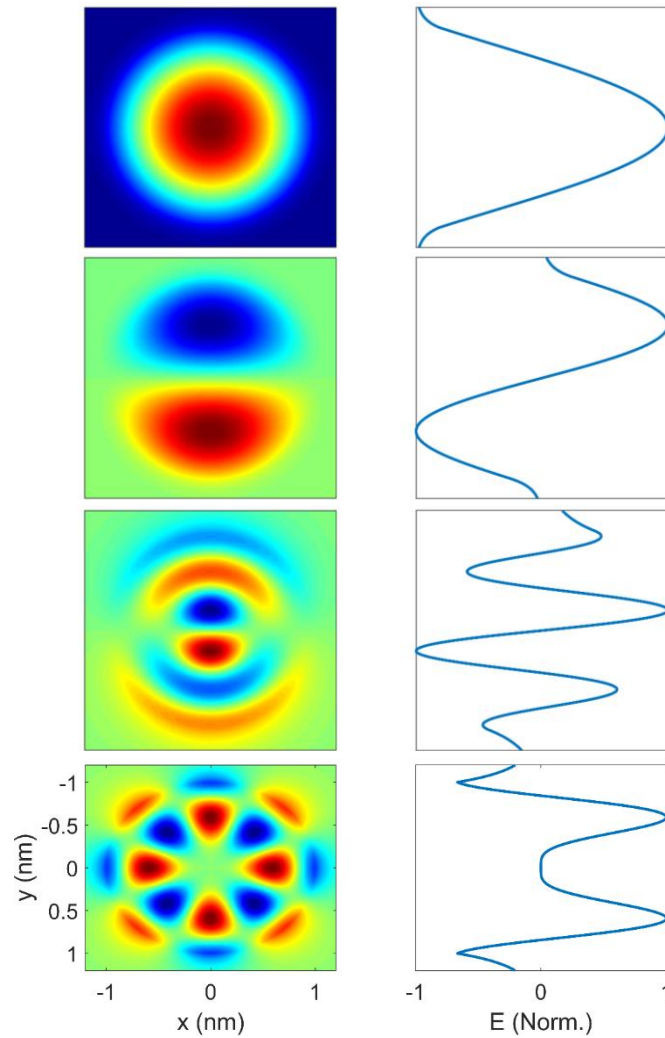


Figure 2.9 Electric field distributions of several LP modes and normalized electric field plots at the center position. From top: LP_{01} , LP_{11} , LP_{13} , LP_{42} .

2.3 Optical local density of state

The rapid development of SNOM technique calls for a theoretical understanding the signals of near-field optical microscopy and spectroscopy. Unlike the far-field optical microscope, the images obtained by SNOM are not necessarily coincident with the topography but are expected to be the solutions of Maxwell equations. Carminati and Sáenz proposed that the measured near-field quantity is related to optical local density of state (LDOS).¹²⁶

As well known, the LDOS is not a commonly used concept in optics but is rather applied to electrons in solid state physics. It describes the possibility of finding an electron of energy $\hbar\omega$ in a volume V . It was demonstrated that, in STM, the tunneling current is proportional to the value of the electron LDOS of the surface.¹²⁷ The analogy between STM and SNOM, under a weak tip-sample coupling approximation, allows using the formula of scanning tunneling microscopy (STM) to fundamentally understand SNOM signal. Moreover, the connection of measured near-field quantity and optical local density of states (LDOS) was demonstrated by experimental work.^{128, 129}

2.3.1 Scanning tunneling microscope

The scanning tunneling microscope (STM), namely based on quantum mechanical tunneling, is a type of microscope for imaging geometry of surfaces at the atomic level. The idea is applying a small bias voltage between an atomically metallic tip and conducting material, when the sharp tip is brought in proximity to the sample ($\leq 10\text{\AA}$), a tunneling electrons form current flowing across the gap.^{130, 131} The measurements are usually performed in a constant current mode to probe the electronic structure of the sample. The tip is mounted on a piezo drive made of piezoelectric ceramics, therefore the tunneling current is kept constant during scanning the sample by applying appropriate voltages to the piezo drive. Simultaneously a feedback loop controls the distance between the sample and the tip to achieve a constant tunneling current. Finally, the applied voltages to piezo drive are converted into a topographic image of the scanned surface with a resolution in the order of atomic distances. It is noteworthy that the image can not only be interpreted as a topographic map but also probe information on the

property vibrations of the sample because the tunneling current is influenced by the lateral and vertical variation of the electronic state density at the surface.

2.3.1.1 Tunneling a rectangular potential barrier

The relationship between STM signal and electric LDOS is concluded from the tunneling current between the probe and sample surface. Before deducing the STM tunneling signal, we firstly introduce the general concept of quantum tunneling.

In classical mechanics, it is not possible for a particle to penetrate or across a potential such as a barrier if the energy of a particle is smaller than the potential energy of the barrier. In quantum, a particle as wave-like properties may propagate through a potential barrier, known as quantum tunneling. Tunneling is normally described by a transmission coefficient which gives the ratio of the current density emerging from a barrier divided by the current density incident on a barrier. Here we illustrate quantum tunneling in simple case of a particle in a rectangular potential energy barrier.

Suppose a uniform and time-independent beam of electrons with energy E traveling along x-axis encounters a potential barrier illustrated in figure 2.10. A constant potential $V(x) = V_0$ resembles the energy barrier between the STM tip and the sample surface. Therefore, the area is divided into three regions. Region I and region III represent the tip and sample respectively, and region II represents the vacuum gap. We consider the situation that $E < V_0$. The question here is the probability of an individual particle in region I traversing through the potential barrier to region III.

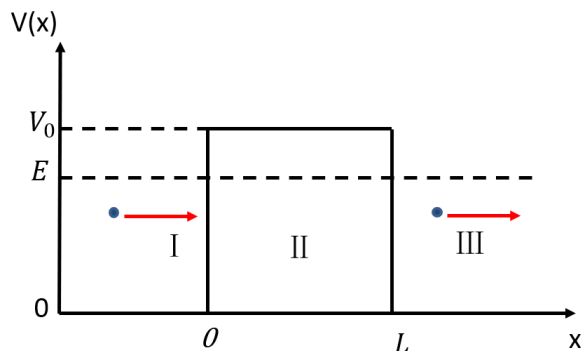


Figure 2.10 Schematic of a potential energy barrier.

The wave characteristics of a particle is described by wave function which is determined by the Schrödinger equation, analogous to electric and magnetic fields described by Maxwell's equations. The time independent Schrödinger equation in 1D case is

$$H\psi(x) = -\frac{\hbar^2}{2m} \frac{d^2\psi(x)}{dx^2} + V(x)\psi(x) = E\psi(x) \quad (2.31)$$

where $\psi(x)$ is the Hamiltonian, m is the mass, E the energy of the particle, and $V(x)$ is the potential energy of barrier that in this case follows the function:

$$V(x) = \begin{cases} 0, & x < 0 \\ V_0 & 0 \leq x \leq L \\ 0, & x > L \end{cases} \quad (2.32)$$

Hence the stationary Schrödinger function has three forms in three regions. In left region I $-\infty < x < 0$,

$$-\frac{\hbar^2}{2m} \frac{d^2\psi_I(x)}{dx^2} = E\psi_I(x) \quad (2.33)$$

In region II $0 \leq x \leq L$,

$$-\frac{\hbar^2}{2m} \frac{d^2\psi_{II}(x)}{dx^2} = (E - V_0)\psi_{II}(x) \quad (2.34)$$

In region III $L < x < \infty$,

$$-\frac{\hbar^2}{2m} \frac{d^2\psi_{III}(x)}{dx^2} = E\psi_{III}(x) \quad (2.35)$$

The general solution of such differential equation is a linear combination:

$$\psi(x) = C_1 e^{\lambda_1 x} + C_2 e^{\lambda_2 x} \quad (2.36)$$

where $\lambda_{1,2}(V) = \pm \sqrt{-\frac{2m}{\hbar^2}(E - V)}$. These coefficients can be either real or imaginary depending on the relative magnitude of particle energy E and potential barrier V . The sign ' \pm ' indicates the direction of moving waves either forward '+' or backward '-'. Therefore, the solutions of the Schrödinger function (2.33) - (2.35) are obtained separately for each region

$$\text{I. } V = 0, \quad \psi_{\text{I}}(x) = Ae^{ik_{\text{I}}x} + Be^{-ik_{\text{I}}x} \quad \text{with } k_{\text{I}} = \sqrt{\frac{2mE}{\hbar}} \quad (2.37)$$

$$\text{II. } V = V_0, \quad \psi_{\text{II}}(x) = Ce^{k_{\text{II}}x} + De^{-k_{\text{II}}x} \quad \text{with } k_{\text{II}} = \sqrt{\frac{-2m(E-V_0)}{\hbar}} \quad (2.38)$$

$$\text{III. } V = 0, \quad \psi_{\text{III}}(x) = Fe^{ik_{\text{III}}x} \quad \text{with } k_{\text{III}} = \sqrt{\frac{2mE}{\hbar}} \quad (2.39)$$

There are two waves in region I, in which one is incident $\psi_{\text{in}}(x) = Ae^{ik_{\text{I}}x}$ and the other is reflected $\psi_{\text{ref}}(x) = Be^{-ik_{\text{I}}x}$. In region III, there is only one term because there only exists transmitted wave $\psi_{\text{tra}}(x) = Fe^{ik_{\text{III}}x}$. In the region II, the coefficient λ in Equation (2.36) is imaginary number, therefore the general solution is not oscillatory but in the form of exponentials. The relation between five coefficients can be calculated from the continuity condition at region boundaries

$$\psi_{\text{I}}(0) = \psi_{\text{II}}(0); \quad \psi_{\text{II}}(L) = \psi_{\text{III}}(L) \quad (2.40)$$

$$\frac{d\psi_{\text{I}}(0)}{dx} = \frac{d\psi_{\text{II}}(0)}{dx}; \quad \frac{d\psi_{\text{II}}(L)}{dx} = \frac{d\psi_{\text{III}}(L)}{dx} \quad (2.41)$$

In general, the probability density is $|\psi(x)|^2 = \psi(x)\psi^*(x)$, hence the tunneling probability or transmitted probability can be obtained from the ratio of corresponding coefficients. For instance, the probability of transmission is given as

$$T = \frac{|\psi_{\text{tra}}(x)|^2}{|\psi_{\text{in}}(x)|^2} = \frac{|F|^2}{|A|^2} \quad (2.42)$$

This is the probability a particle in incident beam tunneling through the potential barrier as a function of barrier width L , particle total energy E , and barrier potential energy V_0 . When an electron is incident upon a vacuum barrier with potential energy larger than the kinetic energy of the electron, there is still a non-zero probability that it may travel the forbidden region and appear on the other side of the barrier.

2.3.1.2 Tunneling current

Theories of STM had been developed shortly after the first experimental demonstrations. Many of these theories are in common derivation analogous to that of Bardeen's

approach which makes use of the time dependent perturbation theory, originally derived for electron tunneling between two weakly coupled electrodes.¹³² In Bardeen's formalism, the total tunneling current in terms of wave functions determined separately for each electrode in the absence of each other is given by

$$I = \frac{2\pi e}{\hbar} \sum_{\mu\nu} f(E_\mu) [1 - f(E_\nu + eV)] |M_{\mu\nu}|^2 \delta(E_\mu - E_\nu) \quad (2.43)$$

$$f(E) = e^{\left(\frac{E-E_F}{k_B T} + 1\right)^{-1}} \quad (2.44)$$

$f(E)$ is the Fermi function, V is the applied voltage, $M_{\mu\nu}$ is the tunneling matrix element between the tip wavefunction ψ_μ and the sample surface wavefunction ψ_ν . $\delta(x)$ the delta function, E_μ and E_ν are the energy of the state ψ_μ and ψ_ν in the absence of tunneling. For small tunneling voltages and low temperature, $f(E)$ can be expanded to obtain:

$$I = \frac{2\pi}{\hbar} e^2 V \sum_{\mu,\nu} |M_{\mu\nu}|^2 \delta(E_\mu - E_F) \delta(E_\nu - E_F) \quad (2.45)$$

the tunneling matrix element is given by an integral over a surface in the barrier region lying between the tip and sample, as shown by Bardeen:

$$M_{\mu\nu} = \frac{\hbar^2}{2m} \int (\psi_\mu^* \vec{\nabla} \psi_\nu - \psi_\nu \vec{\nabla} \psi_\mu^*) d\vec{s} \quad (2.46)$$

Where m is the free electron mass, $*$ denotes the complex conjugate.

Tersoff and Hamann have applied this model and described the tip as a spherical potential well where approaches nearest to the surface with a distance d as sketched in figure 2.11.¹²⁷ The local radius of curvature of the tip apex is R . As discussed in equation (2.37) – (2.39), the wavefunctions in the gap can be written as:

$$\psi_\nu(z) = \psi_\nu^0 e^{\kappa z} \quad (2.47)$$

$$\psi_\mu(z) = \psi_\mu^0 e^{\kappa(z-d)} \quad (2.48)$$

where $\kappa = \frac{\sqrt{2m\phi}}{\hbar}$ is the minimum inverse decay length for the wave function in vacuum, ϕ is the local barrier height. Such exponential dependence enables STM atomic scale resolution. The wavefunctions in the xy plane are expanded:

$$\psi_v^0 = \Omega_s^{-\frac{1}{2}} \sum_G a_G e^{(\kappa^2 + |\vec{k}_\parallel + \vec{G}|^2)^{\frac{1}{2}} z} e^{i(\vec{k}_\parallel + \vec{G})\vec{x}} \quad (2.49)$$

$$\psi_\mu = \Omega_t^{-\frac{1}{2}} c_t \kappa R e^{\kappa R} (\kappa |\vec{r} - \vec{r}_0|)^{-1} e^{-\kappa |\vec{r} - \vec{r}_0|} \quad (2.50)$$

where $\Omega_{s/t}$ is the volume of sample or tip, \vec{k}_\parallel is a surface Bloch wave vector of the state, and \vec{G} is a two-dimensional reciprocal-lattice vector of the surface. The first few factors a_G are typically of order unity.

The concluded tunneling current is:

$$I = \frac{32\pi^3 e^2 V}{h} \phi^2 D_t(E_F) R^2 \kappa^{-4} e^{2\kappa R} \times \sum_v |\psi_v(\vec{r}_0)|^2 \delta(E_v - E_F) \quad (2.51)$$

Where D_t is the density of states per unit volume of the tip.

Correspondingly, the tunneling conductance $\frac{dI}{dV}$ can be obtained as $\sigma \propto \rho(r_0, E_F)$ that is proportional to the surface local density of states:

$$\rho(r_0, E_F) = \sum_v |\psi_v(\vec{r}_0)|^2 \delta(E_v - E_F) \quad (2.52)$$

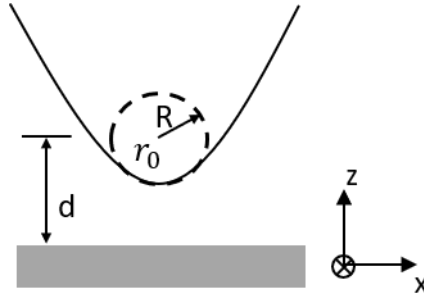


Figure 2.11 Geometry of tip-sample tunneling. Prober has a locally spherical apex with radius of curvature R . The center of curvature is at position of \vec{r}_0 . The distance between tip a sample surface is d .

Therefore, by measuring the derivation of the tunneling current with respect to the applied voltage, one can simply detect the sample local density of state.

Experimentally, electron LDOS was nicely imaged in the direct space with low temperature STM in 1993.¹³³ Crommie, Lutz, and Eigler constructed a quantum corral with STM by placing 48 Fe atoms on a Cu surface, forming a ring with diameter of 10 nm.

The electronic local density of states at fermi energy surrounding the atoms were beautifully observed.

2.3.2 Optical LDOS

The identification of the role of the electron LDOS in the formation of STM images led Carminati and Sáenz to derive Bardeen's formula to the scattering of electromagnetic waves in SNOM.¹³⁴ For the SNOM situation, the tip-sample system is illuminated by a light source, and part of the scattered energy is collected by a detector. The gap region (between the sample and the tip) is assumed to be vacuum or air. Being analogy to the described stationary state of the electron, the state of the electromagnetic field at a given frequency ω is represented by a wave function $\psi(\vec{r})$, and can be written in the form of an angular spectrum of plane wave as described in equation (2.37) and (2.38)

$$\psi(\vec{r}) = \int_0^\infty a(\vec{k}_\parallel) e^{i\vec{k}_\parallel \vec{R} + i\kappa z} d^2 \vec{k}_\parallel + \int_0^\infty b(\vec{k}_\parallel) e^{i\vec{k}_\parallel \vec{R} - i\kappa z} d^2 \vec{k}_\parallel \quad (2.53)$$

Where $a(\vec{k}_\parallel)$ and $b(\vec{k}_\parallel)$ are angular spectra of the wave function in the gap region, the perpendicular wave vector (along z direction) $\kappa = \sqrt{k^2 - k_\parallel^2}$ for $k_\parallel^2 \leq k^2$ and $\kappa = i\sqrt{k_\parallel^2 - k^2}$ for $k_\parallel^2 > k^2$. The wave vector $k = \frac{\omega}{c}$ for the electromagnetic field with c being the speed of light in vacuum, and $k^2 = \frac{2m}{\hbar^2(E-V)}$ for the electron wave function with m being the electron mass \hbar is the Plonk constant. The notations $\vec{R} = (x, y)$, $\vec{r} = (x, y, z)$.

The optical field probability current can be expressed by the introduced wave function as $\vec{J}(\vec{r}) = \frac{\hbar}{m} \text{Im}[\psi^*(\vec{r}) \nabla \psi(\vec{r})]$ where m is the particle mass, Im denotes imaginary part and ∇ the del operator. It is also called probability flux that describes the flow of probability in terms of probability per unit time per unit area. Therefore, the total current through the gap region across a plane is $\Phi = \int J(r) d^2 R$ in the form of:

$$\Phi = \frac{\hbar}{m} \int_{k_\parallel^2 \leq k^2} \gamma \left[|a(\vec{k}_\parallel)|^2 - |b(\vec{k}_\parallel)|^2 \right] d^2 \vec{k}_\parallel + \frac{\hbar}{m} \int_{k_\parallel^2 > k^2} \gamma \left[a(\vec{k}_\parallel) b^*(\vec{k}_\parallel) - a^*(\vec{k}_\parallel) b(\vec{k}_\parallel) \right] d^2 \vec{k}_\parallel \quad (2.54)$$

Here the total current is proportional to the total energy flux which includes two contributions. The first integral for a real perpendicular wave vector describes

propagating currents flowing in opposite directions. The other integral is for the case of imaginary perpendicular wave vector that describes an evanescent current. This causes the fundamental difference between SNOM and STM that both the propagating wave and evanescent wave are included in SNOM signal, while in the case of STM, the current in the gap only has the evanescent channel.

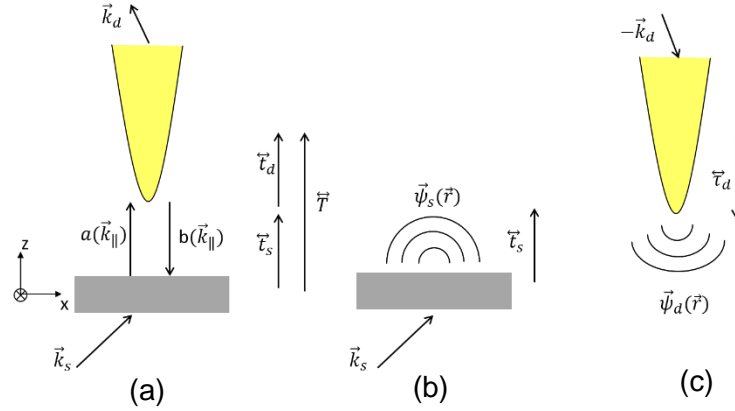


Figure 2.12 (a) A SNOM setup with directional illumination with polarization \vec{a}_s . The light from source is scattered to detector with analyzer along direction of \vec{k}_d . $a(\vec{k}_{\parallel})$ and $b(\vec{k}_{\parallel})$ are the wave function coefficients representing opposite direction. (b) Illustration of the meaning of the sample wave function $\vec{\psi}_s(\vec{r})$ which is the electric field, in the gap region, that results from scattering of the illuminating plane wave by the sample, in the absence of the tip. (c) Illustration of the meaning of the tip wave function $\vec{\psi}_a(\vec{r})$ which is the electric field, in the gap region, that results from scattering by the tip of a plane wave of amplitude unity coming from the direction of the detector (wave vector $-\vec{k}_d$, polarization state \vec{a}_d).

The SNOM signal can in principle be computed with the known angular spectra $a(\vec{k}_{\parallel})$ and $b(\vec{k}_{\parallel})$ that can be obtained by numerically solving the specific scattering problem. Alternatively, analogy to the STM situation, the current can be described from Bardeen's formula in the weak coupling condition. Carminati and Sáenz derived the electromagnetic current formula of SNOM with such approach.¹³⁴ Figure 2.12 shows the SNOM setup depicted in [63]. The incident light wave with wave vector \vec{k}_s has a state of polarization \vec{a}_s . The detected scattering field is defined by the wave vector \vec{k}_d , and its polarization is

determined by the analyzer on the detection path with polarization direction of \vec{a}_d . To express the scatter mathematically, the sample, tip, and the entire setup are described by their transmission tensor $\vec{t}_s(\vec{k}_\parallel, \vec{k}_s)$, $\vec{t}_d(\vec{k}_d, \vec{k}_\parallel)$, $\vec{T}(\vec{k}_d, \vec{k}_s)$. The energy flux density on the detector is the flux of the Poynting vector is

$$S = 2\pi^2 \epsilon_0 c \kappa^2 (\vec{k}_d) |\vec{a}_d \cdot \vec{T}(\vec{k}_d, \vec{k}_s) \cdot \vec{a}_s|^2 \quad (2.55)$$

Where the matrix main quantity of $M_{ds} = \vec{a}_d \cdot \vec{T}(\vec{k}_d, \vec{k}_s) \cdot \vec{a}_s$ is analogous to the tunneling matrix in Bardeen's formalism in equation (2.46).

In a weak coupling approximation, namely the current in the gap results from fields scattered once between tip and sample, the transmission coefficient is

$$\vec{T}(\vec{k}_d, \vec{k}_s) = \int \vec{t}_d(\vec{k}_d, \vec{k}_\parallel) \vec{t}_s(\vec{k}_\parallel, \vec{k}_s) d^2 k \quad (2.56)$$

The two fields illustrated in figure 2.12 (b) and (c) have the form of

$$\vec{\psi}_s(\vec{r}) = \int_0^\infty \vec{t}_s(\vec{k}_\parallel, \vec{k}_s) \cdot \vec{a}_s e^{(i\vec{k}_\parallel \vec{R} + i\kappa z)} d^2 \vec{k}_\parallel \quad (2.57)$$

$$\vec{\psi}_d(\vec{r}) = \int_0^\infty \vec{t}_d(\vec{k}_\parallel, -\vec{k}_d) \cdot \vec{a}_d e^{(i\vec{k}_\parallel \vec{R} - i\kappa z)} d^2 \vec{k}_\parallel \quad (2.58)$$

Where \vec{t}_d satisfies $\kappa(\vec{k}_d) \vec{t}_d(\vec{k}_d, \vec{k}_\parallel) = \kappa(\vec{k}_d) \vec{t}_d^T(\vec{k}_\parallel, \vec{k}_d)$, the superscript T denoting the transposed tensor.¹³⁵ Combing equation (2.57) – (2.58), the critical matrix is

$$M_{ds} = \frac{1}{8\pi^2 i \kappa(\vec{k}_d)} \int [\vec{\psi}_d(\vec{r}) \cdot \frac{\partial \vec{\psi}_s(\vec{r})}{\partial z} - \vec{\psi}_s(\vec{r}) \cdot \frac{\partial \vec{\psi}_d(\vec{r})}{\partial z}] d^2 R \quad (2.59)$$

This equation is like electron tunneling matrix element $M_{\mu\nu}$ which is also an integral of function between state of probe and state of sample. It is noteworthy that the complex conjugation of the tip wave function is absent here. This is not a problem when the tip is not lossy, because the tip wave function $\vec{\psi}_d(\vec{r})$ is a real value.

The derivation of equation (2.59) provides a general expression of the signal in STM and SNOM, which is appropriate to both the tunneling channels and electromagnetic vector fields. This unification thereby opens the way of attributing the SNOM signal to optical LDOS in weak coupling circumstance. Dereux *et al*¹³⁶ suggested that the near-field optical microscope operating in illumination mode should detect the surface

electromagnetic LDOS. Moreover, as the experimentally imaging the electron LDOS of a quantum corral with STM, the optical corral was also designed¹³⁷ and its calculated optical LDOS maps were reproduced by the detected the SNOM near-field signal.¹²⁸

To this point, we have introduced an important approach to explain the SNOM image and spectrum, that is to relate it to the local density of optical states (LDOS). The remaining part would be focused on the numerical calculations of the LDOS of a nanostructure. An elegant expression will be derived from an important relationship between the normal eigen modes of the structure and the dyadic Green's function.^{1, 138}

For a closed non-absorbing nanocavity whose dimension is much smaller than wavelength of light, a set of discrete eigenmodes exist¹³⁹ and obey the Helmholtz equation under a certain boundary condition as introduced in [67]:

$$\nabla \times \nabla \times \vec{e}_n(\vec{r}) - \frac{\varepsilon(\vec{r})\omega_n^2}{c^2} \vec{e}_n(\vec{r}) = 0 \quad (2.60)$$

where $\vec{e}_n(\vec{r})$ and ω_n are regarded as the eigen vectors and eigen frequencies. $\varepsilon(\vec{r})$ is the dielectric function of the medium in the cavity. The corresponding eigen modes, namely the obtained solutions, satisfy the orthogonal relationship

$$\int_V \varepsilon(\vec{r}) \vec{e}_m(\vec{r}) \cdot \vec{e}_n^*(\vec{r}) d^3r = \delta_{mn} \quad (2.61)$$

with the cavity volume V . Hence, the density of states (DOS) that corresponds to the number of states or modes within per unit volume and unit interval of frequency can be defined as:

$$\rho(\omega) = \frac{1}{V} \sum_n \delta(\omega - \omega_n) \quad (2.62)$$

The local DOS is evaluated through a certain summation of the included states whose contribution is weighted by its amplitude of each eigen mode:

$$\rho_e(\omega) = \sum_n |\vec{e}_n(\vec{r})|^2 \delta(\omega - \omega_n) \quad (2.63)$$

The LDOS can be related to the dyadic Green's function as following. The electric Green's function $\vec{G}^E(\vec{r}, \vec{r}', \omega)$ for a homogeneous medium is a solution to:

$$\nabla \times \nabla \times \vec{G}^E(\vec{r}, \vec{r}', \omega) - \frac{\varepsilon(\vec{r})\omega^2}{c^2} \vec{G}^E(\vec{r}, \vec{r}', \omega) = \delta(\vec{r} - \vec{r}') \vec{I} \quad (2.64)$$

where $\vec{\mathbb{I}}$ is the unit tensor.

The Green function can be written in terms of the eigenmodes introduced above,¹³⁸

$$\vec{G}^E(\vec{r}, \vec{r}', \omega) = \sum_n c^2 \frac{\vec{e}_n^*(\vec{r}') \otimes \vec{e}_n(\vec{r})}{\omega_n^2 - \omega^2 - 2i\omega\gamma_n} \quad (2.65)$$

Recalling the LDOS definition in equation (2.63), one can express the LDOS in the form of

$$\rho_e(\vec{r}, \omega) = \frac{2\omega}{\pi c^2} \text{Im}[\text{Tr} G^E(\vec{r}, \vec{r}, \omega)] \quad (2.66)$$

where Tr denotes the trace of the tensor in brackets. The Green's function here describes the dipole emitted power summed over all directions, in contrast, for the case of specific oriented dipole source \vec{u} , a projected LDOS is defined and written in the form

$$\rho_{e,\vec{u}}(\vec{r}, \omega) = \frac{2\omega}{\pi c^2} \text{Im}[\vec{u} \cdot G^E(\vec{r}, \vec{r}, \omega) \cdot \vec{u}] \quad (2.67)$$

In practice, $\rho_{e,\vec{u}}$ is more significant to ρ_e because any detected signal stems from the translation of charge carriers from one point to another. This formula is the main result of this section. It establishes the relationship between the LDOS and the imaginary part of the Green's function, therefore provides a numerical calculation of LDOS which interpolates the near-field signal of SNOM.

Interestingly, the projected LDOS also allows one to calculate the spontaneous decay rate (γ) of a two-level quantum system in an arbitrary reference system:¹

$$\gamma = \frac{2\omega_0}{3\hbar\epsilon_0} |\vec{u}|^2 \rho_{e,\vec{u}}(\vec{r}, \omega) \quad (2.68)$$

2.4 Point dipole model

In this section, we will introduce another SNOM theory of tip-sample coupling system proposed by B. Knoll and F. Keilmann [77], then discuss background suppression and signal contrast enhancement of SNOM signal.

Typically, in scattering SNOM, the incident laser source focused by conventional optics (fibers or objectives) allow for far-field illumination. Hence, the scattered signal comes from not only the near-field of emitters in the vicinity of the tip, but also directly from the

tip shaft as well as the sample. This directly scattered light usually causes a large background signal, obscuring the orders of magnitude smaller near-field signal. It contains no useful information and could introduce artifacts into s-SNOM images. Background suppression methods are therefore required to extract the pure near-field contribution.

In principle, the background signal can be largely avoided by employing adiabatic nanofocusing to SNOM.^{140, 141} This technique is an active topic of current research and first applications in broadband light scattering and time-resolved spectroscopy are currently pursued in different laboratories.⁴⁶ Regular s-SNOM is already much better understood. Specifically, some effort has been devoted in the past to distinguishing the near-field signal from the background in s-SNOM.^{58, 142-145} In a very common approach, the tip-sample distance is modulated with a frequency typically in the 10-kHz-range.¹⁴⁶ Due to the highly nonlinear dependence of the scattered near-field signal on the tip-sample distance, higher harmonics of the modulation frequency are found in the signal. Demodulating at higher harmonics improves the near-field to background ratio and leads to improved contrast.¹⁴⁵

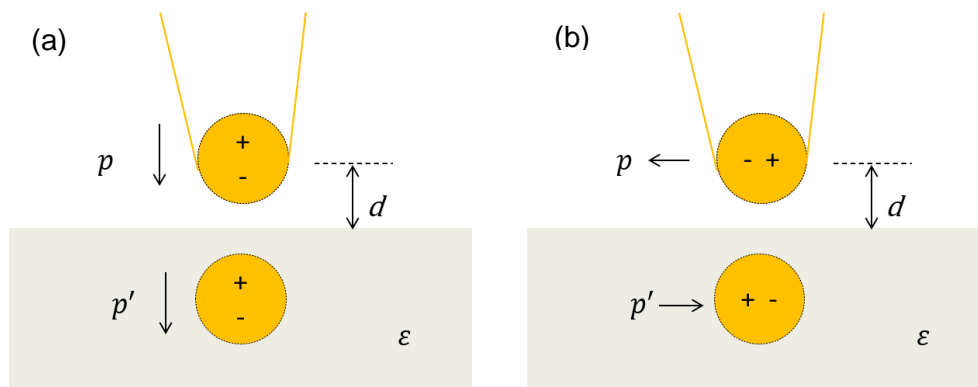


Figure 2.13 A typical probe-sample configuration of point dipole model in a uniform electric field (a) perpendicular and (b) parallel to the sample surface. The probe tip dipole p and sample image dipole p' are separated with a distance of $2d$.

In the point dipole model, both probe tip and sample are represented by polarizable spheres. Within small distances, tip and sample dipole moments are mutually enhanced.

This theory is suitable for single molecules, small particles, or a planar surface. As illustrated in figure 2.13, the probe is modeled as a polarizable sphere with radius of a and polarizability of α . Sample with complex dielectric function of ε is positioned close to the probe with distance of d . As applying an incident electric field E_0 perpendicular to the sample surface in panel (a), the probe sphere is excited, creating a dipole moment with polarization $p = \alpha E_0$. The polarization is the source of a point-dipole-like excitation at the tip position and emits a secondary field, $E_{dipole} = \frac{p}{2\pi d^3}$, which in turn induces an image dipole in the sample if the tip-sample-distance is roughly equal to or smaller than the apex radius of curvature. The image dipole has dipole moment determined by the complex dielectric function of the sample material, $p' = (\varepsilon - 1)/\varepsilon + 1) \cdot p$, and locates at a distance of $2d$ to the tip. It emits an electric field $E_{ID} = \frac{p'}{16\pi d^3}$ which enhances the incident field at the tip position, such that the actual tip dipole moment becomes:¹⁴⁵

$$p = \alpha(E_0 + E_{ID}) = \frac{\alpha(1+\beta)}{1 - \frac{\alpha\beta}{16\pi d^3}} E_0 \quad (2.69)$$

where $\alpha = \frac{4\pi a^3(\varepsilon_p - 1)}{\varepsilon_p + 2}$ with probe dielectric function ε_p , and $\beta = \frac{\varepsilon - 1}{\varepsilon + 1}$.

Hence, the output signal of a tip-sample couple system is equivalent to an effective response to the incident electric field. The effective polarizability for the incident field perpendicular to the sample surface is:

$$\alpha_{eff\perp} = \frac{\alpha(1+\beta)}{1 - \frac{\alpha\beta}{16\pi d^3}} \quad (2.70)$$

As the incident electric field parallel to the sample, the image dipole has an opposite sign to the tip dipole as shown in figure 2.13(b), and the corresponding effective polarizability:

$$\alpha_{eff\parallel} = \frac{\alpha(1-\beta)}{1 - \frac{\alpha\beta}{32\pi d^3}} \quad (2.71)$$

Obviously, the response of tip in such dipole-dipole coupling model is strongly distance-dependent. Here we take an example system applying a gold tip and 780 nm excitation light and calculate the scattering cross section of the tip apex according to $C_{sca} =$

$\frac{k^4}{6\pi} |\alpha_{eff}|^2$ according to the Rayleigh scattering Equation (2.16). Figure 2.14 discuss the C_{sca} dependency on the tip-sample distance for different incident electric field polarizations, tip radii, dielectric function (sample materials).

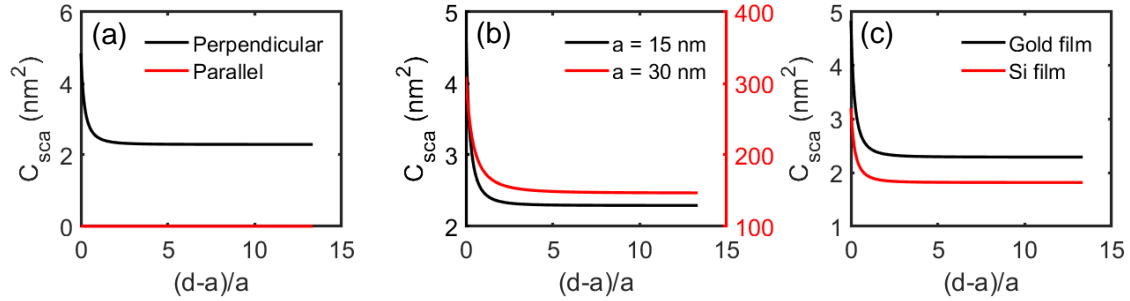


Figure 2.14 Effective polarizability dependency on the tip-sample distance for (a) perpendicular (solid line) and parallel (dashed line) polarization of the incident electric field for 15 nm radius gold tip, (b) 15 nm (black curve) and 30 nm (red curve) radius gold tip under perpendicular polarization excitation on a gold film, (c) gold and silicon sample for a 15 nm radius gold tip under perpendicular polarization excitation.

When excitation electric field polarization is parallel to the sample, the tip and image dipole cancel in the effective polarizability. Figure 2.14 (a) compares the scattering of a gold tip with 15 nm radius under excitation either parallel or perpendicular to the gold surface. An exponential increase is observed as tip-sample distance is reduced, which fits the evanescent feature of near-field. Clearly, the parallel polarization yields weaker response because the image dipole is out of phase to the probe dipole therefore destructively interference. From the aspect of tip size, the spatial resolution of SNOM could be improved by applying sharper tips. However, a smaller scatterer weakens near-field enhancement (as indicated in Figure 2.14 (b)), because the Rayleigh scattering is proportional to the sixth power of radius. Another important factor influencing the near-field signal is the material dielectric function. Panel (c) of Figure 2.14 depicts the perpendicular effective polarizability of gold tip for gold and silicon sample. Obviously, the sample with higher dielectric function is beneficial to the tip and sample enhancement. For a broad bandwidth measurement, a sample that is resonant in the incident light range generally displays a resonance in the near-field signal. From this point of view, SNOM

enables identifying the local property of nanostructures.

Due to the strong distance-dependence of the dipole-dipole coupling, the near-field signal resembles an exponential signal decreasing with tip-sample distance becoming larger, and a phase of φ_{NF} due to the dipole-dipole coupling is taken into account:¹⁴⁷

$$E_{NF}(z) = E_{NF,0} \cdot e^{-\frac{d}{d_0}} \cdot e^{i\varphi_{NF}} \quad (2.72)$$

Here d_0 is the near-field decay length, which depends on the tip radius of curvature. In contrast, the background field scattered from the tip shaft oscillates in a sinusoidal fashion and the variation period is in the light wavelength scale. Due to the pathway difference of two fields, the background signal E_B has a phase shift with respect to the near field. The pathway of E_B is longer the tip-sample distance d plus a constant distance \bar{d} , which combines the distance from the apex, at which the backscattering from the shaft occurs. The pathway multiplied with the wave vector $k = \frac{2\pi}{\lambda}$ determines the phase of E_B , together with a phase shift φ_B that can occur due to the reflection the background field is:

$$E_B(z) = E_{B,0} \cdot e^{i2k(d+\bar{d})} \cdot e^{i\varphi_B} \quad (2.73)$$

The other background field scattered from the sample E_s is independent of the tip-sample distance. Both near-field and tip scattered background field are varying as a function of the tip-sample distance, while their dependency is essentially different. If the tip vibrates above the sample surface, the rapidly changing $E_{NF}(z)$ generates light scattering at higher harmonics, while background is confined mostly to the DC term and lower harmonics. This is the main accordance to distinguish two contributions.

When the tip-sample distance d varies as a periodic function with period T : $d = d(t) = d(t + T)$, where $T = f^{-1} = 2\pi\Omega^{-1}$ is the inverse of the tip modulation frequency. The distance can be written as a sinusoidal function with the modulation amplitude M , centered at the average tip-sample distance \bar{d} :

$$d(t) = \bar{d} + M \cdot \cos(\Omega t) \quad (2.74)$$

Thus E_B and E_{NF} are temporally periodic function with the same period T :

$$E_B(\bar{z}, t) \approx E_{B,0} \cdot e^{ik\bar{d}+i\varphi_B} \cdot e^{ikM\cos(\Omega t)} \quad (2.75)$$

$$E_{NF}(\bar{z}, t) \approx E_{NF,0} \cdot e^{i\varphi_{NF}} \cdot e^{-\frac{d}{d_0}} \cdot e^{-\frac{M}{d_0 \cos(\Omega t)}} \quad (2.76)$$

The explicitly time-dependent factors of these two fields can be approximated as Fourier sums:

$$E_B(\bar{z}, t) \approx E_{B,0} \cdot e^{ik\bar{d} + i\varphi_B} \cdot \sum_{n=-\infty}^{\infty} b^{(n)} e^{in\Omega t} \quad (2.77)$$

$$E_{NF}(\bar{z}, t) \approx E_{NF,0} \cdot e^{i\varphi_{NF}} \cdot e^{-\frac{\bar{d}}{d_0}} \cdot \sum_{n=-\infty}^{\infty} c^{(n)} e^{in\Omega t} \quad (2.78)$$

Here we have introduced the complex Fourier coefficients $b^{(n)}$ and $c^{(n)}$ of the background field E_B and the near field E_{NF} , respectively, where n is the harmonic order of the tip modulation frequency. The Fourier coefficients can be easily calculated:

$$b^{(n)} = \frac{1}{T} \int_0^T e^{ikM \cos(\Omega t)} \cdot e^{-in\Omega t} dt = (i)^n \cdot J_n(2kM) \quad (2.79)$$

$$c^{(n)} = \frac{1}{T} \int_0^T e^{-\frac{M}{z_0 \cos(\Omega t)}} \cdot e^{-in\Omega t} dt = (-1)^n \cdot I_n\left(\frac{M}{z_0}\right) \quad (2.80)$$

The Fourier coefficients for the background field $b^{(n)}$ are given by Bessel functions of the first kind and of order n , J_n , which displays oscillating line shape as illustrated in figure 2.8. Fourier coefficients $b^{(n)}$ of even order are real values, while those of odd orders are imaginary. This means that the phase of the background field shifts with each modulation order. The Fourier coefficients of the near-field are modified Bessel functions of the first kind and of order n , I_n that exponentially increasing and are all real. The absolute of the Fourier coefficients as a function of demodulation order 1 to 4 are shown in a bar diagram in figure 2.15, specifically for a wavelength $\lambda = 600$ nm and the tuning fork modulation amplitude $M = 12$ nm. The red bars are the background-field coefficients normalized to the zeroth order coefficient, i. e., $\left| \frac{b^{(n)}}{b^{(0)}} \right|$, and the blue bars the according near-field coefficients $\left| \frac{c^{(n)}}{c^{(0)}} \right|$. It is noteworthy that both coefficients decrease with demodulation order, and the relative strength of the background decreases much more rapidly than that of the near field. This implies that the near-field contribution becomes more clearly visible as the demodulation order increases. The increase of the near-field-to-background-ratio with demodulation order forms the basis for higher-order demodulation SNOM.

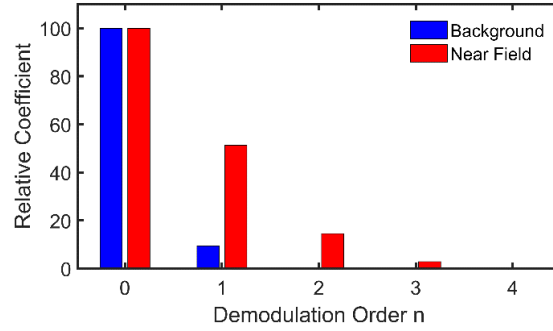


Figure. 2.15 Relative amplitude of the Fourier coefficients $b^{(0)}$ to $b^{(4)}$ (red bars) and $c^{(0)}$ to $c^{(4)}$ (blue bars) normalized to $b^{(0)}$ and $b^{(0)}$, respectively, as a function of demodulation order n . The amplitude of both decreases with demodulation order, but the background-field coefficients $b^{(n)}$ decreases much more rapidly than the near-field coefficients $c^{(n)}$.

To precisely reveal our experiment, we simulate the signal by quantifying the tip modulation, electric field interference, and lock-in amplifier demodulation as follows. Firstly, the tip vibrating frequency is set as $f = 32kHz$, amplitude is $M = 12 nm$. In actual measurement, the minimum tip-sample distance is about $\bar{z} = 3 nm$. Figure 2.16 (a) shows the simulated tip vibration curve in the manner of $d(t) = \bar{d} + M \cdot \cos(\Omega t)$. Then, the near-field amplitude $E_{NF,0} = 2$ is approximated from $\sqrt{C_{sca}}$ when a gold tip is 3 nm away from a gold film. The amplitude and phase of background field from tip shaft as $E_{B,0} = 60$, and from sample surface as $E_s = 3$. The phase of three fields are $\varphi_B = 0, \varphi_{NF} = \pi$. Three electric fields can be determined according to Equation (2.75) and (2.76). The signal that is measured in the detector plane is proportional to the absolute square of the total field $E_{total}(\bar{z}, t) = E_B(\bar{z}, t) + E_{NF}(\bar{z}, t) + E_s$:

$$|E_{total}(\bar{z}, t)|^2 = |E_B(\bar{z}, t) + E_{NF}(\bar{z}, t) + E_s|^2 \quad (2.81)$$

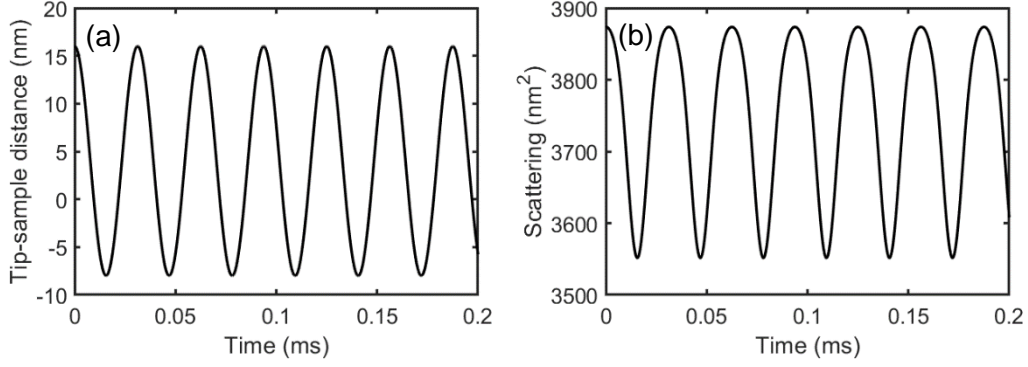


Figure 2.16 (a) Tip-sample distance modulation function and (b) the modulated total signal.

The resulted time dependent total intensity for optical wavelength of 780 nm is calculated as illustrated in figure 2.16 (b). Given the time dependent total intensity $|E_{total}(\vec{z}, t)|^2$, the power impinging on a detector is

$$P(\vec{z}, t) = \frac{1}{2} \epsilon_0 c A |E_{total}|^2 \quad (2.82)$$

Where A is the area of the detector. Multiplication with the detector efficiency η yields the output voltage $U(\vec{z}, t) = \eta \cdot P(\vec{z}, t)$. The demodulation is achieved by a lock-in amplifier which can be written as:

$$S_{nf}(\vec{z}) = \gamma \cdot \frac{1}{T} \int_{t-T}^{t'} \cos[n\Omega t + \theta] \cdot U(\vec{z}, t) dt \quad (2.83)$$

Here, the index nf denotes the demodulation frequency, γ is the gain parameter of the lock-in detector, and θ is the phase between modulation waveform and detected signal. When measuring $S_{nf}(\vec{z})$ with the lock-in detector, the influence of this phase is eliminated by actually recording the amplitude, i. e., the geometrical average of $S_{nf}(\vec{z}, \theta_1)$ measured for one phase setting θ_1 and $S_{nf}(\vec{z}, \theta_2)$ measured for a second phase setting $\theta_2 = \theta_1 + \frac{\pi}{2}$. In our calculation, the same effect is achieved easily by evaluating the integral of Equation (2.83) for $\theta = 0$.

Figure 2.17 shows the output amplitude of the lock-in amplifier for a detected signal in figure 2.16 (b), specifically for light wavelength of 780 nm. The Lock-in signal from the

first to the 8th harmonic are calculated for an integration time of 5 ms. The demodulation signal decreases rapidly with the demodulation orders and can be barely seen above fourth harmonic order.

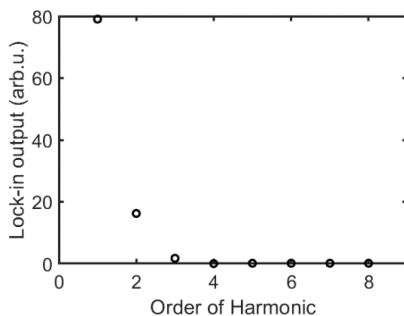


Figure 2.17 Lock-in amplifier output versus demodulation harmonic orders.

At last, the approach curves demodulated at the fundamental and at the second and third harmonic frequency are calculated. Figure 2.18 shows the amplitude of the lock-in-detector signal during the approach at the respective demodulation frequency. The optical signal demodulated at the fundamental tip modulation frequency, $1f$ in Figure 2.18 (a), shows a strong modulation with a period of ~ 300 nm, corresponding to half the wavelength of the excitation laser. This modulation is a result of the interference of the near-field and background field. The optical signal demodulated at the second harmonic, $2f$ in Figure 2.18 (b) shows a small modulation still. When demodulating at the third harmonic, however, $3f$ in figure 2.18 (c), there is a clear near-field contribution. The near-field signal resembles a strong exponential signal increase with a decay length of about 8 nm. The improved near-field-to-background-ratio with demodulation order forms the basis for higher-order demodulation SNOM. Additionally, the demodulated signal magnitude decreases with harmonic order.

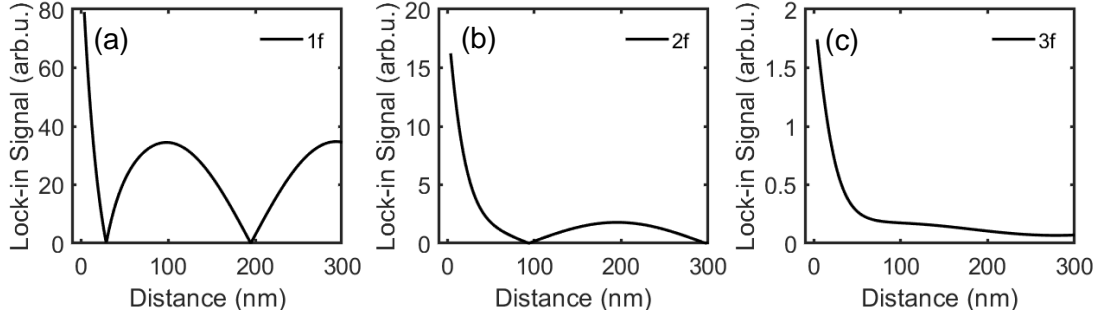


Figure 2.18 lock-in amplifier output as a function of tip-sample distance for (a) the fundamental and (b) the second, (c) third harmonic frequencies. The tip sample distance is adjusted by varying the \bar{z} in Equation 2.74

2.5 Homodyne and Heterodyne detection

As described in last section, the near-field is the dominant part in higher harmonic signal, however, a complete suppression of the unwanted background is challenging regardless of the harmonic order. Generally, the light field components that are scattered from the near field, from the diffraction-limited spot on the sample and from the tip shaft interfere and lead to the detection of a mixed intensity signal that cannot be disentangled, because mixing occurs at the electric field level. A general approach to enabling the discrimination of the different contributions is amplifying the near-field signal by homodyne, heterodyne, or pseudo-heterodyne mixing of the scattered signal with a well-controlled reference wave. In this session, we will introduce the working principle of homodyne and heterodyne scheme, and particularly discuss the improve of near-field strength and contrast in a homodyne detection combined SNOM.

Figure 2.19 (a) represents schematically a typical homodyne sSNOM. The tip-sample junction is illuminated with a monochromatic field at frequency ω . The reference field is a branch of the incident light E_R , and has a constant amplitude $E_{R,0}$ and phase φ_R . The tip-sample scattered fields E_B and E_{NF} together with E_R form the Michelson interferometer. According to equation (2.81) and (2.82), the detected intensity in this case is:

$$\begin{aligned}
I &= |E_B + E_{NF} + E_R|^2 \\
&= (E_B + E_{NF} + E_R)(E_B^* + E_{NF}^* + E_R^*) \\
&= \left| E_{R,0} e^{i\varphi_R} + E_{B,0} e^{ik\bar{d} + i\varphi_B} \cdot \sum_{n=-\infty}^{\infty} b^{(n)} e^{in\Omega t} + E_{NF,0} e^{ik\varphi_{NF}} e^{-\frac{\bar{d}}{d_0}} \cdot \sum_{n=-\infty}^{\infty} c^{(n)} e^{in\Omega t} \right|^2 \quad (2.84)
\end{aligned}$$

$$\begin{aligned}
I &= |E_{R,0}|^2 \\
&+ |E_{B,0}|^2 \sum_{n=-\infty}^{\infty} \sum_{m=-\infty}^{\infty} b^{(n)} b^{(m)*} e^{i(n-m)\Omega t} \\
&+ |E_{NF,0}|^2 e^{-2\frac{\bar{d}}{d_0}} \sum_{n=-\infty}^{\infty} \sum_{m=-\infty}^{\infty} c^{(n)} c^{(m)*} e^{i(n-m)\Omega t} \\
&+ \left(E_{R,0} E_{B,0} e^{ik\bar{d} + i(\varphi_B - \varphi_R)} \cdot \sum_{n=-\infty}^{\infty} b^{(n)} e^{in\Omega t} + c.c. \right) \\
&+ \left(E_{R,0} E_{NF,0} e^{ik(\varphi_{NF} - \varphi_R)} e^{-\frac{\bar{d}}{d_0}} \cdot \sum_{n=-\infty}^{\infty} c^{(n)} e^{in\Omega t} + c.c. \right) \\
&+ \left(E_{B,0} E_{NF,0}^* e^{ik\bar{d} + i(\varphi_B - \varphi_R)} e^{-\frac{\bar{d}}{d_0}} \sum_{n=-\infty}^{\infty} \sum_{m=-\infty}^{\infty} b^{(n)} c^{(m)*} e^{i(n-m)\Omega t} + c.c. \right) \quad (2.85)
\end{aligned}$$

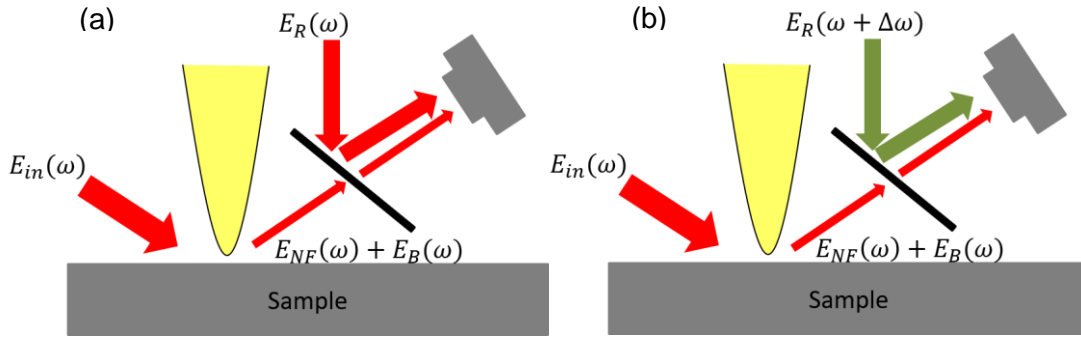


Figure 2.19 (a) Sketch of a heterodyned sSNOM containing an additional optical interferometer with a Δ frequency-shifted reference field E_R and the tip-sample scattered fields near-field E_{NF} and background E_B . (b) Homodyne optical system in which the detected light is the coherent superposition of E_R , E_{NF} and E_B .

There are six terms in the total intensity. The first three terms are the respective intensities of three fields. The intensity $|E_{R,0}|^2$ is not time dependent thereby is filtered out by lock-in amplifier. For nth order demodulated signal, the second intensity is nonzero only for the case of $m=0$, however $c^{(0)}$ is inexistent. Hence the second term is also filtered out. The later three terms correspond to the mutual interference among the near-field field, background field, and reference field. Obviously, the reference field strength can be adjusted to be several orders of magnitude higher than other fields, $E_{R,0} \gg E_{NF,0}, E_{R,0} \gg E_{B,0}$. On the other hand, the calculation of the Fourier coefficients in Figure 2.15 showed that the near-field and background contribution decreases rapidly with increasing demodulation order, such that $|E_{B,0}b^{(n)}| \ll |E_{B,0}b^{(0)}|$ for $|n| > 0$. With these assumptions the signal measured at the first and higher harmonic demodulation frequencies, S_{1f} to S_{4f} , can be approximated:¹⁴⁷

$$S_{1f}(\bar{z}) \approx \gamma\eta\varepsilon_0cA \cdot \left[-Re\{E_{R,0}E_{B,0}\}|b^{(1)}| \cdot \sin(k\bar{d} + \varphi_B) - Re\{E_{R,0}E_{NF,0}\}|c^{(1)}|e^{-\frac{\bar{z}}{z_0}} \cdot \cos(\varphi_{NF}) \right. \\ \left. - Re\{E_{B,0}E_{NF,0}\}|b^{(0)}||c^{(1)}|e^{-\frac{\bar{z}}{z_0}} \cos(k\bar{d} + \varphi_B - \varphi_{NF}) \right] \quad (2.86)$$

$$S_{2f}(\bar{z}) \approx \gamma\eta\varepsilon_0cA \cdot \left[-Re\{E_{R,0}E_{B,0}\}|b^{(2)}| \cdot \cos(k\bar{d} + \varphi_B) + Re\{E_{R,0}E_{NF,0}\}|c^{(2)}|e^{-\frac{\bar{z}}{z_0}} \cdot \cos(\varphi_{NF}) \right. \\ \left. - |E_{B,0}|^2|b^{(0)}||b^{(2)}| + Re\{E_{B,0}E_{NF,0}\}|b^{(0)}||c^{(2)}|e^{-\frac{\bar{z}}{z_0}} \cos(k\bar{d} + \varphi_B - \varphi_{NF}) \right] \quad (2.87)$$

$$S_{3f}(\bar{z}) \approx \gamma\eta\varepsilon_0cA \cdot \left[-Re\{E_{R,0}E_{B,0}\}|b^{(3)}| \cdot \sin(k\bar{d} + \varphi_B) - Re\{E_{R,0}E_{NF,0}\}|c^{(3)}|e^{-\frac{\bar{z}}{z_0}} \cdot \cos(\varphi_{NF}) \right. \\ \left. - Re\{E_{B,0}E_{NF,0}\}|b^{(0)}||c^{(3)}|e^{-\frac{\bar{z}}{z_0}} \cos(k\bar{d} + \varphi_B - \varphi_{NF}) \right] \quad (2.88)$$

$$S_{4f}(\bar{z}) \approx \gamma\eta\varepsilon_0cA \cdot \left[Re\{E_{R,0}E_{B,0}\}|b^{(4)}| \cdot \cos(k\bar{d} + \varphi_B) + Re\{E_{R,0}E_{NF,0}\}|c^{(4)}|e^{-\frac{\bar{z}}{z_0}} \cdot \cos(\varphi_{NF}) \right. \\ \left. + |E_{B,0}|^2|b^{(2)}|^2 + Re\{E_{B,0}E_{NF,0}\}|b^{(0)}||c^{(4)}|e^{-\frac{\bar{z}}{z_0}} \cos(k\bar{d} + \varphi_B - \varphi_{NF}) \right] \quad (2.89)$$

When the reference field strength is controllable and is adjusted to strong enough, $E_{B,0}|b^{(0)}| \ll E_R$ holds. The cross terms between higher-order coefficients within reference field dominate. Moreover, the faster decay of $|b^{(n)}|$ with increasing demodulation order nearly completely removes the influence of the background field at higher harmonics.

Eventually, the dominance of the near-field and reference field product $Re\{E_{R,0}E_{NF,0}\}|c^{(n)}|$ is a result of a homodyne interferometer. It is the most important conclusion in our measurement. We will use this to retrieve the near-field response of various samples.

The heterodyne version is sketched in Figure 2.18 (b). It incorporates a reference wave that has shifted frequency $\Delta\omega$ with respect to the illumination light source. E_B and E_{NF} are simply characterized by their amplitude and phase $(E_{B,0}, \varphi_B)$ and $(E_{NF,0}, \varphi_B)$. In comparison to homodyne technique, the interference term between reference field and either background field or reference field and near-field oscillates in a new frequency $\Delta\omega$, therefore the last three terms of equation (2.85) contain an additional frequency part. Here we only focus on the difference of two methods, hence the far-field detection of heterodyne scheme can be simplified as:¹⁴⁸

$$\begin{aligned}
I &= |E_B|^2 + |E_{NF}|^2 + |E_{NF}|^2 \\
&+ 2|E_B||E_{NF}| \\
&+ 2|E_B||E_R|e^{i(\Delta\omega t)} \\
&+ 2|E_{NF}||E_R|e^{i(\Delta\omega t)}
\end{aligned} \tag{2.90}$$

Keep in mind that the $|E_B|$ and $|E_{NF}|$ includes modulated by the tip oscillation. The sixth term which dominants at higher harmonics is proportional to:

$$E_{R,0}E_{NF,0} \cdot e^{i(\varphi_{NF}-\varphi_R)} \cdot e^{-\frac{\bar{d}}{d_0}} \cdot \sum_{n=-\infty}^{\infty} c^{(n)} e^{i(n\Omega \pm \Delta\omega)t} \tag{2.91}$$

In this case, the SNOM signal is obtained by lock-in detection at various frequencies $(n\Omega \pm \Delta\omega)/2\pi$. Similarly, to the homodyne detection method, the dominant output of the lock-in amplifier is independent of the background field. Moreover, in this amplitude the near-field strength is enhanced by the adjustable reference field. On the other hand, the phase channel in homodyne and heterodyne technique provides pure information on the phase delay of the optical near field relative to the reference field. This can evaluate the physical origin of the optical near field, such as plasmon resonance or electronic coupling in a nanostructure system.

3 Experimental setup and data processing

3.1 Overview over the optical setup

The experiments presented in this thesis were performed with a home-built sSNOM that has been presented in our previous work.^{147, 149} A part of content in this section has been modified from [1].

The home-built sSNOM incorporated in the sample arm of a Michelson interferometer is depicted schematically in Figure 3.1. Light from a Titanium:Sapphire laser (Femtolasers Rainbow), with a spectral bandwidth of around 150 nm and centered at a wavelength of 820 nm (see inset in the lower left of Figure 3.1), is used to illuminate the sample. The input power is set to 12 mW (in front of the interferometer setup). The direction of the electric field vector of the linearly polarized light can be rotated using a half-wave plate (HWP), and it's in a specific experiment set to either s-polarization (in the sample plane) or p-polarization (along tip axis). Incident light passes a beam splitter (BS), where 20% is reflected and is then focused on the sample at an angle of 65° using a reflective microscope objective (MO, Beck Optronics Solutions, model 5003-000) with NA=0.4 and working distance of 14.5 mm. Using a reflective MO minimizes dispersion, which would otherwise result in a varying fringe spacing in the recorded spectral interferogram. 80% of the incident light is transmitted at the BS and serves as a reference field E_R in our measurements. For this, the power is adjusted by a variable grey filter before light is reflected back to the BS by a mirror (M_R) that forms the reference arm of the Michelson interferometer. The reference arm length is adjusted to be shorter than the sample arm by $\sim 100 \mu\text{m}$ in order to enable spectral interference with a convenient fringe spacing and then kept constant during the measurement. To access the near-field region, a sharp gold nanotaper is brought in close proximity to the sample surface. Scattered light is collected in backwards direction by the MO. The part that is transmitted through the BS is overlapped with the reference field E_R , and the resulting superposition is collected for detection. Typically, we employ two different detection methods. In the first case, the reference arm is blocked and the signal back-scattered from the focus region is detected with an avalanche photodiode (APD, Hamamatsu, model C5331-02). It is further

processed by a lock-in amplifier (Zurich Instruments HFLI), with the tip modulation frequency as the reference signal. The signal demodulated at the fundamental tip modulation frequency as well as those demodulated at its second, third, and fourth harmonic are obtained and stored. We label these spectrally unresolved signals produced by the lock-in amplifier with S_{1f} , S_{2f} , S_{3f} , and S_{4f} . In this case, with the reference arm blocked, the signal detected by the APD is constituted of light scattered out of the near field by the sharp tip, E_{NF} , and of unwanted background field E_B , scattered from the sample and from the tip shaft. Together, this results in a voltage proportional to $|E_{NF} + E_B|^2$. While for demodulation at the fundamental tip modulation frequency we expect the signal S_{1f} to carry a significant amount of background. For the higher-order demodulated signals, the term $|E_{NF}|^2$ becomes dominant over background and mixed terms due to the strongly nonlinear dependence of the near field signal on the tip-sample distance. With the tip in close vicinity to the sample surface, i. e., with a minimal tip-sample distance of ~ 4 nm, the light focus position is aligned to maximize S_{3f} or S_{4f} signal that is monitored by the Zurich instrument. During a measurement, the positions of the tip and the laser focus are fixed, and the sample can be moved in three dimensions.

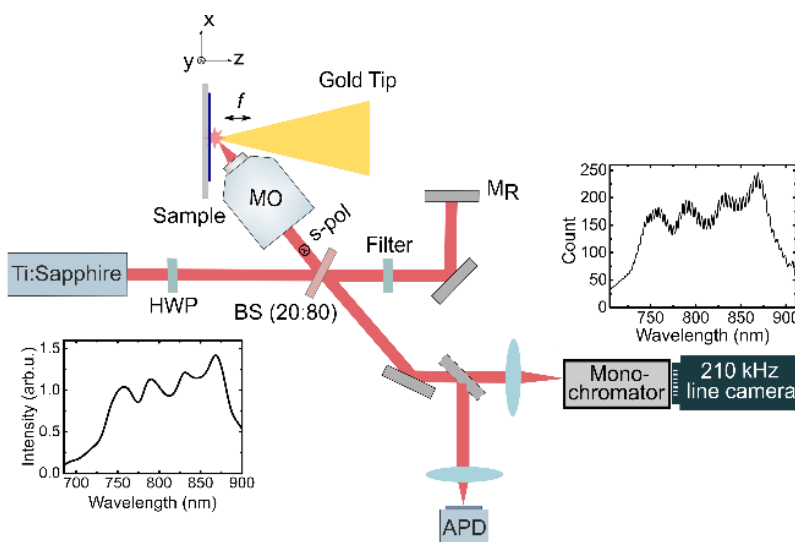


Figure. 3.1 Experimental setup for broad-bandwidth interference SNOM (BISNOM). Light from a broad-bandwidth titanium:sapphire laser (see the spectrum in the inset in the lower left) is focused onto the sample by an MO. The polarization is controlled by an HWP. A

sharply etched gold tip is brought close to the sample to scatter light from the near-field region to the far field. The scattered light is collected by the MO. The larger part of the incident light (80%) is transmitted through a BS to the reference arm of a Michelson interferometer, adjusted in power by a variable gray filter, reflected (MR), and superimposed with the light from the sample arm at the BS (see the spectral interferogram in the inset in the lower right). The light is detected either by an APD or by a monochromator followed by a 2D camera.

In the second case, for spectrally resolved measurements, the reference arm is unblocked, and the output of the Michelson interferometer is steered to the monochromator (Princeton Instruments, IsoPlane-160) equipped with a fast line camera (e2V Aviiva EM4 with 512 pixels). The line camera has a maximum readout rate of 210 kHz, and we typically record 60.000 consecutive spectra with the maximum read-out rate. When recording spectra with the fast line-camera, the fundamental and higher-order demodulated signals are extracted in post-processing. The numerical generation of those demodulated spectra and the extraction of the sample's transmission function with sub-diffraction-limit spectral resolution will be described in more detail later in the chapter. In short, the recorded values are considered separately, i. e., for each wavelength component of the spectrum, the line camera records a time series of 60.000 values. A Fourier series expansion is performed around multiples of the tip modulation frequency. For each pixel, the so determined Fourier coefficients are quantities analogous to the signals generated by the lock-in amplifier in the monochromatic measurements. Assembling the respective Fourier components for all camera pixels results in spectra $S_{1f}(\lambda)$ to $S_{4f}(\lambda)$, demodulated at the first to fourth harmonic of the tip modulation frequency. As previously discussed, for higher order demodulation these spectra produce $Re\{E_{NF}E_R\}$ dominates such that the background field E_B is strongly suppressed.

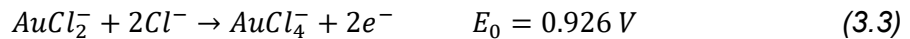
3.2 Tip fabrication and vibration

In scanning probe microscopy, tip production is of great importance. Especially for scattering SNOM, the tip apex radius determines the spatial resolution and the tip surface roughness greatly affects the far-field strength scattered from the tip shaft. Therefore, preparing smooth and sharp tapers appears to be a crucial issue in sSNOM. In this thesis,

the near-field probes are prepared by electrochemical etching.¹⁵⁰

Polycrystalline gold wires with a diameter of 125 μm (Advent Research Materials) are first annealed under 800 $^{\circ}\text{C}$ for 8 hours in argon atmosphere. The annealing process increases the grain size of the polycrystalline gold wires. It is important to produce single-crystalline grains of that are several tens of micrometers in length, such that no grain boundaries are in the volume that is electrochemically etched to form a sharp tip in the following step. In the absence of grain boundaries, the etching process typically leaves a smooth defect-free surface.¹⁵¹

Then, gold tips are prepared by electrochemically etching the monocrystalline gold wires in hydrochloric acid (Sigma-Aldrich, purity: 37%) as sketched in figure 3.2(a). The gold wire and a platinum ring constitute the two electrodes. They are both immersed in the solution and suspend slightly beneath the surface. The voltage applied between the two electrodes is supplied by a function generator. Figure 3.2 (b) depicts the rectangular voltage with 3 kHz frequency, peak-to-peak voltage of $V_{pp} = 7.5 \text{ V}$, 10% duty circle and 250 mV DC offset. As the voltage is turned on, the following chemical reactions take place in the solution for varied electrode potential E_0 :¹⁵²



Meanwhile, a great amount of Cl^- ions are consumed. A temporal depletion of Cl^- around the Au wire leads to the formation of gold oxides, which passivates the gold electrode and decreases the reaction current. Subsequent Cl^- supply from the bulk solution dissolves the oxide as AuCl_4^- , producing O_2 . As a result, the exposed bare gold surface re-consumes Cl^- , increasing the reaction current. We adopted the AC supply such that Cl^- ions are efficiently resupplied during the duty-cycle, and the current fluctuation is reduced.

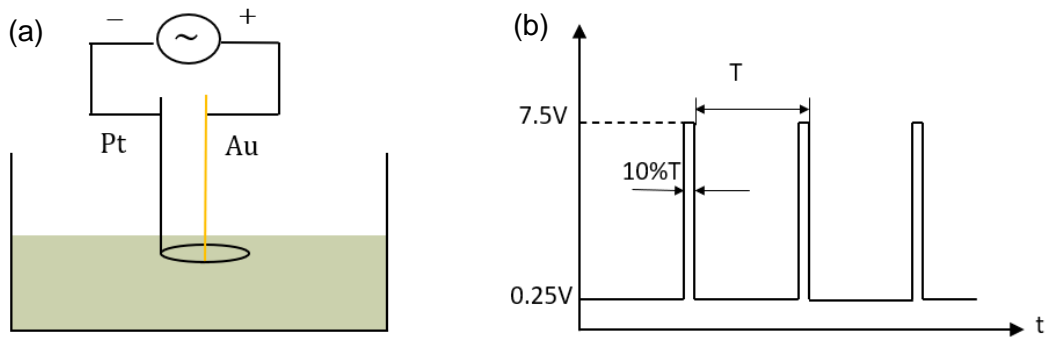


Figure 3.2 (a) Schematic of etching procedure gold wire. A gold wire and a platinum ring with diameter of 5 cm is dipped in HCl solution. (b) The periodic voltage pulses applied by a function generator

When the Au wire is immersed in the HCl, a meniscus around the wire is observed at the liquid/solid interface. The reactions in Equation (3.1)-(3.3) occur faster in this meniscus region than in the bulk solution.¹⁵³ Therefore, the wire within the meniscus area is observed to be shrinking and the meniscus simultaneously moves down. When the shrinking region is too narrow to support the weight of wire below solution surface, the neck breaks in two parts and the lower part drops off forming a sharp tip. The etching is terminated automatically. During the etching process, a bubbling effect is observed owing to side reactions of O_2 and Cl_2 evolution.

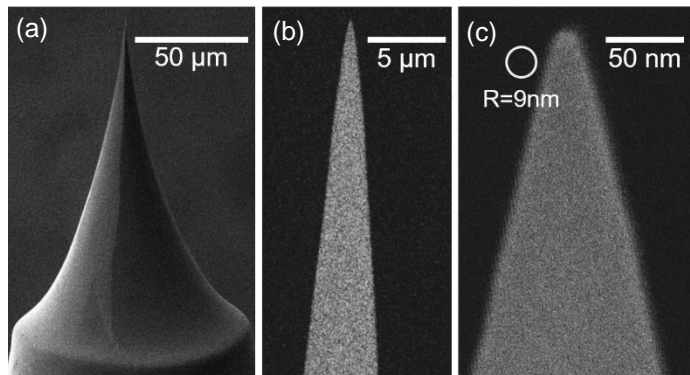


Figure 3.3 Scanning electron microscopy (SEM) images of a typical gold taper. (a) The single-crystalline sharp gold taper has a smooth surface. (b) High magnification image of

the front part with an even profile. (c) The apex of the tip exhibits a radius of curvature of less than 10 nm with an opening angle around 30°.

The etched tips are then characterized by a scanning electron microscope (FEI Helios NanoLab 600i). A suitable tip ideally has a radius of curvature below 20 nm, an opening angle between 10° to 40° and a smooth surface. Figure 3.3 depicts a typical gold tip produced by the described method. The side-view in panel (a) is the light incident facet and has an overall even and smooth surface. More importantly, there are no defects visible on the last tens micrometers from the apex. A closer view of the tip end demonstrates the apex radius of 9 nm and opening angle of 30°.

3.3 Tuning fork

Practically, a precise control of the tip-sample distance is a stringent condition of near-field optical microscope to bring the sample to the vicinity of the probe with a precision of nanometers, meanwhile, a constantly smooth scan of the sample surface need to be guaranteed. In contact mode, the tip experiences both a longitudinal compressive force and a lateral shear force, and such force varies along with the surface topography. Hence one of the distance control methods is based on the optical detection of the force acting on the tip.¹⁵⁴⁻¹⁵⁸ In such detection modes, the tip is vibrated either parallel (shear force mode) or perpendicular (tapping mode) to the sample surface at a mechanical resonance. The vibration amplitude is optically detected by differential interferometry or by the intensity of a laser beam focused on the tip. Despite the reliable operation, this method is not technically convenient, and the light path may induce an undesired optical background. Alternatively, the piezoelectric technique utilizing quartz tuning fork was introduced by Karrai and Grober^{159, 160}. The piezoelectricity of quartz crystal allows mechanical excitation of tuning fork and convert it to a voltage signal and vice versa.

A commercial quartz tuning fork (Auris TC26, UV curing glue Cyberbond U3200) is encased in vacuum-sealed canister, and resonant at ~32 kHz. After removing the metallic outer can, a gold tip is glued on one prong along the tuning fork and an equally sized gold wire is fixed on the top of the other prong. The tip is then aligned with its axis along the z-axis, i. e., the sample surface normal, and the tuning fork is driven with an AC voltage such that the tip moves back and forth along the z-axis. The bending amplitude of the

prongs is maximum at its resonance frequency, and this mechanical oscillation in turn generates an oscillation potential which is the 'signal' measured by a lock-in amplifier. A typical resonance of the piezoelectric signal is shown in Figure 3.4 (a). The quality of factor is defined as $Q = f_0/\Delta f$, where f_0 is the resonant frequency and Δf is the full frequency width at half-maximum of the resonance curve. When freely vibrating in air, a tuning fork has a Q of 9000. Such a high quality factor enables the tuning fork sensitive to sub hertz shifts, which results in a high force resolution.¹⁶¹ This is the main advantage of tuning fork over the conventional silicon cantilever. Figure 3.4 (b) illustrates the resonance curve of the tuning fork with a tip glued on one prong and a balance gold wire glued on the other prong. The fork resonance is shifted to 26.91 kHz and the quality of factor drops to 6700.

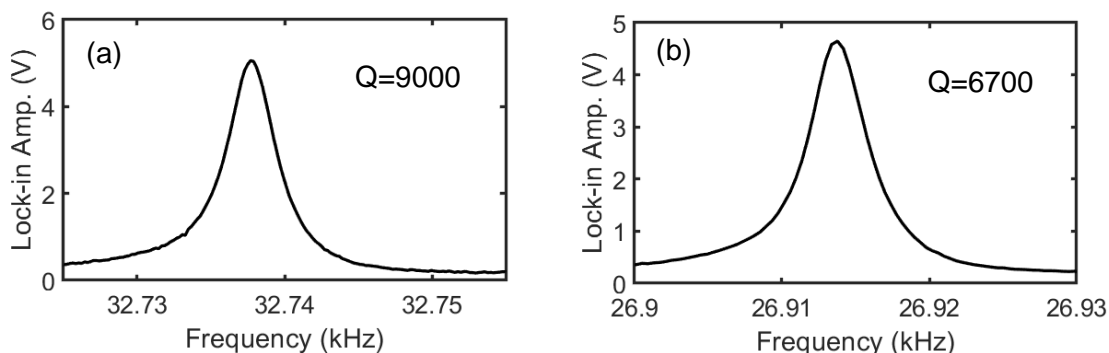


Figure 3.4 Amplitude of the Lock-in amplifier signal as function of the driving frequency for (a) a tuning fork in air, (b) the tuning fork with a gold tip and a balancer glued on two prongs. The quality of factor Q is calculated using the resonance frequency and the full width frequency width at half-maximum of the output amplitude.

In the experiment, the tuning fork works at the resonance frequency. When the sample surface is approached to tens of nanometers of a sample surface, the lock-in amplitude decreases due to the tip-sample interaction. The relationship of this force and the output voltage is given by:¹⁶⁰

$$|F_s| = \left(1 - \frac{V}{V_0}\right) \cdot k \cdot |x_0| / (Q \cdot \sqrt{3}) \quad (3.4)$$

where $\frac{V}{V_0}$ is the normalized piezoelectric signal amplitude at resonance frequency. x_0 and

Q are the tip amplitude and quality of factor when tip is away from the sample. k is the static compliance of one prong and can be inferred by $k = m_e \omega_0$ with $\omega_0 = 2\pi \cdot f_0$. The effective mass is determined by $m_e = 0.2427\rho \cdot (Ltw)$, with the density of quartz $\rho = 2650 \text{ kg/m}^3$ and the fork geometrical dimensions (length L , width w and thickness t). Applying the parameters of the tuning fork used in our measurement ($L = 3.2\text{mm}$, $w = 400\mu\text{m}$, $t = 360\mu\text{m}$, $f_0 = 26.91\text{kHz}$), a typical static compliance is $k = 8.47 \frac{\text{kN}}{\text{m}}$. Using $Q = 6700$ and $|x_0| = 12 \text{ nm}$, a signal amplitude duction of 2% corresponds to an interaction force of $|F_S| = 8.3 \text{ nN}$. During a sSNOM scan, the tip-sample distance is controlled by adjusting the sample z-position using the piezoelectric signal $\frac{V}{V_0}$ as a setpoint.

3.4 Near-field spectroscopy with homodyne detection

To realize near-field spectroscopic technique, the reference arm is incorporated, namely the light reflected from the reference mirror is superimposed with the signal scattered out of the focus area on the sample by the near-field prober. The length of either arm is about 150 mm, and the reference arm is normally shorter than the sample arm by a few hundred micrometers. This path length difference is chosen to be moderately large such that the delay time can easily be separated from the DC background in time domain, at the same time the spectral interference caused fringe spacing is large enough to be resolved by a detector. The output of the Michelson interferometer is collected by the fast line camera with a maximal readout rate of $f_{camera} = 210 \text{ kHz}$. In the measurement, the frame acquisition rate of the line camera is normally set to the highest value such that high order harmonic optical signal can be achieved. On the other hand, for each measurement position, $N_{spec} = 60000$ frames are accumulated, which corresponds to an integration time of about 280 ms, to get a good signal-to-noise ratio.

3.4.1 Fast camera data

Figure 3.5 (a) illustrates 60.000 spectra recorded consecutively at position on gold. The spectral wavelength abscissa correlates to the 512 pixels of camera chip, and it could be changed as the incidence coupling to the monochromator is different, therefore it is calibrated for different measurement. In the vertical direction, time increases from bottom

to top, and the count per pixel is color-coded. Evidently, the interference fringes swing in the integration time, indicating the arm length difference varies during a measurement. The sample arm in the interferometer including the near-field probe and sample is housed inside a foam-covered box for acoustic noise suppression, hence the arm length delay drift could be caused by a jittering reference arm mirror. The prior step of spectral data analysis is correcting such effect. The panel (b) depicts a typical spectrum, and the maximal intensity count reaches 3600 for a full capacity of 4096 (12-bit depth).

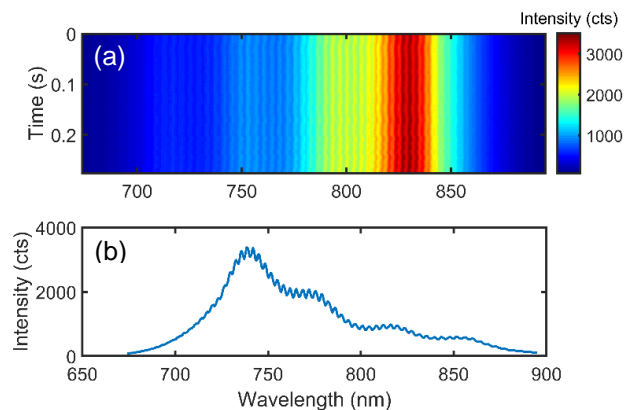


Figure 3.5 (a) Counts recorded by the fast line camera, color-coded as a function of wavelength and time. (b) One exemplary spectrum from panel (a).

For further quantitative analysis, the data in wavelength units is converted to equidistant distributed energy axis, based on the principle that the signal values in energy domain is corrected to retain the power spectral density according to:¹⁶²

$$f(E)dE = f(\lambda)d\lambda \quad (3.5)$$

where $f(E)$ and $f(\lambda)$ corresponds to the spectrum in energy and wavelength unit, respectively. Figure 3.6 shows the converted spectra in energy units.

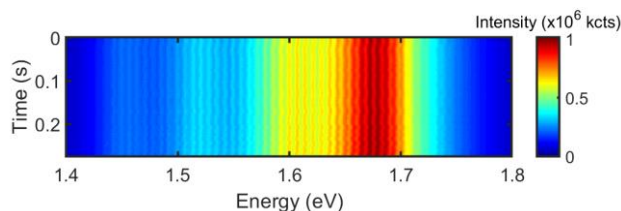


Figure 3.6 Spectra in energy domain converted from figure 3.5.

Before further analyzing such 2D spectral data, I will firstly demonstrate a method of correcting the time delay drift (wavy fringes) in the camera data by simulating a spectral interferogram signal like the measurement data, then apply such processing method on the measurement data to achieve spectral interferogram data with straight stripes. Moreover, the Fourier transform technique is illustrated to retrieve an input Lorentzian resonance introduced in the sample arm. This technique will be utilized on BISNOM data analysis in chapter 5.

3.4.2 Spectral interference simulation

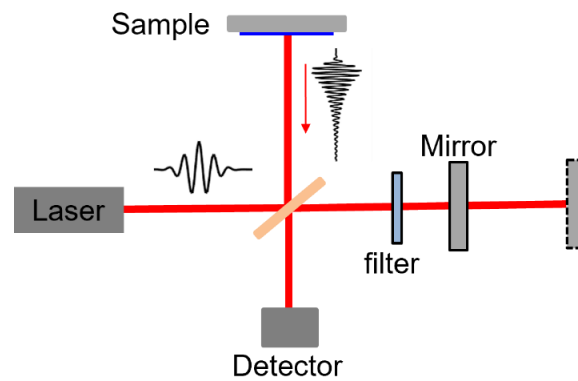


Figure 3.7 Michelson interferometer. The incident light is divided into two parts by a 45° oriented 50/50 beam splitter (BS). Half of the incidence is reflected to a sample surface, and the remaining part transmits through the BS and is reflected by a silver mirror to the BS, forming the reference arm of the interferometer. The reference mirror is movable to vary the path length, and the reference field strength can be adjusted by a grey filter.

To mimic the rainbow laser source used in the measurement, I introduce a broadband width light which is an ultrashort pulse in the time domain (as depicted in the inset of figure 3.7):

$$E_0(t) = |E_0| \cdot e^{-2\ln(2)\frac{(t-t_0)^2}{T^2}} \cdot \cos(\omega_c \cdot t + \varphi_{CE}) \quad (3.6)$$

Where $|E_0|$ is the field amplitude which is set as 1, $t_0 = 0$ is the time when the pulse is centered, and $T = 4 f_s$ is the full width at half maximum, ω_c is the Gaussian envelope

center frequency ($\hbar\omega_c = 1.51 \text{ eV}$), $\varphi_{CE} = 0$ is the carrier-envelope phase at the BS. The incident light spectrum is given by the Fourier transformation of the pulse $E_0(t)$, as shown in figure 3.8 (a).

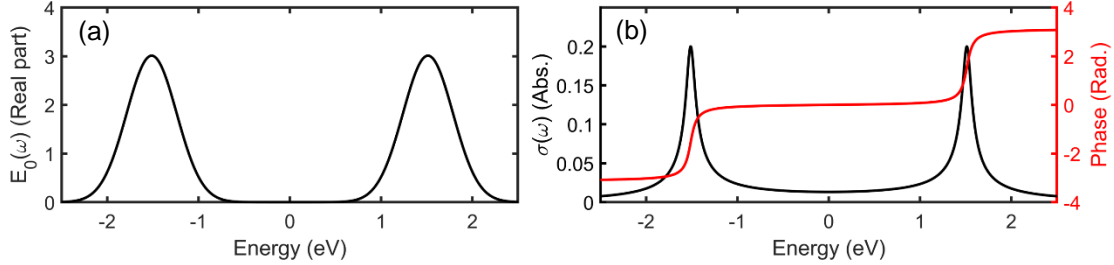


Figure 3.8 Simulation of (a) incident electric field $E_0(\omega)$, and (b) a Lorentzian resonance of the sample.

This incident light is divided into two paths by a BS, one of which transmits through the BS and is reflected by a mirror. The position of the mirror is movable such that the reference arm length is varied to be different from the other path length. An ND filter is inserted to adjust the reference field intensity without varying the spectral shape, and the transmission efficiency of the filter is expressed by $t_f(\omega) = |t_f|e^{i\varphi_f(\omega)}$ with $|t_f| = 0.7$. Therefore, the reference field reflected by the BS is given by $E_1(\omega) = \frac{1}{4} \cdot t_f^2(\omega)E_0(\omega) \cdot e^{i\varphi_1}$, where phase φ_1 is generated by a time delay of L_1/c_0 and L_1 is the additional optical length of $E_1(\omega)$ in comparison to the incident field $E_0(\omega)$ at the BS.

The remaining part of the incidence is reflected by a sample surface with a reflection coefficient of $\sigma(\omega) = |\sigma(\omega)|e^{i\varphi_\sigma}$. For simplification, this sample response coefficient is assumed as a Lorentzian line shape $\sigma(\omega) = A_\sigma\gamma_\sigma\left(\frac{1}{\omega+\omega_\sigma+i\gamma_\sigma} - \frac{1}{\omega-\omega_\sigma+i\gamma_\sigma}\right)$, where the resonant frequency and line width is $\hbar\omega_\sigma = 1.51 \text{ eV}$, $\hbar\gamma_\sigma = 50 \text{ meV}$, respectively, and the amplitude is taken as $A_\sigma = 0.2$. Figure 3.8 (b) shows the simulated Lorentzian response in which the phase has a π jump at the resonant energy position. Thus the reflected field from the sample arm is $E_2(\omega) = \frac{1}{4}\sigma(\omega)E_0(\omega) \cdot e^{i\varphi_2}$, where φ_2 is generated by a time delay L_2/c_0 of $E_2(\omega)$ in comparison to the incident field $E_0(\omega)$ at the BS.

Hence, the detected interference signal is denoted as:

$$\begin{aligned}
S_s(\omega) &= |E_1(\omega) + E_2(\omega)|^2 \\
&= \frac{1}{16} |E_0(\omega)|^2 (|t_f|^4 + |\sigma(\omega)|^2 + |t_f|^2 |\sigma(\omega)| e^{i(\Delta\varphi - \varphi_\sigma)} + cc.) \quad (3.7)
\end{aligned}$$

Where $\Delta\varphi = \varphi_f + \varphi_0$ is the setup introduced phase, $\varphi_0 = \varphi_1 - \varphi_2 = \frac{\Delta L}{c_0} \cdot \omega$ is the optical path length difference generated phase, and it is the factor that introduces delay drifts when ΔL varies.

Before simulating an interferogram analogous to the experimental data depicted in figure 3.6, I will firstly discuss the interferogram in time domain for the simulated signal $S_s(\omega)$ in three cases $\Delta\varphi$:

- (1) The first case assumes the transmission coefficient phase φ_f is 0 and φ_0 is negative with $\Delta L = -900 \text{ nm}$. Figure 3.9 (a) exhibits the field amplitude of $E_1(\omega)$ and $E_2(\omega)$, as well as the phase $\varphi_0 = -300 \text{ fs} \cdot \omega$ (red curve). According to the shift theorem of Fourier transform, such a linear phase φ_0 in frequency domain corresponds to a delay (a shift) in time domain. Figure 3.9 (d) displays the interferogram $s(t) = \mathcal{F}^{-1}[S_s(\omega)]$, which is composed of three parts, one center peak $s^0(t)$ and two symmetric sidebands $s^{+/-}(t)$ as expressed:

$$\begin{aligned}
s^0(t) &= FT^{-1} \left\{ 1/16 \cdot |E_0(\omega)|^2 (|t_f|^4 + |\sigma(\omega)|^2) \right\} \\
s^+(t) &= FT^{-1} \left\{ 1/16 \cdot |E_0(\omega)|^2 \cdot |t_f|^2 |\sigma(\omega)| e^{i(-\varphi_\sigma + \Delta\varphi)} \right\} \\
s^-(t) &= FT^{-1} \left\{ 1/16 \cdot |E_0(\omega)|^2 \cdot |t_f|^2 |\sigma(\omega)| e^{i(-\varphi_\sigma - \Delta\varphi)} \right\} \quad (3.8)
\end{aligned}$$

where FT^{-1} denotes an inverse Fourier transformation. $s^0(t)$ denotes the zero delay peak (dc peak), and $s^+(t)$ and $s^-(t)$ corresponds to the positive and negative peak (ac peak) that carry identical amplitude information. In the central peak, the incident laser $|E_0(t)|^2$ dominates such that exhibits a Gaussian profile, while the shape of the side peak is determined by the time structure of $FT^{-1}\{|\sigma(\omega)| \cdot |E_0(\omega)|^2\}$, namely a convolution of an exponential function and a Gaussian function. Hence an exponential decay appears shortly after the side peak.

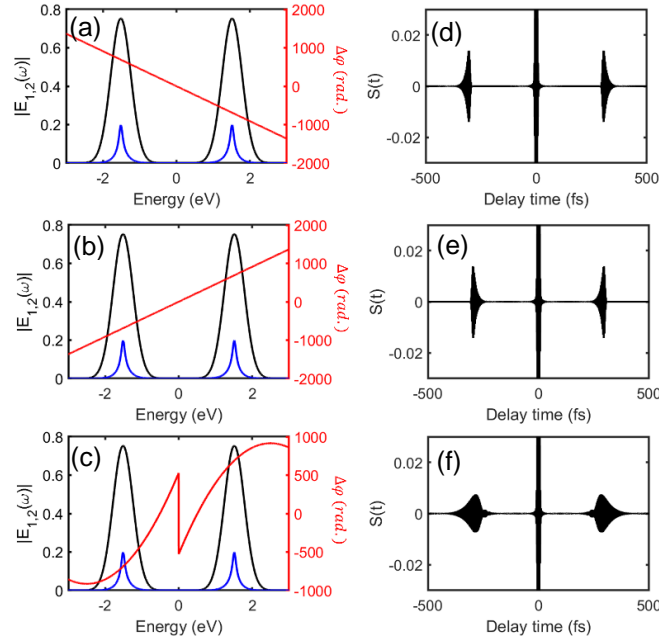


Figure 3.9 Field amplitude of $E_1(\omega)$ (black curves) and $E_2(\omega)$ (blue curves) as well as the phase of $\Delta\varphi$ (red curves) for (a) $\varphi_f = 0$ and $\Delta\varphi > 0$, (b) $\varphi_f = 0$ and $\Delta\varphi < 0$, (c) $\varphi_f = 100fs \cdot \omega^2$ and $\Delta\varphi < 0$. (d,e,f) Real valued Fourier transformation of the corresponding interferogram, $\mathcal{F}^{-1}\{S_s(\omega)\}$.

- (2) Oppositely, for $\varphi_f = 0$ and the length difference is positive $\Delta L = +900 \text{ nm}$ as shown in figure 3.9 (b), two side peaks in time domain still sit at $\tau_s = \pm 300fs$, while the exponential decay tail in the side peak is reversed and shows up shortly ahead of the peak position. In this case, the exponential tail is possibly overlapped with the central band when the delay time is not sufficiently large, and it also depends on the lifetime of the Lorentzian resonator as well as the pulse width.
- (3) On the base of the second case with $\Delta L = +900 \text{ nm}$, the third case introduces a quadratic phase of $\varphi_f = a(\omega - \omega_0)^2$ where $a = 100 \text{ fs}$ is the chirp parameter of the filter, as depicted in Figure 3.9(c). Correspondingly, two side peaks in the time domain as observed in panel (f) shows a stretched envelope in comparison to the time structure in panel (e). This broadened amount depends on the dispersion index of the filter material in the laser spectral range.

Now I simulate the experimental interferogram data recorded on the fast line camera by taking the first case. To mimic the reference mirror jittering, a time dependent arm length difference is additionally introduced (as illustrated in figure 3.10 (a)), $\Delta L(t) = A * \sin(2\pi f_j t)$ where $A=500 \text{ nm}$ and $f_j = 10 \text{ Hz}$ is the mirror vibration frequency. The time delay caused phase of the interferogram in equation (3.1) is in this case altered as a time dependent function, $\Delta\varphi(t) = \frac{\omega}{c_0} \cdot (\Delta L + \Delta L(t))$. The resulting signal in an integration time of 300 ms is shown in figure 3.10 (b), in which the spectral interference fringes regularly swings.

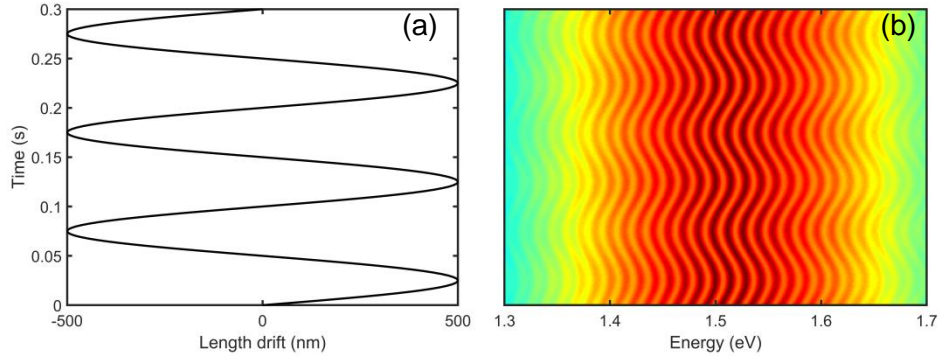


Figure 3.10 (a) Reference mirror jitter length in 0.3 s integration time and (b) the resulted spectral interference.

For such a data series, the first step is to eliminate the signal noise introduced by the setup system, literally to stretch the stripes in the image. The essential work is to find out the time delay in each interferogram and then normalize to the same point. Generally, there are methods to realize the delay between two interference fields. For the first method, the side peak position of the interferogram in time domain gives the time delay, τ_n . Taking τ_1 of the first spectral interferogram $S_{s1}(\omega)$ as a reference, one gets the delay time evolution of $\tau_d = \tau_n - \tau_1$. Therefore, this delay drift can be corrected by compensating a phase term of $e^{\pm i \cdot \omega_0 \tau_d}$ (ω_0 is the spectral central frequency) to the negative/positive component of $S_s(t)$, for instance, $s'(t) = S_s^+(t) \cdot e^{-i\omega_0 \tau_d} + S_s^0(t) + S_s^-(t) \cdot e^{i\omega_0 \tau_d}$, then the drift corrected interferogram spectrum is obtained from its inverse Fourier transformation: $S'_s(\omega) = \mathcal{F}^{-1}[s'(t)]$. On the other hand, according to the shift property of the Fourier transform, a shift in time domain corresponds to a linear phase of

$e^{i\tau\omega}$ in frequency domain, therefore the second method verifies the time delay from the slope of the linear spectral phase, for example $Arg(S^-(\omega))$, where $S^-(\omega) = \mathcal{F}^{-1}\{s^-(t)\}$. Correspondingly, the delay drift is corrected in the frequency domain as well, thus the compensated time structure in this case is $s'(t) = \mathcal{F}[S^+(\omega) \cdot e^{-i\omega\tau_d}] + s^0(t) + \mathcal{F}[S^+(\omega) \cdot e^{-i\omega\tau_d}]$.

In principle, both methods help correcting the reference arm jitter caused time delay drift in the interferogram signal, however precisely searching for the peak position is difficult for a broad band spectrum because the side component of $s^+(t)$ is no longer a sharp peak but a blunt band. Hence, the second approach is utilized to retrieve the time delay evolution as displayed in figure 3.11(a) which precisely overlaps with the set values. Then the corrected signal is obtained as displayed in panel (b) which shows straight stripes as expected.

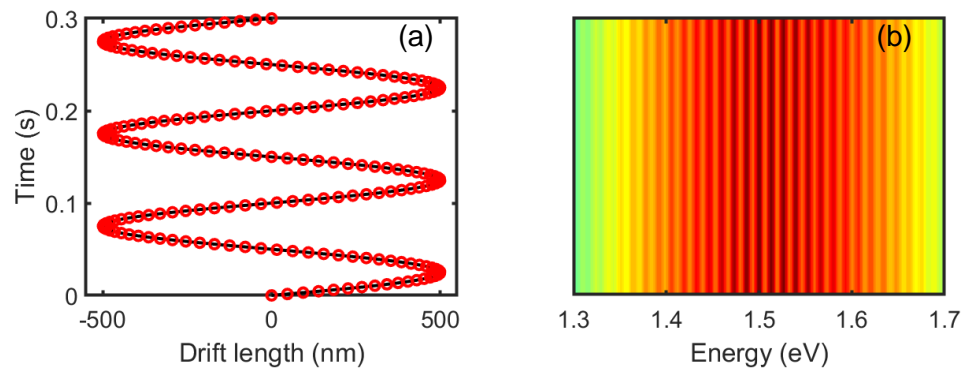


Figure 3.11. (a) Retrieved (black) and manually set (red) mirror jitter length, and (b) corrected spectral interferogram series.

At last, I will describe the Fourier-transform technique based on the simulation data. This technique will be eventually referred to as retrieving the near-field response function which will be discussed in detail in Chapter 5. As discussed in equation (3.8), the Fourier amplitude of an interferogram consists of three components. The essential idea of the Fourier-transform technique is to isolate the dc and ac peaks by filter. In this way, more relationships among variables in the formular are formed such that the near-field property is retrievable from solving equation set.

Figure 3.12 (a,b) display the simulated interferogram $S_s(\omega)$ and its Fourier amplitude $s(t)$.

Applying a rectangular window (red dashed lines in panel b) divides $s(t)$ data into three segments as formulated in equation (3.8). Then performing inverse Fourier transform algorithm to the DC peak $s^0(t)$ results in a DC spectrum:

$$S^0(\omega) = 1/16 \cdot |E_0(\omega)|^2 \left(|t_f|^4 + |\sigma(\omega)|^2 \right) \quad (3.9)$$

As illustrated in black curve in figure 3.12 (c), the DC spectrum shows a similar shape to the input spectrum. The AC spectrum transferred from the positive component $s^+(t)$ is given by:

$$S^+(\omega) = 1/16 \cdot |E_0(\omega)|^2 \cdot |t_f|^2 |\sigma(\omega)| e^{i(-\varphi_\sigma + \Delta\varphi)} \quad (3.10)$$

as plotted in red curve in panel c. It displays evident difference from the DC spectrum because of the influence of the Lorentzian response $\sigma(\omega)$.

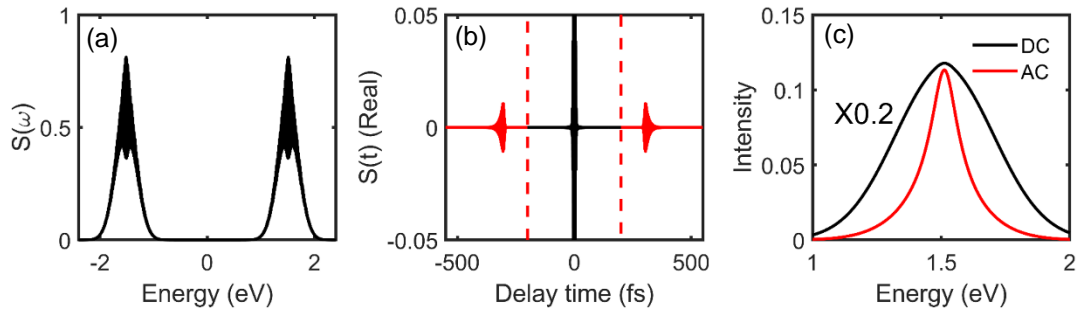


Figure 3.12 (a) Spectral interferogram with a fringe contrast of 20%. (b) Fourier transform of the interferogram in (a) with a DC contribution around $\tau = 0$ fs and an AC contribution around $\tau = \pm 300$ fs. (c) Inverse Fourier transforms of the DC (dashed black) and the positive AC (solid blue) component as isolated by the window in (b). (d) Retrieved amplitude (blue) and phase (red) of the sample response.

Combining the Equation (3.9) and (3.10), with setting the constant $t_f = 1$ for simplicity, the ratio between the AC and DC components gives a quadratic equation of the amplitude $|\sigma(\omega)|$:

$$\frac{|S^+(\omega)|}{|S^0(\omega)|} = \frac{|\sigma(\omega)|}{1 + |\sigma(\omega)|^2} \quad (3.11)$$

Solving the equation of $|\sigma(\omega)|^2 - |\sigma(\omega)| + \frac{|AC(\omega)^+|}{|DC(\omega)|} = 0$ gives two solutions: $|\sigma^+(\omega)| = \frac{1}{2f}$.

$(1 + \sqrt{1 - 4f^2})$ and $|\sigma^-(\omega)| = \frac{1}{2f} \cdot (1 - \sqrt{1 - 4f^2})$, with $f = \frac{|S^+(\omega)|}{|S^0(\omega)|}$. The laser spectrum, according to the equation (3.10), is given by $|E_0(\omega)|^2 = 16 \cdot |AC(\omega)^+|/|\sigma(\omega)|$. For two solutions of $|\sigma^{\pm}(\omega)|$, the spectral shape of $|E_0^c(\omega)|^2$ results in two possibilities as shown in figure 3.13. The negative solution $|\sigma^-(\omega)|$ generated spectral shape (in red dash curve) exactly coincidences with the assumed laser spectrum $|E_0(\omega)|^2$ (in black solid curve). Therefore, one concludes that the response function amplitude is determined by the negative solution in equation (3.11), $|\sigma(\omega)| = |\sigma^-(\omega)|$, as plotted in figure 3.13 (b) which also matches the simulated Lorentzian line shape.

Moreover, the phase structure of the AC component in equation (3.11) implies that:

$$\varphi_\sigma = \Delta\varphi - \arg(S^+(\omega)) \quad (3.12)$$

Figure 3.13 (c) shows the phase shape of $\arg(S^+(\omega))$, in which a large amount of linear component originating from phase $\Delta\varphi$ is contained. To deduce the influence of $\Delta\varphi$, the linear phase component is fitted by performing a first order polynomial fitting of $\arg(S^+(\omega))$, as plotted in red dashed line in panel (c). Based on such fitted phase, the response function phase φ_σ is retrieved according to equation (3.12) and is displayed in Figure 3.13 (d) which demonstrates a great agreement with the principal values and shows a π phase jump at the resonance frequency.

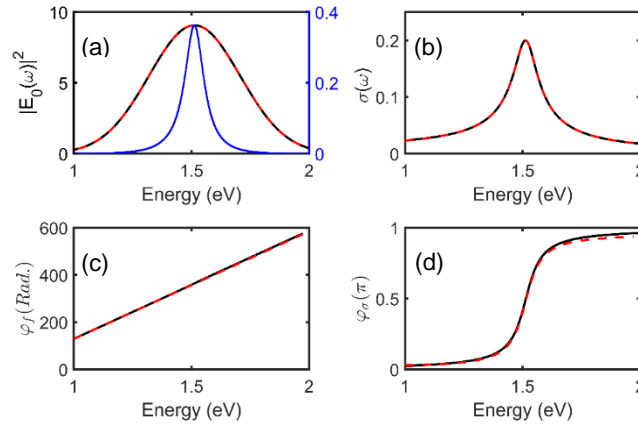


Figure 3.13 (a) Calculated input laser spectral shape as $|\sigma(\omega)|$ is taken as a negative solution of $\frac{1}{2f} \cdot (1 - \sqrt{1 - 4f^2})$ (red dashed curve) and a positive solution $\frac{1}{2f} \cdot (1 +$

$\sqrt{1 - 4f^2}$) (blue curve). The laser spectrum calculated from the negative solution $|\sigma^-(\omega)|$ has the same spectral shape as the assumed laser spectrum $|E_0(\omega)|^2$ (black curve). (b) Calculated (black curve) and simulated (red dashed curve) lineshape of $|\sigma(\omega)|$. (c) Spectral phase (black curve) of the side peak component, $\arg(S^+(\omega))$ and the fitted linear phase (red dashed curve). (d) The retrieved response function phase (red dashed curve) and the simulated Lorentzian phase φ_σ .

3.4.3 Experimental spectral data processing

For the measurement data as displayed in figure 3.5, a spectrum captured by the line camera is illustrated in figure 3.14 (a), where spectral fringes originate from the spectral interference between the sample arm field and the reference field. The interferogram in delay time domain in panel (b) evidently shows one central contribution (DC part) and two delay components (AC part), and the time delay is large enough such that two AC peaks can be isolated from the DC peak. As discussed in the simulation, such a time delay corresponds to a linear phase in frequency domain. The phase of the AC peak spectrum, namely the inverse Fourier transformation of the AC peak, in figure 3.11 (c) displays a prominent linear shape, therefore the slope of a linear fit to the AC spectral phase reveals the delay time τ of the interferogram. Moreover, this deduced delay time for every interferogram in the measured 60000 frames (in figure 3.6) is shown in figure 3.11 (d). It contains a fast modulation in a slow vibrating motion. The fast modulation is generated by tip vibration with an amplitude of about 30 nm. The wavy fringes in the camera 2D data are obviously caused by slow motion. Hence the fast tip modulation is eliminated by filtering the time delay signal in frequency domain (panel (e)), and the jitter length can be obtained from $c_0\Delta\tau$ where $\Delta\tau$ is the time delay variation referenced to the first interferogram.

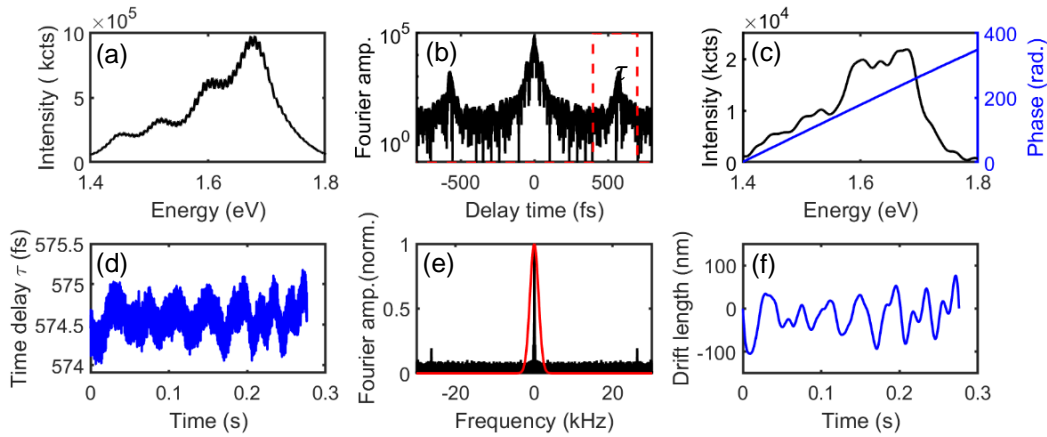


Figure 3.14. (a) A typical spectral interferogram in energy axis, from the measurement signal (figure 3.5). (b) Fourier transformation (black curves) of the interferogram in logarithm scale where two side peaks (AC component) located at time delay of $\pm\tau$ are distinguishable from the central peak (DC component). Red dashed lines isolate the positive AC peak. (c) Side peak spectrum (black peak), namely inverse Fourier transformation of the isolated positive peak in (b), and the spectral phase (blue line) in which the slope of the linear component quantifies the time delay τ of the interferogram. (d) Retrieved time delay values between two arms in the measurement data in figure 3.5. A slow vibration of τ originates from the reference mirror jitter and a fast modulation is generated by the tip vibration. (e) Fourier transformation (black curves) of the time delay evolution, in which the peaks at about ± 26.2 kHz represents the tip modulation frequency, and a narrow window (red curve) is used to filter out the slow variation in the time delay. (f) Delay drift of the measurement data in figure 3.5, obtained from the inverse Fourier transformation of the filtered component in (e).

According to the simulation, the retrieved delay drift is compensated in frequency domain, and the corrected interferogram data $S(\omega, t)$ is shown in figure 3.15 which displays straight interference fringes instead of the original oscillating stripes.

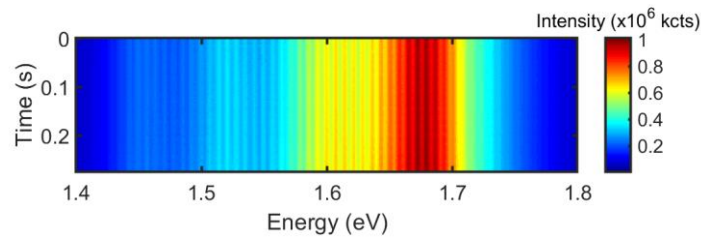


Figure 3.15 Measurement data after drift delay correction.

3.4.4 Demodulated spectral interferogram

At this point, demodulated spectral information can be achievable from the drift corrected signal $S(\omega, t)$. Beforehand, the tip vibration frequency is precisely identified.

For a specific frequency of ω , the time series $S_\omega(t)$ records the optical signal evolution which is modulated at the tip vibration frequency. To show the temporal modulation, the fast Fourier transform of each time series is performed. Figure 3.16(a) illustrates the Fourier amplitude of $S_{\omega_n}(t)$ as $\hbar\omega_n = 1.65 \text{ eV}$ and $\hbar\omega_n = 1.46 \text{ eV}$, respectively. Several peaks evidently appear at multiples of the fundamental tip modulation frequency, $f_0 = 27.756 \text{ kHz}$ with an accuracy of $df_t = \frac{f_{camera}}{N_{spec}} = 3.5 \text{ Hz}$. The signal to noise ratio of harmonic peaks decreases as the demodulation order increases.

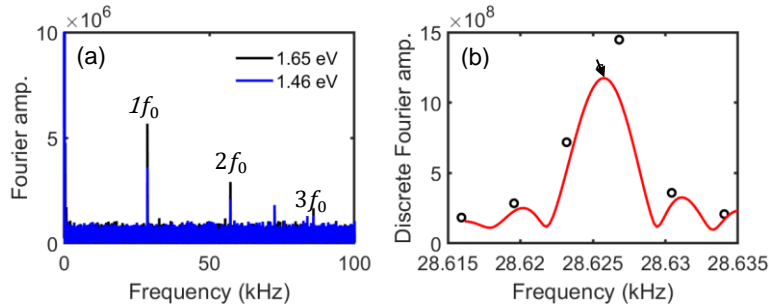


Figure 3.16 (a) The Fourier transforms of the signal shown in figure 3.15 along the time axis for specific energy axis point of $\hbar\omega_n = 1.65 \text{ eV}$ (black curve) and $\hbar\omega_n = 1.46 \text{ eV}$ (blue curve), showing peaks at the fundamental (peak marked with ' f_0 ') and harmonics of the tip modulation frequency. The unmarked peak between $2f_0$ and $3f_0$ originates from the utility frequency. (b) DFT function calculated over a section near the f_0 as plotted in red curve, together with the corresponding values of the FFT function as labeled with black circles.

Here, the obtained frequency f_0 may not be precise enough because the camera readout speed (210 kHz) is not a multiple of the tip frequency. Thus, a more accurate method seeking the tip modulation frequency is needed. Based on the preliminarily estimated f_0 ,

we take 100 evenly spaced frequency values f_i distributed around f_0 and compute the discrete Fourier transform (DFT) of the time series for each frequency f_i ,

$$s(f_i) = \sum S(t) \cdot e^{-i \cdot 2\pi f_i \cdot t} \quad (3.13)$$

Figure 3.16 (b) plots the integrated Fourier amplitude $\sum s_n(\omega_i)$ for each frequency ω_i in the subtle range. The finer grid calculation (red curve) leads to a higher first harmonic signal, because the peak of the DFT curve more precisely determines the tip frequency. Hence, the peak frequency f of the DTF curve is determined as the tip modulation frequency for the following data processing.

In the following, the interferograms demodulated at different order harmonics of the tip frequency are calculated. As discussed in Chapter 2, the time series $S_\omega(t)$ can be approximated by a Fourier series:

$$S_\omega(t) \approx \sum_{n=-\infty}^{\infty} c_{n,\omega} \cdot e^{i2\pi n f t} \quad (3.14)$$

with the complex Fourier coefficients:

$$c_{n,\omega} = \frac{1}{T} \int_{-T/2}^{T/2} S_\omega(t) \cdot e^{-i2\pi n f t} dt \quad (3.15)$$

Here, n is the demodulation order, and $T = 1/f$ is the modulation period with the tip modulation frequency f . In practice, we typically extract five coefficients $c_{n,\omega}$ with $n = 0, 1, 2, 3, 4$ and $c_{-n,\omega} = c_{n,\omega}^*$.

Plotted as a function of energy in Figure 3.17 (a), for $n=0$, the (real-valued) Fourier component $c_{0,\omega}$ represents the temporally averaged spectrum,

$$S_{0f}(\omega) = c_{0,\omega} = \langle S_\omega \rangle \quad (3.16)$$

The Fourier components $c_{n,\lambda}$ with $n > 0$ are complex-valued, and literally express the signal demodulated at n th order harmonics as denoted by $S_{nf}(\omega) = c_{n,\omega}$. Figure 3.17 (b) depicts the demodulated interferogram $S_{nf}(\omega)$ for $n = 1, 2, 3, 4$. Fringes in the demodulated signal $S_{nf}(\omega)$ originate from interference between the reference field and the background field scattered by the tip shaft as well as the near-field from the tip apex.

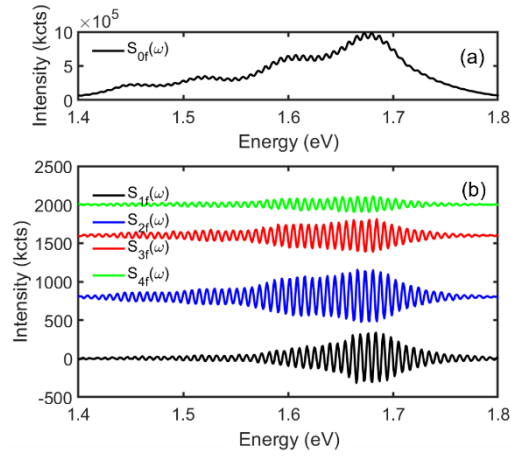


Figure 3.17 The spectral interferogram demodulated at (a) 0th order, and (b) 1st, 2nd, 3rd, 4th order harmonic of the tip modulation frequency, $c_{n,\omega}$, show strongly modulated spectrum.

At last, the demodulated spectra are obtained from the interferograms $S_{nf}(\omega)$. Figure 3.18 (a) illustrates the Fourier transform amplitude of signal $S_{2f}(\omega)$, and the blue dashed line labels the isolated positive side peak. Inverse Fourier transformation of the AC peak results in the positive spectrum $S_{2f}^+(\omega)$ where the interference spectral fringes are eliminated, (figure 3.18 (b)). Analogously, demodulated spectra $S_{nf}^+(\omega)$ for $n=1,3,4$ are retrieved as well, and $S_{2f}^+(\omega)$, $S_{3f}^+(\omega)$, $S_{4f}^+(\omega)$ spectra closely resemble each other, while the spectral shape of $S_{1f}^+(\omega)$ clearly deviates from others. In agreement with the in chapter 2, this leads to conclude that the higher-order demodulated spectra reliably reflect near-field spectra, while spectral interference of background and reference fields give rise to spectral variations in the $S_{1f}^+(\omega)$ signal.

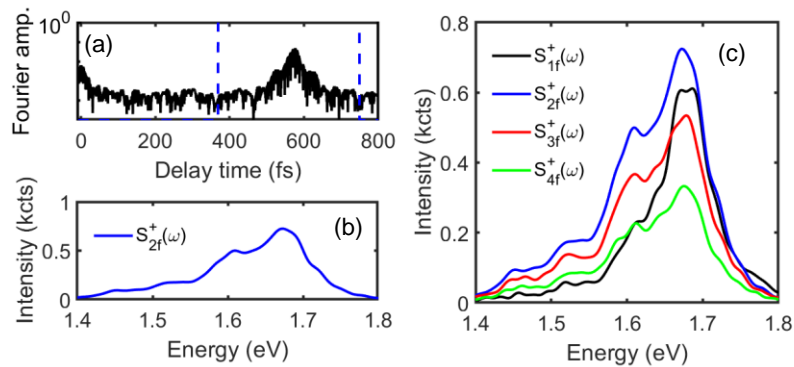


Figure 3.18 (a) The Fourier transform of the spectral interferogram signal $S_{2f}(\omega)$ in logarithm shows AC peak (marked with blue dashed line). (b) The side peak in (a) is isolated, then applying the inverse Fourier transform yields unmodulated spectra $S_{2f}^+(\omega)$.

4 Spatial and spectral mode mapping of a dielectric nanodot

4.1 Sample preparation

Sb_2S_3 has recently sparked interest as a promising sensitizer for hybrid solar cells.¹⁶³ It has a high absorption coefficient ($1.8 \times 10^5 \text{ cm}^{-1}$ at 450 nm for amorphous thin films) and a bandgap of 1.7 eV, consists of abundant materials and is assumed to be of reduced toxicity.¹⁶⁴ Here, we investigate Sb_2S_3 nanoparticles on a flat, 140-nm-thick film of crystalline Sb_2S_3 . The nanoparticles are created by EBL⁶⁵ on top of the flat film in a regular order.

Sample preparation is inspired by a metal-butyldithiocarbamic acid (BDCA)¹⁶⁵-based molecular precursor solution that we adopted for direct patterning. BDCA is nontoxic, cheap, and thermally degradable and can be easily synthesized by the reaction of carbon disulfide and 1-butylamine. The ethanol solution of BDCA can be directly applied to dissolve various types of hydroxides and metal oxides, such as Sb_2O_3 forming chalcogenide precursor solutions. This Sb_2S_3 -complex solution diluted with ethanol (ratio 2 to 1)¹⁶⁶ was deposited on TiO_2 substrate by spin-coating at a speed of 8000 rpm for 30 s. After spin-coating, the substrate was baked at 140 °C for 1 min, which resulted in the formation of a 180-nm thick orange-red amorphous Sb_2S_3 thin film. The obtained substrates were transferred into a glove box to anneal at 300 °C for 30 min, upon high-temperature annealing, the thermal decomposition of metal–organic molecular precursors will generate chalcogenide materials, forming a 140-nm thick, compact, crystalline Sb_2S_3 film. On top of this dense Sb_2S_3 film, a second, 100-nm thick Sb_2S_3 film was deposited as a precursor for the nanostructure fabrication, by spin-coating an Sb_2S_3 -complex solution diluted with ethanol. We then directly transferred the obtained substrate into the electron beam lithography (EBL) system (Elphy nanolithography based on Zeiss Neon 40EsB 30 keV scanning electron microscopy) for electron beam patterning (EBP) with a typical dose of $36.000 \mu\text{C}/\text{cm}^2$ at 20 keV. After the EBL process, the substrates were annealed at 300 °C for 30 min in a glove box. At last, the patterned Sb_2S_3 nanoparticle array was developed with acetone rinse.

Figure 4.1 (a) shows a scanning electron microscope (SEM) image of the nanoparticles array. The spacing between particles ($2\ \mu\text{m}$ in Figure 4.1) is chosen sufficiently large to avoid dipolar couplings between adjacent nanoparticles such that each nanodot may be considered as an isolated nanoparticle. They are typically dome-shaped, with a round or slightly elliptical cross section of $\sim 350\ \text{nm}$ diameter and a height of $\sim 150\ \text{nm}$. As indicated in Figure 4.1 (b), a higher resolution image of an individual nanoparticle reveals a slightly elliptical shape and a somewhat rough surface. The center of the particle seems to have collapsed to some extent after the annealing processes following EBL. These features (ellipticity, surface roughness, and indentation) vary slightly from one nanoparticle to the next.

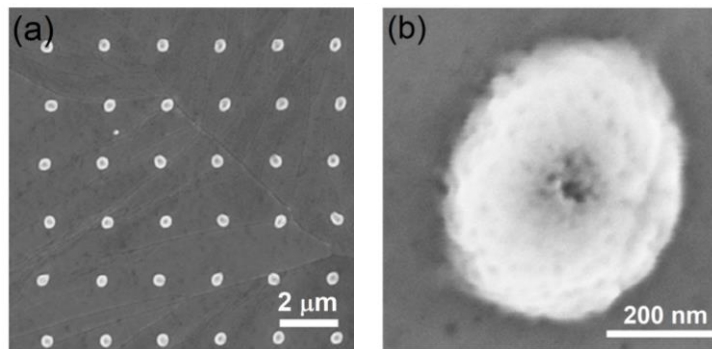


Figure. 4.1 Scanning electron microscopy (SEM) images of the sample. (a) Sb_2S_3 nanodots are created on a flat, compact Sb_2S_3 film by electron beam lithography (EBL). The nanodots are regularly spaced by $2\ \mu\text{m}$, their shape varies slightly. (b) The SEM image of an individual nanodot shows a slight ellipticity and a dark shadow in the center, where the material has collapsed after EBL and annealing.

Our samples are annealed at $300\ ^\circ\text{C}$ such that crystalline thin films and nanostructures are formed. This procedure results in a reduced above-gap absorption coefficient ($8 \times 10^4\ \text{cm}^{-1}$ at $450\ \text{nm}$),⁶⁴ and appreciable absorption just below the band edge ($2.5 \times 10^4\ \text{cm}^{-1}$ at $700\ \text{nm}$). In the spectral region investigated here ($700\ \text{nm}$ and $900\ \text{nm}$), Sb_2S_3 has relatively low losses (absorption $< 10^4\ \text{cm}^{-1}$ at $800\ \text{nm}$) and a high index of refraction with a positive real part varying from 3.2 at $700\ \text{nm}$ to 2.9 at $900\ \text{nm}$ as demonstrated in figure 4.2, which means it interacts with the light from the

Titanium:Sapphire laser as a dielectric.

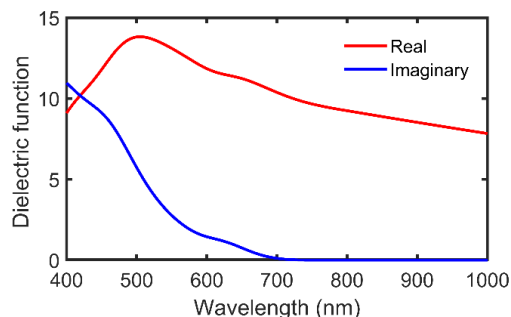


Figure 4.2 Dielectric function of Sb_2S_3 film.

Subband absorption observed in crystalline Sb_2S_3 suggests the existence of trap states, for example due to defects in the crystalline structure.⁶⁴ Such trap states could be used to increase the total light conversion efficiency of a solar cell, particularly if the interaction length of below-bandgap light with the material is increased. Here we cover the flat crystalline Sb_2S_3 film with Sb_2S_3 nanoparticles, aiming at a cylindrical structure that should guide the incident light into the underlying thin film.

4.2 Near-field imaging

Before recording BISNOM spectra, we perform preparatory experiments to validate the near-field contrast and spatial resolution of the optical signals in our near-field microscope.

4.2.1 Near-field contrast

We use a quasi-monochromatic spectrum for excitation, created by inserting a 40-nm bandwidth interferometric filter centered at a wavelength of 900 nm in front of the BS, and the APD and lock-in amplifier for detection. The demodulated signals S_{1f} , S_{2f} , S_{3f} and S_{4f} are generated by the lock-in amplifier and are recorded during the measurement. Figure 4.3 (a) shows approach curves recorded above a flat Sb_2S_3 film, i. e., the demodulated signals as a function of tip-sample distance. The approach is stopped when the tuning fork oscillation amplitude is reduced by 2.5% (see inset of Figure 4.3 (a)). This

position, which corresponds to a minimum tip-sample distance of about 4 nm, is later taken as the set point for lateral sSNOM scans. The blue, green and red curves in Figure 4.3 show the optical signals S_{1f} , S_{2f} and S_{4f} , respectively, when the sample is retracted from the tip. To retain clarity in Figure 4.3 (a), S_{3f} is not shown, as its shape is very similar to that of S_{2f} . As the tip is retracted, the near field decays quickly. This is reflected by all three curves shown in Figure 4.3 (a), where the strong peaks at the minimum tip-sample distance of 4 nm decrease to their half maximum value within increasing the tip-sample distance by 1 nm. Compared to the near field, the background field's dependence on the tip-sample distance is weaker. As a result, the first-order demodulated signal, S_{1f} , which mainly probes background scattering from tip shaft, remains at a rather high level and fluctuates strongly also for large tip-sample distances. Fluctuations arise from finite mechanical instabilities and/or laser noise. The higher demodulation orders, however, measure an interference between the near-field signal and the background. Here, a measurable signal is only seen for tip-sample distance of <10 nm. The signal amplitude in contact decreases when going from 2f to 4f due to the demodulation of the signal recorded with finite tapping amplitudes.⁵⁸

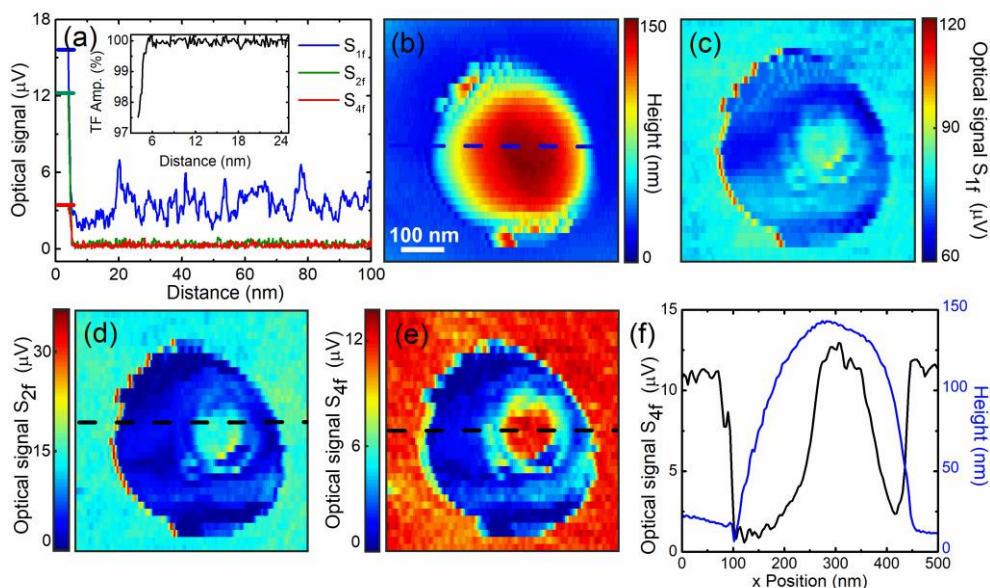


Figure 4.3 Quasi-monochromatic SNOM measurements of an individual nanoparticle

using a 40-nm bandwidth laser spectrum centered at 900 nm for excitation and the APD and lock-in amplifier for detection. (a) Optical signal demodulated at the first (blue curve), second (green curve), and fourth harmonic (red curve) of the tip modulation frequency as a function of tip-sample distance. The higher order demodulated signals demonstrate improved near-field contrast. The inset shows the simultaneously recorded tuning fork amplitude. (b) Topographical map, and (c)-(e) maps of the optical signals S_{1f} , S_{2f} and S_{4f} , respectively. All maps show a ring-shaped intensity distribution. (f) Cross cuts through the topographical map (blue curve) and the S_{4f} signal (black curve) along dashed lines in Figures. (b) and (e).

To further evaluate the optical image capabilities of the near-field microscope we then scanned a single Sb_2S_3 nanodot with the quasi-monochromatic measurement method, while the tip-sample distance was kept constant at ~ 4 nm. The height of the sample and the demodulated signals S_{1f} to S_{4f} were recorded over a $1 \mu\text{m}$ by $1 \mu\text{m}$ large area. The sample was scanned line-wise in the x -direction with a step size of 4 nm and with a step-size of 16 nm between the lines, i. e., in y -direction. The topographic image displayed in Figure 4.3 (b) shows that this nanodot was almost circular, with lengths of 360 nm and 380 nm of the short and the long axis of an ellipse, respectively, and with a height of about 150 nm. The simultaneously recorded maps of the signals S_{1f} , S_{2f} and S_{4f} are displayed in Figure 4.3 (c), (d), and (e), respectively. They all display a clear optical signal drop in the shape of a ring over the particle. In the following we investigate several of the observed features one by one.

The near-field images of the nanodot in Figure 4.3 show a rather smooth surface and sharp signal change at the edge of the nanoparticle. The maps of the S_{1f} and S_{2f} signals display some variation across the surrounding Sb_2S_3 film, which may be caused by residual background interference. The S_{1f} and S_{2f} maps both show a strong and sharp signal increase at the left-hand edge of the nanoparticle, which is probably caused by the grazing incidence of the illuminating laser light. The sharp spike in the S_{2f} map (the red border on the left side of the particle in Figure 4.3 (d)) gives an upper limit for the spatial resolution of the optical images of 10 nm (a cut through Figure 4.3 (d) is shown in the

Figure 4.4).

The best near-field contrast is reached with the S_{4f} signal (Figure 4.3 (e)). The optical signal measured across the particle is reduced in the ring-shaped area with respect to the signal measured on the film by roughly 90%. This difference can be understood as follows. While the tip is within a small distance to the flat film, the tip dipole, which is excited by the laser light incident on the tip, induces a polarization in the Sb_2S_3 film. The incident light and light scattered from the film couple to the polarizability component of the tip dipole that is oriented along the polarization direction of the incident laser field. The laser is polarized perpendicular to the tip axis to avoid strong resonance excitation of the longitudinal tip polarizability. The y-polarized tip dipole induces an image in the sample and electric field re-emitted by the film enhanced the tip dipole, and as a result the field scattered by the tip that reaches the detector is enhanced. In the flat film region, the near-field contrast thus results from the coupling of the tip and image dipoles as introduced by Knoll and Keilmann as the coupling of a probe dipole and an image dipole.¹⁶⁷ The strong signal in the area surrounding the nanoparticle corresponds to a large LDOS, through the continuum of evanescent waves the tip point dipole can couple to.^{168, 169} As the tip reaches the edge of the particle and is lifted off the flat film, it does no longer couple to an extended film, but to a nanoparticle of finite size, or, more specifically, to nanoparticles arranged in a square array. The environment of the tip dipole can now better be described by a square lattice of pillars surrounded by air, with a refractive index ratio of ≈ 3 , giving rise to Bloch waves as solution to the wave equation rather than a continuum of modes.¹⁷⁰ This considerably reduces the LDOS, which is seen by the signal decrease at the rim of the nanodots.

From this low-signal region near the rim inside the nanodot, the near-field signal again rises steadily towards the center of the nanodot. The over-all symmetry is roughly radial. To show this more clearly, cuts through the topographic image and through the S_{4f} map (along the dashed lines in Figures 4.3(b) and (e)) are plotted together in Figure 4.3 (f). The topography contour (blue curve) is a smooth cone, with its maximum leaning somewhat to the right. The S_{4f} signal drops abruptly as the tip reaches the particle and has a minimum close to the edge. Scanning towards the center of the particle the signal

rises again until it reaches a maximum at the center of the particle, where the signal strength is slightly higher than measured on the flat film. In contrast to plasmonic nanoparticles, where the electric fields usually concentrate at the surface, the field penetrates dielectric nanoparticles, and the electric field maxima are usually formed within the particles.⁵⁹ We thus interpret the central feature as the spatial extent of the superposition of optical modes excited by the laser light. The dome-like shape of the observed mode is reminiscent of fundamental fiber-optical modes and suggests that such a waveguide mode is excited in the Sb_2S_3 nanoparticle. As the nanodot and the film are fabricated from the same material and are annealed after EBL, near perfect index matching prevents back-reflection. We expect that the nanodot efficiently guides and couples the incident light to the underlying film, where the light finally dissipates.

4.2.2 Spatial resolution

In order to determine the spatial resolution of our sSNOM, we measure the size of the smallest features in the measured near-field maps. A suitable example can be found in the monochromatic sSNOM measurements shown in Figure 4.3, where at the left side of the nanoparticle a sharp spike appears. The S_{2f} signal map is redrawn in Figure 4.4 (a). While the near-field probe scans from the left to the right, it comes in close contact with the side of the nanodot before the tip is retracted. This causes the sharp signal increase seen as the red border around the particle on the left side. Figure 4.4 (b) shows a crosscut along the dashed line in Figure 4.4 (a). The pixel-size of such a line scan is 4 nm. One can clearly see the sharp spike that arises as the tip reaches the edge of the nanoparticle, and a fast decrease of the S_{2f} signal to the low level inside the particle. Both, the width of the peak and the distance over which the signal drops, are ~ 10 nm. We thus can take 10 nm as the upper limit for the optical resolution in our SNOM.

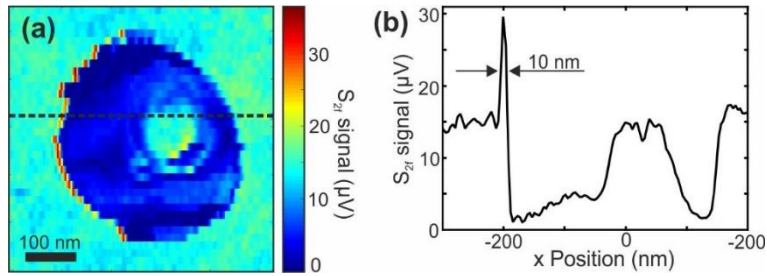


Figure 4.4 Spatial resolution of the optical signal in sSNOM. (a) Map of the optical signal S_{2f} of a single Sb_2S_3 nanodot with slightly elliptic shape of approximately 360 nm by 380 nm, and of 150 nm height. For the measurement, a quasi-monochromatic laser spectrum with 40 nm bandwidth centred at 900 nm was used. (b) Cut along the dashed line in (a). A sharp spike is seen, followed by a drop of the signal to a lower level inside the particle. Both the width of the peak and the distance over which the signal drop occurs are 10 nm.

4.2.3 Influence of surface roughness

In order to demonstrate the influence of shape and surface structure on the sSNOM images, we selected a Sb_2S_3 nanodot with a relatively rough surface and recorded near-field maps using the APD and lock-in amplifier. In these measurements, we turn our attention to hotspots of high electric field intensity that are supported by nanoscopic features, like cracks and other surface defects.^{171, 172} The spatial extent of these hotspots is usually less than the spatial resolution in SNOM, such that their apparent size is resolution-limited. The recorded images of the selected nanodot are presented in Figure 4.5.

The topographic image (Figure 4.5 (a)) shows an almost circular nanodot of approximately 380 nm diameter and 150 nm height. With the height information provided by the atomic force microscope the surface seems smooth, with the remarkable exception in the lower right area. The fast modulation of the height information as the tip moves from left to right shows that the height change was rather rapid, such that the height control started oscillating. Possibly the nanodot was chipped on this side. The optical

signal demodulated with the fundamental tip modulation frequency, S_{1f} (Figure 4.5 (b)) reflects this height control oscillation by interference fringes that are visible in the same area, but the higher order demodulated signal maps S_{2f} , S_{3f} , and S_{4f} , shown in Figures 4.5 (c), (d), and (e), respectively, do not show any modulation in this area. All optical signal maps do, however, show a strongly modulated signal in the central area of the nanodot, which may indicate localized electric fields due to surface roughness on a scale below the resolution limit of the AFM image. Figure 4.5 (f) compares the topographical information (blue curve) and the S_{4f} signal (black curve) along a crosscut indicated by the dashed lines in Figure 4.5 (a) and (e), respectively. While the topology appears smooth, the S_{4f} signal is strongly structured, and indicates the mentioned hotspots on the nanodot surface. The size of the features reaches down to 20 nm, which agrees with the earlier estimation of the optical resolution in our SNOM.

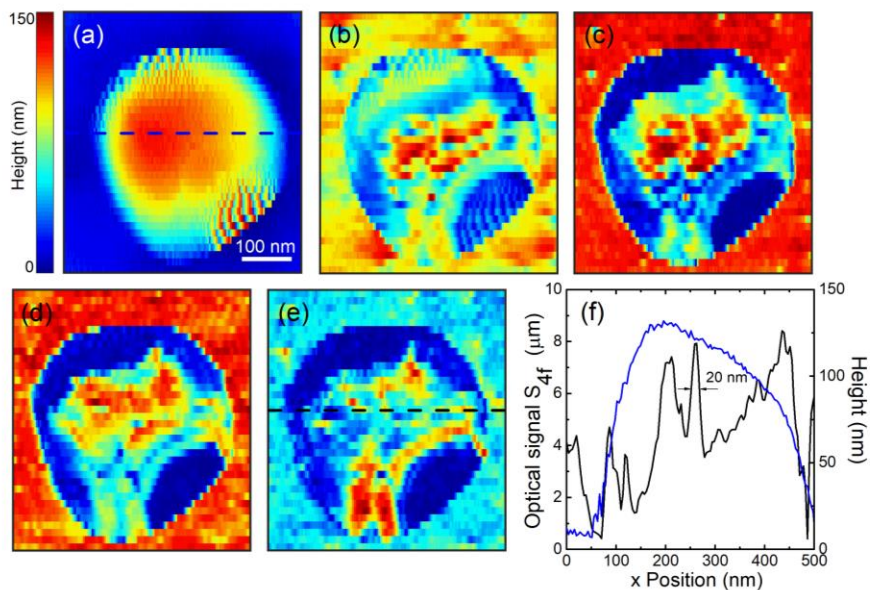


Figure 4.5 Near-field maps of an Sb_2S_3 nanodot. (a) The topographic image shows a slightly elliptical nanodot of approximately 320 nm by 380 nm, and of 150 nm height. With the height information provided by the atomic force microscope the surface seems smooth. (b)-(e) Maps of the optical signals recorded by demodulating at the first to fourth harmonic of the tip modulation frequency. (f) Cuts through the topographic map (blue

curve) and the S_{4f} signal (black curve), along the dashed lines in Figs. (a) and (e), respectively. While the topology appears smooth, the S_{4f} signal is stronger structured and thereby reveals hotspots on the nanodot surface. The size of the features reaches down to 20 nm.

In essence, the mode structure that was so clearly visible in many of the investigated nanodots is completely obscured by the smaller features observed here. In this example, the surface is strongly structured on a nanometer scale and thereby supports hotspots, which constitute the dominant features in the SNOM maps. In the less structured nanodots, we expect to measure a convolution of eigenmodes and surface features. The observed deviations of the measured SNOM maps from projected LDOS calculations can be seen as a result of such a convolution.

4.2.4 Calculation of eigen modes in Sb_2S_3 nanodot

In order to explain the measured spatial function of the waveguide modes, shown in Figure 4.3, we calculate the projected local optical density of states (LDOS). In the spectral region covered by the laser in this work, the nanodot material shows negligible absorption and very weak dispersion. Under these conditions the nanodot supports eigenmodes, which are very similar to the well-known modes of an optical fiber. Here we describe the calculations used to derive the projected LDOS, which then is compared to the measured near-field maps.

We assume that the LDOS in the nanodot region is mainly given as a sum over these bound modes with eigenvectors $\vec{e}_m(\vec{r})$ and eigenfrequencies ω_m . Each of these modes is characterized by a finite damping rate γ_m that describes the temporal decay of the electromagnetic field emitted by this mode after impulse excitation. In the limit of sufficiently weak damping, the LDOS may be phenomenologically written as

$$\rho(\vec{r}, \omega) = \sum_m |\vec{e}_m(\vec{r}, \omega)|^2 \delta(\omega - \omega_m) \quad (4.1)$$

Here $\delta(\omega - \omega_m) = -\frac{2i\omega'_m}{\pi(\omega_m - \omega^2 - 2\gamma\omega\gamma_m)}$ with $\omega'_m = \sqrt{\omega_m^2 - \gamma_m^2}$ is a generalized Dirac delta function. Its integral along the frequency axis gives unity. Quite generally, the damping

can be induced by the finite lifetime of the mode m , $T1_m$, and possible pure dephasing processes with pure dephasing time $T2_m$ resulting from stochastic fluctuations of the environment. Phenomenologically, the damping rate can then be taken as $\gamma_m = (2T1_m)^{-1} + (T2_m)^{-1}$ and the mode can be characterized by a complex resonance frequency $\tilde{\omega}_m = \omega_m - i\gamma_m$. The contribution of unbound radiation modes is neglected since their overlap with the nanodot core is small. For the perfect cylindrical waveguide considered here, for each bound mode a continuum of modes that are propagating along the fiber axis exists and the LDOS is spectrally flat.

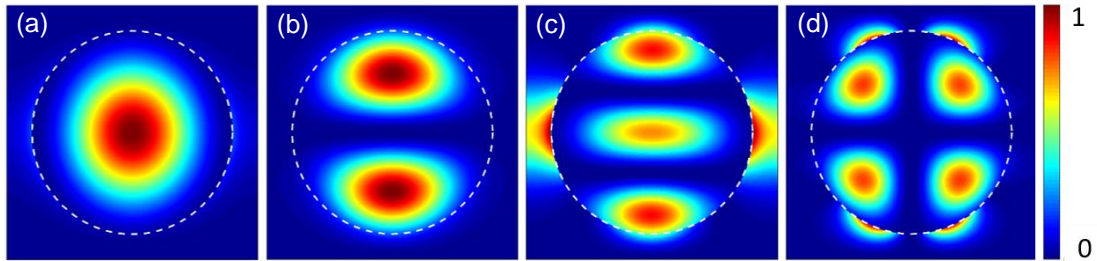


Figure 4.6 (a)-(d) Solutions of the modes identified in FDTD simulations for a cylindrical structure of 200 nm diameter and 75 nm height, capped with a semi-ellipse to a total height of 150 nm and placed on top of a 100-nm thick film, both with refractive index of 3.04. The circumference is outlined by the broken white circles. The modes profiles are very similar to analytical calculations for a cylindrical waveguide.

In order to retrieve the eigenmodes, we first performed FDTD simulations of a Sb_2S_3 nanodot. We modelled the structure as a cylinder with 200 nm radius and 75 nm height, capped with a semi-ellipse on top. The total height was 150 nm, and the structure was placed on a 100-nm thick film. For both the film and the structure we applied the experimentally measured refractive index function of Sb_2S_3 , which varies from 3.2 at 700 nm to 2.9 at 900 nm. The solution for the modes identified by the FDTD solver in the structure, in the xy -plane parallel to the surface of the film, are shown in Figure 4.6. They are very similar to analytical solutions for an infinitely long, cylindrical waveguide, which are well known, for example, for optical fibers (shown in Figure 4.7). For the sake of clarity in the following considerations of the LDOS, we continue with the analytical solutions of the cylindrical waveguide.

To calculate the eigenmodes of the Sb_2S_3 nanodot, we calculate the solutions of the vector Helmholtz equation for a weakly guiding, cylindrical waveguide, as introduced in Chapter 2. Taking a cylindrical structure with radius $a = 200 \text{ nm}$, with the refractive index of Sb_2S_3 and surrounded by air. We find that over the wavelength range covered in our experiment, such a structure supports four guided modes, the LP_{01} , LP_{11} , LP_{02} and LP_{21} modes. Here, the first index, m , designates the angular momentum, i. e., the number of azimuthal nodes divided by 2, and the second index, p , gives the number of nodes in the radial coordinate r , including the node at $r \rightarrow \infty$. The cutoff wavelength for the highest order of these modes, the LP_{21} mode, is expected to lie close to the long-wavelength limit of the used laser spectrum. The intensity profiles of these four modes, calculated for a wavelength $\lambda = 800 \text{ nm}$ and $n_{\text{Sb}_2\text{S}_3}(\lambda = 800 \text{ nm}) = 3.04$, are plotted in Figure 4.7. Note that the modes with angular momentum $m=1$ and $m=2$ are degenerate, such that the superposition and hence the LDOS is always rotationally symmetric (Figure 4.7 (a)). The waveguide modes are furthermore polarization degenerate and support electric field vectors in x - and y -direction.

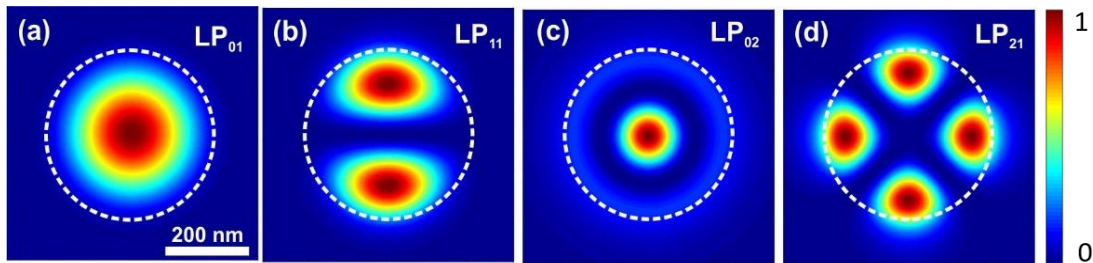


Figure 4.7 Calculated mode intensity profiles for a Sb_2S_3 cylindrical waveguide with radius 200 nm. The waveguide boundary is outlined by the broken white circle. Such a structure surrounded by air supports (a) the LP_{01} , (b) the LP_{11} , (c) the LP_{02} , and (d) the LP_{21} mode. The LP_{11} and LP_{21} modes are degenerate: in addition to the profiles shown there exist profiles that are rotated such that the position of nodes and antinodes is switched. (e) The superposition of these four modes, including the degenerate solutions, represents the LDOS and is rotationally symmetric.

The sum over the eigenmodes in Equation 4.1 is performed over the quantum numbers m and p of the bound fiber modes, as well as over the propagation constant $\beta_{m,p}(\omega)$, since, for every frequency ω in our spectral range and every bound mode (m, p) a wave exists that propagates along the fiber core with constant $\beta_{m,p}(\omega)$.

The LDOS for a cylindrical waveguide of 200 nm radius is plotted in Figure 4.8 (a). In this picture, the corresponding eigenvectors are two-fold polarization degenerate, for light field polarization along the x and the y axis, while the z -axis is the direction of propagation of the guided waves. An SNOM measurement carried out by scanning a point dipole \vec{p} oriented along \hat{u} across a structure with localized modes probes the projected LDOS,

$$p_u(\vec{r}, \omega) = \frac{2\omega}{\pi c^2} \text{Im}[\hat{u} \cdot \vec{G}(\vec{r}, \vec{r}, \omega) \cdot \hat{u}] \quad (4.2)$$

where, for weakly dissipative systems, Green's function can be written as

$$\vec{G}(\vec{r}, \vec{r}, \omega) \approx c^2 \sum_m (\vec{e}_m^*(\vec{r}') \otimes \vec{e}_m(\vec{r})) / (\omega_m^2 - \omega^2 - 2i\omega\gamma_m) \quad (4.3)$$

In principle, if a tip closely representing a point dipole was scanned across a flat surface with such a waveguide mode profile (such as the flat top of a pillar of Sb_2S_3 surrounded by air), the resulting SNOM map should be an image of the calculated LDOS shown in Figure 4.8 (a). In our experiment, however, the surface of the nanodot is not flat, but it is more truthfully described by a flattened half-ellipse with circular base of 200 nm radius and a shorter height of 140 nm. When scanning a point dipole across the nanodot, the point dipole projection onto its surface changes continuously. Figure 4.8 (b) shows in a sketch how the projection onto the surface (the red arrow) increases as an x -oriented tip dipole is moved along the central x -axis from the rim of the particle to its center. When scanning an x -oriented dipole along the central y -axis, however, the projection onto the surface does not change. In total, the projected LDOS then resembles the LDOS shown in Figure 4.8 (a), but it is cropped at the left and right side (see Figure 4.8 (c)). Analogously, when scanning a y -oriented dipole across the nanodot, the projected LDOS appears rotated by 90° (Figure 4.6 (d)). In contrast, a z -oriented tip dipole creates the largest projection close to the particle rim, resulting in the image shown in Figure 4.6 (e).

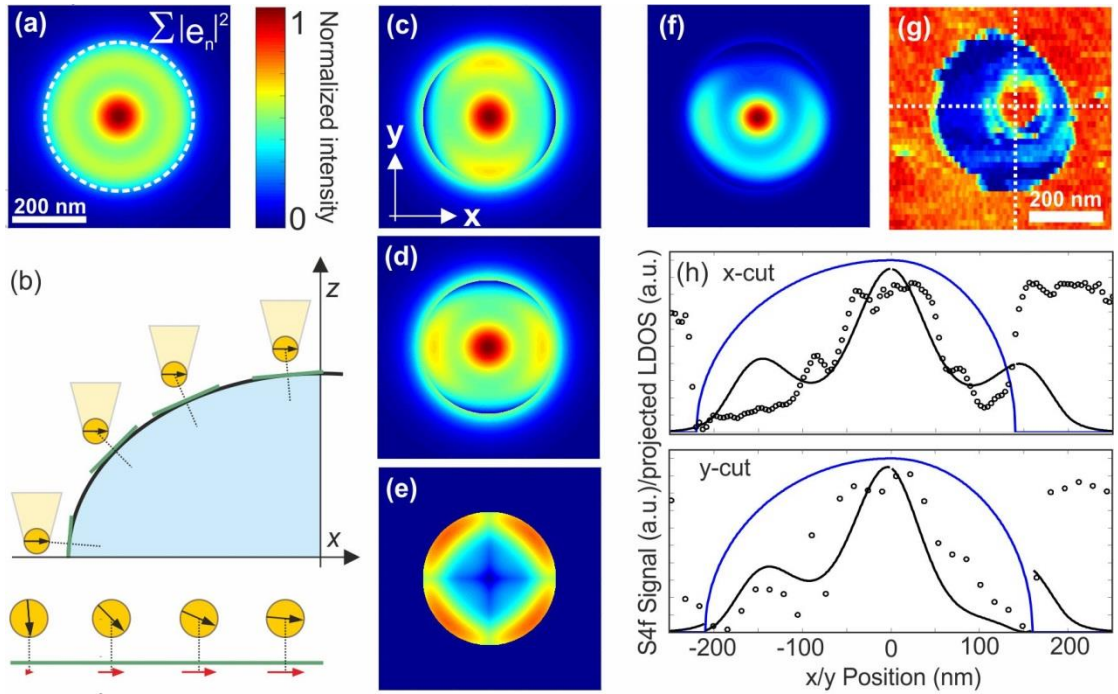


Figure 4.8 (a) Local density of states in a Sb_2S_3 -waveguide with circular cross section of 200-nm radius. (b) An x -oriented tip dipole is moved along the x -axis from the left rim to the center over the surface of the elliptical nanodot. Below is shown how the dipole orientation changes relative to the surface, and the red arrows at the bottom indicate the projection on the surface. (c) The projected LDOS as probed with an x -oriented tip dipole is cropped at the left and right rim, corresponding to the small projection of the tip-dipole onto the surface at these edges. (d) Using a y -oriented tip dipole results in a 90° -rotated image, and (e) a z -oriented dipole in particular probes the edge of the rim. (f) shows the asymmetric SNOM map calculated for a tip dipole $\vec{p} = (0.3, 1, 0.2)$ and (g) for comparison the measured S_{4f} map (same as Figure 3(e)). The main maximum as well as the asymmetric side lobes on the left and lower right and the near-zero signal regions at the top and bottom are well recreated. (h) A horizontal and vertical cut (upper and lower graph, respectively), of the measured SNOM map (black circles) together with calculated SNOM signals (black curve), calculated for the nanodot curvature shown by the blue curves.

In order to account for the curved surface, we here consider a modified projected LDOS, which we describe in the following. We assume a fixed dipole $\vec{p} = |\vec{p}| \cdot \hat{p}$ as excited by the laser focus. For each position (x, y) of the tip during a scan, the z-coordinate is retrieved as the height of the Sb_2S_3 nanodot surface:

$$z^2 = \begin{cases} \frac{H^2}{R^2}(R^2 - x^2 - y^2) & x^2 + y^2 \leq R^2 \\ 0 & x^2 + y^2 > R^2 \end{cases} \quad (4.4)$$

With $R=200$ nm the radius and $H=140$ nm the height at the center of the nanoparticle.

At every position (x, y) this yields the height $z(x, y)$ and from the derivation of Equation (4.4) the surface normal \hat{n} . The projection onto the surface is:

$$\vec{u}' = \hat{p} - \hat{n}(\hat{n} \cdot \hat{p}) \quad (4.5)$$

This modified projected LDOS is calculated by applying Equations (4.2) and (4.3), and it defines the field enhancement at the tip position and hence the induced dipole moment \vec{p}' of the tip.

In our experiment, the light was incident from a direction in the x - z -plane, with an angle of $\sim 20^\circ$ to the negative x axis and $\sim 70^\circ$ to the z -axis, with the field polarization along the y -axis. However, as the tips are etched and then glued onto the tuning fork manually, their orientation relative to the sample is with some error margin ($\sim 10^\circ$). Thus, an excitation of the z -oriented as well as the x -oriented tip dipoles can hardly be avoided due to uncertainties in the alignment of the tips, and an excitation of the three components on the diagonal of the polarizability tensor was considered. Considering the experimental configuration, we find that the tip dipole can be described well with $\vec{p}_{tip} = (0.3, 1, 0.2)$. Finally, the radiation of the tip dipole, locally enhanced by the coupling to the waveguide modes into the far field (i. e., the detector, located at position \vec{R}_{det} in the direction of the incident light) is calculated to yield the simulated SNOM map, shown in Figure 4.8 (f). The SNOM map displays a distinct radial asymmetry, which is likely to arise from the particular orientation of the tip dipole. The simulation using the projection of the tip dipole on an elliptical surface explains in particular the rather narrow central maximum in the SNOM map, as well as the side lobes to the left and lower right and the near-zero signal

strength at the upper and lower rim (compare S_{4f} map in Figure 4.8 (g)). Figure 4.8 (h) compares the simulated (black curves) and measured S_{4f} signals (black circles) along a horizontal and a vertical cut (upper and lower graph, respectively). These cuts have been calculated for the LDOS shown in Figure 4.8 (a), but for differently curved surfaces (indicated by the blue curves), in order to account for the slightly asymmetric shape of the nanoparticle. One can in particular see that neither simulated nor measured values reach zero at the left and right rim of the nanodot (see x -cut), but they do so at the upper and lower rim (y -cut). Even though the simulations reproduce most of the experimental observations, some minor discrepancies remain. In particular the plateau formed around the center by of the measured SNOM map and a very sharp ring around that central plateau are not reproduced. We believe that here the mode structure is disturbed by the particular shape of the nanodot, i. e., the dark shadow in the central region that was visible in the electron micrographs. As the height profile measured with the SNOM tip (Figure 4.8 (b) and (f)) did not reproduce the feature seen in the electron micrographs, this dark region may indicate a refractive index gradient, possibly caused by gas captured during collapse of the nanodot after annealing. Such a refractive index gradient could explain the observed deviation. Summarizing the projected LDOS calculations, they verify that the shape of the SNOM images resembles the projected LDOS given by four lowest-order bound modes of a circular waveguide with a dome-like surface topography.

4.3 Spectral response of Sb_2S_3 waveguide modes

In the following, we will employ spectrally resolved near-field measurements of a Sb_2S_3 nanodot to study these modes in more detail. In particular, we can approach this in two ways. Firstly, the waveguide modes proposed above provide a solution for a continuum of wavelengths. At a fixed spatial position, these modes should be excited across the complete spectral range covered by the broad-bandwidth laser and the scattered spectra therefore should show negligible spectral variation in our experiments. We will next present spectra recorded at different positions on the nanodot and the film to verify this behavior. Secondly, the spatial extent of LP fiber modes increases slightly with increasing wavelength. By spectrally filtering near-field maps obtained from a nanodot we will also verify this behavior.

4.3.1 Near-field spectrum and dipole model simulation

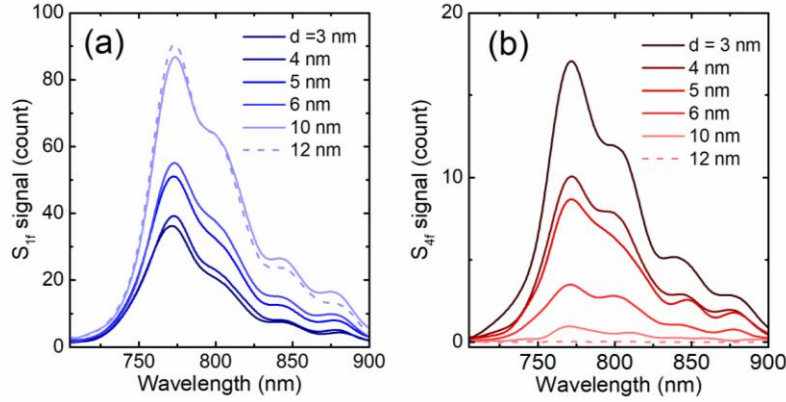


Figure 4.9 Spectrally resolved approach curves measured above the flat Sb_2S_3 film. (a) Spectra recorded on the Sb_2S_3 film, demodulated at the fundamental tip modulation frequency $S_{1f}(\lambda)$ as a function of tip-sample distance. Due to background interference the spectra change their shape as the tip is retracted. (b) The signal demodulated at the fourth harmonic, $S_{4f}(\lambda)$, retains its shape and decreases rapidly as the tip-sample distance increases.

In order to verify that near-field contrast is achieved also with BISNOM measurements, we record near-field spectra during an approach over the flat Sb_2S_3 film. Figures 4.9 (a) and (b) compare the spectra demodulated at the fundamental tip modulation frequency, $S_{1f}(\lambda)$, and spectra demodulated at the fourth harmonic, $S_{4f}(\lambda)$, for a few tip-sample distances between 3 nm and 12 nm. The $S_{1f}(\lambda)$ spectrum (Figure 4.9 (a)) increases in intensity, when the sample is removed from the tip, and the spectral shape changes. Both effects can be ascribed to interference of the reference field with a strong background signal scattered from the tip. In contrast, the $S_{4f}(\lambda)$ spectrum (Figure 4.9 (b)) decays strongly as the sample is removed from the tip; as the distance is increased by 12 nm, the signal has mostly vanished. During the process, the spectral shape is retained. In order to show that the measured $S_{4f}(\lambda)$ spectrum represents in good approximation the near-field spectrum, we have calculated the latter.

In Chapter 2, we introduced the dipole model of SNOM signal and concluded an effective polarizability describing the tip-sample coupling system. Ideally, a prober is approximated as a sphere with isotropic polarizability $\vec{\alpha}_{tip} = \vec{1} \cdot 4\pi \cdot R^3 (\epsilon_{Au} - \epsilon_{air}) (\epsilon_{Au} + 2\epsilon_{air})^{-1}$. However, the tips with conical or pyramidal shapes have longitudinal polarizability (along the taper cone) different from the transversal sphere resonances. This has been confirmed by finite-difference time-domain simulations¹⁶ and our previous experimental work.⁴⁴ Therefore, we assume the tip response is a diagonal polarizability tensor:

$$\vec{\alpha}_{tip}(\omega) = \begin{pmatrix} \alpha_{xx}(\omega) & 0 & 0 \\ 0 & \alpha_{yy}(\omega) & 0 \\ 0 & 0 & \alpha_{zz}(\omega) \end{pmatrix} \quad (4.6)$$

The transversal component $\alpha_{xx} = \alpha_{yy}$ can be described by the polarizability of a nanosphere with diameter of $r = 10\text{nm}$ and is shorten as $\alpha_{x,y}$:

$$\alpha_{x,y}(\omega) = 4\pi r^3 \cdot (\epsilon_{Au} - 1) / (\epsilon_{Au} + 2) \quad (4.7)$$

Here ϵ_{Au} is the dielectric functions of gold. And the longitudinal polarizability can be modeled by a Lorentz lineshape. More precisely, we have independently deduced resonance energies and linewidths for both components by broadband, polarization-resolved evanescent wave excitation,⁴⁴ and concluded resonance energy ($\hbar\omega_0$) and damping rate ($\hbar\gamma$) for the longitudinal resonance $\alpha_{zz}(\omega)$ of 1.58 eV and 0.33 eV and for the transversal resonance $\alpha_{x,y}(\omega)$ of 2.17 eV and 0.17 eV. Here the Lorentzian line shape functions hold the form of:

$$L(\omega) = \frac{|\mu^t|^2}{\hbar} \left(\frac{1}{\omega + \omega_0 + i\gamma} - \frac{1}{\omega - \omega_0 + i\gamma} \right) \quad (4.8)$$

As demonstrated in our previous work,⁴⁴ when the tip mode is mainly excited by the incident excitation, the effective dipole moment μ^t gives a maximum field enhancement factor of approximately 7 at the very apex of the taper as indicated in figure 4.10.

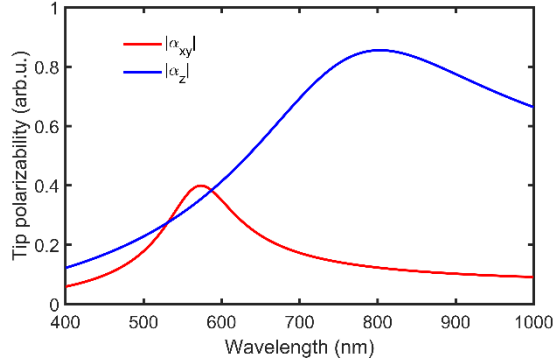


Figure 4.10 Longitudinal (blue curve) and transversal (red curve) polarizability of a gold tip with diameter 10 nm.

With incident electric field excitation, a dipole oscillation in the tip is activated. Following Knoll and Keilmann, the tip dipole causes a polarization in the material, which re-emits a field acting back on the tip dipole, effectively enhancing the incident field. This is described by an effective polarizability, which increases in a super-linear fashion as the tip-sample distance is decreased. For a specific wavelength, the effective polarizability tensor is:

$$\vec{\alpha}_{eff}(d) = \frac{\vec{\alpha}_{tip}}{1 - \frac{\vec{\alpha}_{tip}\beta}{32\pi d^3}} \quad (4.9)$$

Here, $\beta = (\epsilon_{Sb_2S_3} - 1)(\epsilon_{Sb_2S_3} + 1)^{-1}$ is the material response with the dielectric function of Sb_2S_3 (in Figure 4.2) and d is the tip-sample distance.

The near field radiated by the tip at position \vec{r}' and detected at position \vec{r} is calculated by applying the dyadic Green's function \vec{G} :

$$\vec{E}_{NF}(\vec{r}, d) = \vec{G}(\vec{r}, \vec{r}') \vec{\alpha}_{eff}(d) \vec{E}_{inc} \quad (4.10)$$

the dyadic Green function $\vec{G}_0(\vec{r}, \vec{r}')$ is defined as:

$$\vec{G}_0(\vec{r}, \vec{r}') = \frac{e^{ikR}}{4\pi R} \left[\left(1 + \frac{ikR-1}{k^2 R^2}\right) \vec{I} + \frac{3-3ikR-k^2 R^2}{k^2 R^2} \cdot \frac{\vec{R}\vec{R}}{R^2} \right] \quad (4.11)$$

Where R is the absolute value of vector $\vec{R} = \vec{r} - \vec{r}'$, and $\vec{R}\vec{R}$ denotes the outer product of \vec{R} with itself. According to the distance range R in comparison with the wavelength λ , the

Green function $\vec{G}_0(\vec{r}, \vec{r}_0, \omega)$ can be written as the addition of that for near-field, $G_{NF}(R \gg \lambda)$, intermediate-field, $G_{NF}(R \approx \lambda)$, and far-field, $G_{FF}(R \ll \lambda)$:

$$\vec{G}_0 = \vec{G}_{NF} + \vec{G}_{IF} + \vec{G}_{FF} \quad (4.12)$$

with

$$\vec{G}_{NF}(\vec{r}, \vec{r}_0, \omega) = \frac{e^{ikR}}{4\pi R} \cdot \frac{1}{k^2 R^2} \left(-\vec{I} + \frac{3\vec{R}\vec{R}}{R^2} \right) \quad (4.13)$$

$$\vec{G}_{IF}(\vec{r}, \vec{r}_0, \omega) = \frac{e^{ikR}}{4\pi R} \cdot \frac{i}{kR} \left(\vec{I} - \frac{3\vec{R}\vec{R}}{R^2} \right) \quad (4.14)$$

$$\vec{G}_{FF}(\vec{r}, \vec{r}_0, \omega) = \frac{e^{ikR}}{4\pi R} \left(\vec{I} - \frac{\vec{R}\vec{R}}{R^2} \right) \quad (4.15)$$

For the present experiments, with an incident field that is polarized in y-direction $\vec{E}_{inc} = E_{inc}\hat{y}$ parallel to the sample surface, we only consider the polarizability in y-direction (α_{yy}) of the gold tip. In Figure 4.11 (a) the yy matrix element of the effective polarizability (the only non-zero element under excitation with y-polarized light) is plotted as a function of wavelength for the same tip-sample distances d as were measured in the experiment and taking into account the dielectric functions of gold and of Sb_2S_3 . One can see that the effective polarizability increases as the tip-sample distance decreases. The increase towards short wavelengths is caused by the tip resonance, which is far detuned to the blue. This spectral shape is preserved during the approach.

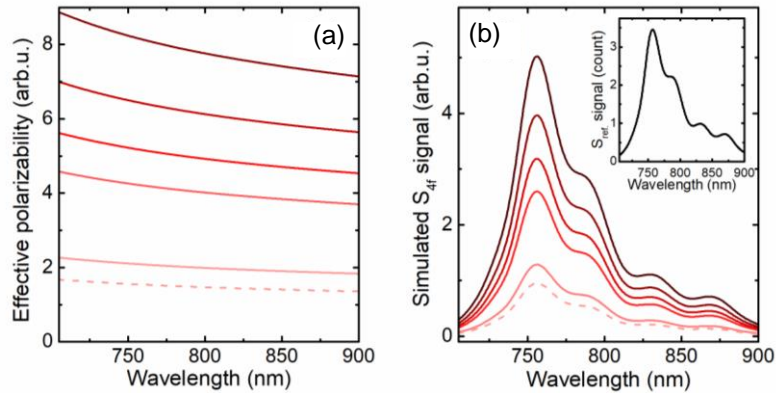


Figure 4.11 (a) Effective tip polarizability calculated for the same tip-sample distances as

used in the measurements, and (b) calculated near-field spectra. The inset shows the reference spectrum that was measured in the experiment and used as the input spectrum for the simulations. The calculated near-field spectra are in good agreement with the measured $S_{4f}(\lambda)$ spectra.

In order to calculate the near field radiated towards the detector, we apply the dyadic Green's function, but for this simple estimate we neglect its direction dependence. The near field is then mixed with the reference field to yield the measured near-field spectrum:

$$S_{NF}(\lambda, d) \propto k^2 Re \left\{ \left(\vec{\alpha}_{eff}(\lambda, d) \right)_{yy} \cdot E_R(\lambda) \cdot E_{inc}(\lambda) \right\} \quad (4.16)$$

Finally, one has to take into account the demodulation process that reduces the signal to its AC components. We do this numerically by subtracting the near field signal at a large tip-sample distance of 50 nm and approximate the measured $S_{4f}(\lambda, d)$ signal by

$$S_{4f}(\lambda, d) = S_{NF}(\lambda, d) - S_{4f}(\lambda, d_{far} = 50nm) \quad (4.17)$$

The result calculated by Equations (4.9), (4.16-17) are the near-field spectra shown in Figure 4.8 (d). The agreement with the measured S_{4f} spectra is excellent, both in spectral shape and in distance dependence.

4.3.2 Spatially resolved near-field spectrum

We now perform a spectrally resolved BISNOM scan of an Sb_2S_3 nanoparticle, using the monochromator and fast line camera. The laser spectrum used for this particular measurement is the one shown in the setup sketch Figure 4.1. We record complete near-field spectra $S_{1f}(\lambda)$, $S_{2f}(\lambda)$, $S_{3f}(\lambda)$, and $S_{4f}(\lambda)$, across a 500-nm by 400-nm large area, and with a step size of 12.5 nm and 20 nm in x and in y direction, respectively. In Figures 4.12 (a), (b), and (c) we show sets of these four spectra exemplarily for three different positions, in the center of the nanoparticle (Pos. 1, Figure 4.12 (a)), on the flat Sb_2S_3 film (Pos. 2, Figure 4.12 (b)), and on the outer area of the nanoparticle, where the near-field signal is strongly reduced (Pos. 3, Figure 4.12 (c)). The positions are marked in the SNOM map in the inset in Figure 4.12 (d), which has been prepared by plotting the spectrally integrated signal $S_{4f}(\lambda)$ as a function of position on the sample. Within each of

the Figure 4.12 (a)-(c) one can see that the measured $S_{2f}(\lambda)$, $S_{3f}(\lambda)$, and $S_{4f}(\lambda)$ spectra closely resemble each other, while the spectral shape of $S_{1f}(\lambda)$ clearly deviates from these and furthermore varies between the positions. In agreement with the observation shown in Figures 4.9(a) and (b), this leads us to conclude that the higher-order demodulated spectra reliably reflect near-field spectra, while spectral interference of background and reference fields leads to spectral variations in the $S_{1f}(\lambda)$ signal.

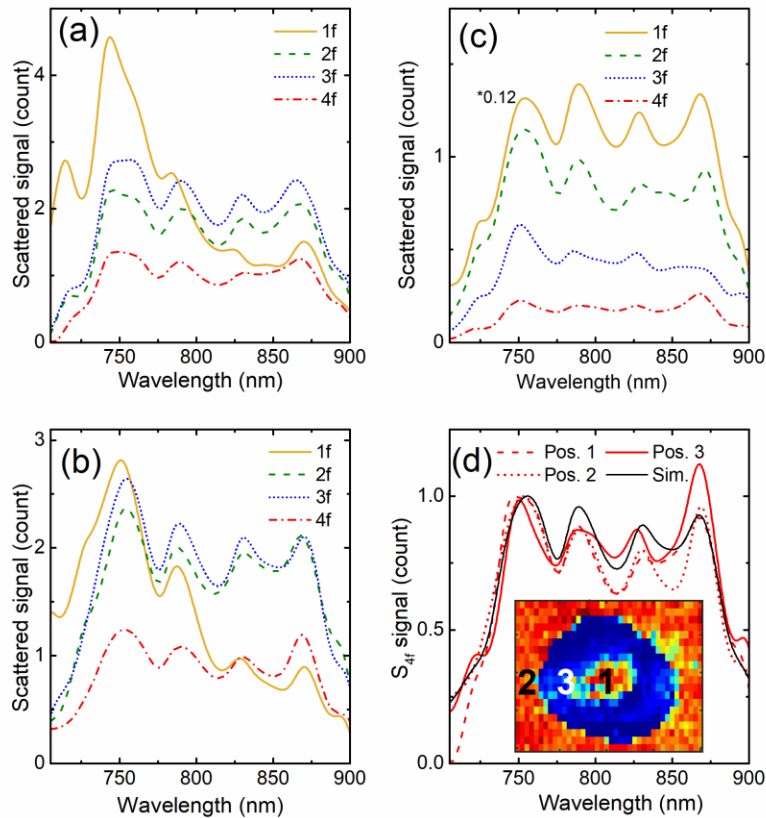


Figure 4.12 Near-field spectra recorded at different positions on an Sb_2S_3 nanoparticle using the monochromator and fast line camera. (a) Demodulated signals $S_{1f}(\lambda)$ to $S_{4f}(\lambda)$ recorded with the tip in close contact above the centre of the nanodot, (b), on the film, and (c), above the outer area on the nanodot. (d) Comparison of the three $S_{4f}(\lambda)$ spectra shown in (a)-(c) and a calculated $S_{4f}(\lambda)$ spectrum (black curve). The inset indicates the three positions, where the spectra shown in this figure are recorded.

In contrast, the higher-order demodulated spectra seem to hardly vary as the position on the sample is changed. In order to facilitate a direct comparison, the $S_{4f}(\lambda)$ spectra of the three positions are plotted together in Figure 12 (d). The black curve represents a near-field spectrum calculated from the effective polarizability above a flat Sb_2S_3 film and using the laser input spectrum shown in Figure 4.1. As expected, the $S_{4f}(\lambda)$ spectrum recorded on the film (Pos. 2, dotted red curve) matches the calculated spectrum well. A similar agreement can be seen for the $S_{4f}(\lambda)$ spectrum recorded at the center of the nanodot (Pos. 1, dashed red curve). This supports our interpretation of the central feature of the field profile as a waveguide mode, which has a broad bandwidth and is spectrally flat within our measurement range. Coupling into the waveguide is nearly wavelength-independent, which is reflected by the close resemblance of the calculated spectra and those measured on the film and the central area of the nanodot. The last spectrum, measured in the outer area of the nanodot, has a slightly different shape (Pos. 3, solid red curve): here the long-wavelength edge is markedly higher compared to the short-wavelength side. As known from fiber modes, the diameter of the waveguide mode increases slightly with wavelength. Thus, when probing at a radius that lies just at the edge of these modes, one would expect that the coupling efficiency for the shorter wavelengths has already dropped, while longer wavelengths still could be coupled to a guided mode with considerably higher efficiency. This would result in an overexpression of the longer-wavelength edge of the spectrum as observed in this measurement. Together, the measurements presented in Figure 4.12 verify the assumption of the broad bandwidth and flat spectral shape of the observed fundamental optical mode of the nanodot and supports modelling the dielectric structure as a waveguide. We have also seen first evidence of the typical spatial-spectral behavior of guided wave modes.

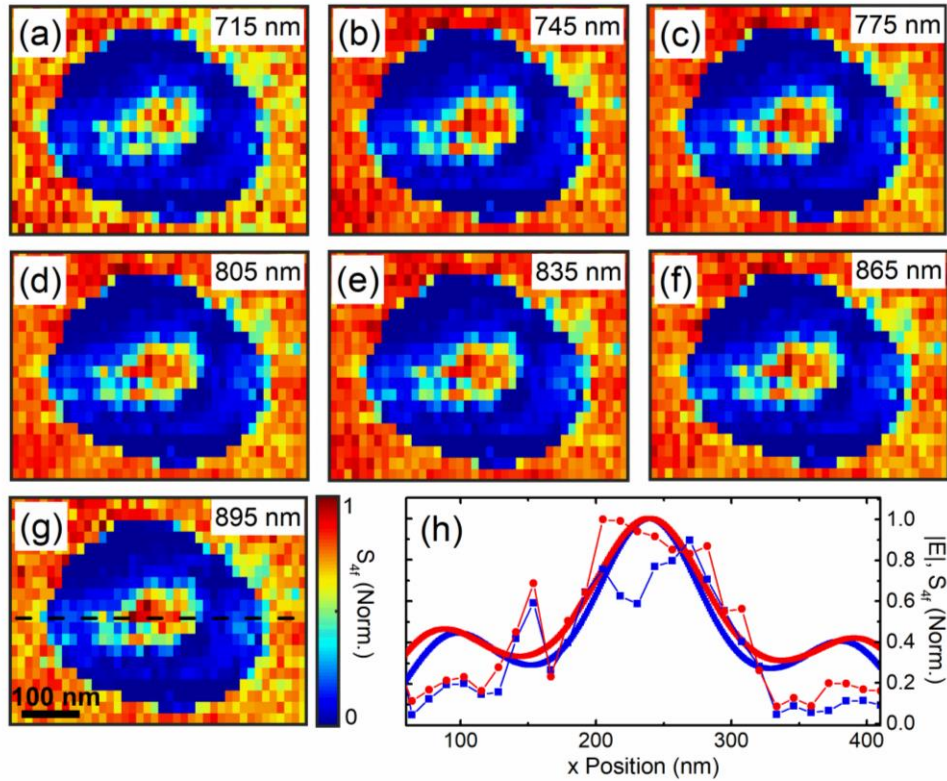


Figure 4.13 Spectrally resolved near-field maps of a Sb_2S_3 nanodot. (a)-(g) Near-field maps recreated from 30-nm spectral bands centered at 715, 745, 775, 805, 835, 865, and 895 nm. (h) Cross cuts through the near field maps shown in (a) (spectral range 700-730 nm, blue symbols) and in (f) (spectral range 850-880 nm, red symbols) together with calculated SNOM maps at 715 nm (blue curve) and 865 nm (red curve).

As a final verification of the spatial-spectral mode properties, we extract spectral near-field maps from the BISNOM data. In Figures 4.13(a)-(g) we have plotted maps created by spectrally integrating the $S_{4f}(\lambda)$ signal over 30-nm wide spectral bands, centered at equally spaced wavelengths from 715 nm to 895 nm. The contrast in these SNOM maps remains high throughout these seven spectral bands, which is yet another implication of the negligible spectral variation of the waveguide modes. At the short- and the long-wavelength edge, the measurement noise is increased due to the lower spectral power density of the laser. In each of these maps, a ring-shaped signal decrease can be seen

clearly. On closer inspection, the characteristic features from the projected LDOS calculation can be found here again, namely the secondary maxima at the left and lower right of the nanodot, and the near-zero signal regions at the top and bottom. Compared to the earlier investigated nanodot (cmp. Figure 4.8), here the main maximum appears to be more centered, which indicates that the nanodot is more regularly shaped.

Figure 4.13 (h) compares cross cuts through the maps created at the outermost spectral bands at 715 nm and 865 nm (Figures 4.13 (a) and (f), respectively) with calculated SNOM measurements above an elliptical surface over the LP_{01} , LP_{11} , LP_{02} , and LP_{21} mode profiles, once calculated for a wavelength of 715 nm and once for 865 nm. The measured values are shown as symbols in Figure 4.13 (h) and the calculated values as solid curves. As all curves are normalized, the larger extent of the long-wavelength mode is reflected by the lower decrease with larger radius (red curve). The general shape of the cross cuts through the measured near-field maps agrees well with the simulated projected LDOS. Unfortunately, the expected difference in diameter for the two different wavelength ranges cannot easily be seen in the measurements. The noise in these measurements is probably too high to see this small distinction. For example, there is one position, slightly left from the center, where the signal drops in both measured curves. Such a drop can appear due to a small dent on the surface of the nanostructure, where momentarily the tip-sample distance is increased. The larger extent of the waveguide mode at long wavelengths can, however, be seen in the measurement at larger radii, where the wings of the red symbols are clearly offset from the blue symbols. Together, the spectrally resolved near-field measurements presented in Figures 4.11 and 4.12 verify that the Sb_2S_3 nanodot supports LP-like waveguide modes.

This wavelength dependent waveguide model distribution is further supported by (FDTD) simulations. Figure 4.14 shows the intensity profiles of the fundamental modes LP_{01} and LP_{11} , calculated for a Gaussian-shaped spectrum of 20-nm width and centred at 700 nm (left column), at 800 nm (middle column), and at 900 nm (right column). From left to right, one can see that the extents of the two guided modes increases slightly with increasing wavelength. This matches our measurement results and calculation expectation illustrated in Figure 4.13.

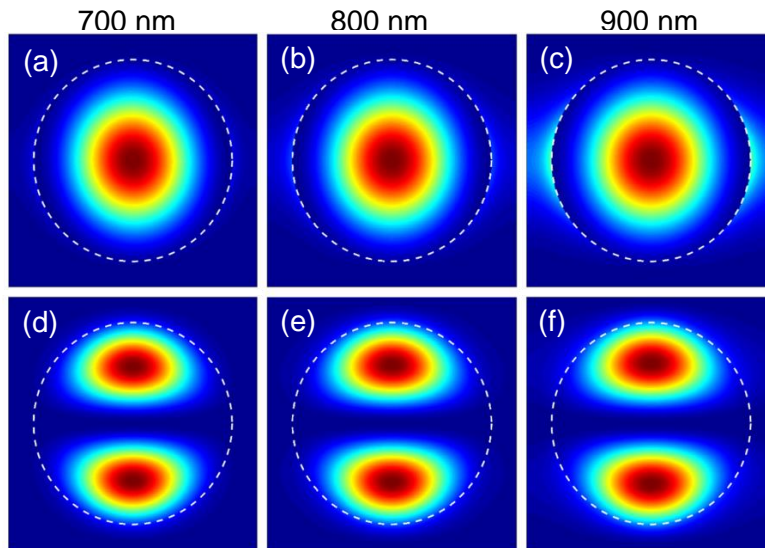


Figure 4.14 Intensity mode profiles obtained from finite-difference time domain (FDTD) simulations. Shown are the two lowest-order (a,b,c) mode LP_{01} , and (d,e,f) mode LP_{11} profiles calculated for a 20-nm width Gaussian laser spectrum centred at a wavelength of 700 nm, 800 nm, and 900 nm.

Figure 4.15 shows the crosscut through the calculated intensity profile of the LP_{01} mode for 700 nm, and 900 nm (black, and red curves). As displayed in figure 4.14 (h), the increasing diameter of the mode profiles is clearly visible in the measurements. A small increase in width is observed when the center wavelength increases from 700 nm to 900 nm in Figure 4.15, which is in good agreement with the simulated mode profile widths.

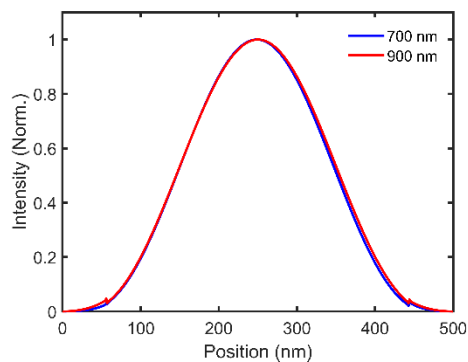


Figure 4.15 Cross cuts through the maps shown in Figure 4.14 (a) (spectral range 700-730 nm, blue curve) and in (c) (spectral range 850-880 nm, red curve).

In summary, we have realized scanning near-field optical spectroscopy with a broad bandwidth in the near-infrared. The key to the method is a fast CCD line camera capable of recording complete spectra with a read-out rate of more than eight times the tip modulation frequency, such that near-field spectra demodulated at the fourth order can be obtained in post-processing. Furthermore, we have incorporated the near-field microscope in a Michelson interferometer for homodyne mixing and boosting the weak near field signal.

We have demonstrated the potential of the broad-bandwidth interferometric near-field spectroscopy by experimentally investigating the optical modes supported by an Sb_2S_3 nanoparticle. We observe a round mode profile reminiscent of the fundamental fiber-optical mode. Near-field spectroscopy reveals that the observed mode is continuous across the bandwidth supported by our laser. Measuring near field spectra with high spatial resolution specifically at the outer edge of the observed mode profile reveals that here efficient coupling is retained predominantly for the longer-wavelength side of the spectrum. This indicates that the extent of the mode profile increases slowly with increasing wavelength and is a demonstration of the spatial-spectral mode characteristics. In agreement with FDTD simulations, the observation is that of a guided mode of the dielectric waveguide nanostructure. Such nanodots created on top of a thin film of the same material may serve as an efficient waveguide for below-band gap light into the film and thereby can help to improve the over-all efficiency of photovoltaic materials. In a different branch of applications, such dielectric nanostructures designed to support either guided or standing wave modes may in the future become an important alternative to metallic plasmonic nanostructures. Compared to those, dielectric nanostructures realize lower field enhancement, but they also cause much lower Ohmic losses, which makes them advantageous specifically for waveguide realizations in plasmonic circuitry. As such, the samples investigated in this report represent a novel class of basic plasmonic elements.

5 Time-domain response of single Halide Perovskite nanoparticles

Metallic, semiconducting and dielectric nanoparticles form outstanding tools for localizing light on the nanoscale. Their optical shape resonances confine light in certain localized modes and in spectral regions, largely tunable by varying the size, shape or composition of the particle. Such particles find broad applications in nanosensing, nonlinear optical switching, photocatalysis, and biomedicine. Often, the lifetimes of the optical resonance of those particles are so short, in the range of few femtoseconds, that direct time-resolved measurements of their localized optical near-fields are highly challenging. In this chapter, the broadband, interferometric scattering-type scanning near-field optical spectroscopy technique is utilized, setup details as described in chapter 3, to reconstruct the complex response function of a single nanostructure in the time domain and with nanometer-spatial resolution. We demonstrate this approach by analyzing single MAPbI₃ perovskite nanoparticles, promising new candidates for nanoscale light sources. Their optical spectra are expected to feature distinct Fano resonances, arising from the coupling of excitons to the Mie resonances of the particles. In this chapter, we provide direct evidence for these Fano resonances by measuring amplitude and phase of their local optical near-field with high spatial and spectral resolution. We identify a destructive interference dip in the time structure of the reconstructed optical near-field as the distinct signature of these Fano resonances. Our technique provides a general approach for measuring the response functions of nanostructures in the visible and near-infrared spectral range with femtosecond temporal and nanometer spatial resolution.

5.1 Sample preparation

Perovskite nanoparticles are fabricated by laser printing method from a perovskite thin film.^{121, 173} For preparing a uniform and dense perovskite film, a solution of perovskite precursor (MAPbI₃) is firstly prepared in a drybox as follows: methylammonium iodide (MAI) in γ -butyrolactone with dimethyl sulfoxide (GBL/DMSO) at the concentration of 1.5 M is used to dissolve 1.5 M of lead iodine (PbI₂). The solution is stirred and heated at

70 °C overnight and used after filtration through 0.45 µm PTFE syringe filter. With this solution, a perovskite layer is created by a solvent engineering technique inside the drybox.¹⁷⁴ First, the solution precursor MAPbI₃ is spread over the entire surface of the substrate at rotation speed 1000 rpm. The solvent is evaporated after maintaining the rotation for several tens of seconds. Then, 200 µL of toluene is dripped at 3000 rpm. During the film formation, the toluene does not dissolve perovskite. At last, the formed film is annealed at 100 °C for 10 min, converting the complex into highly uniform and crystalline perovskite.

For the laser printing method, the forward-transfer geometry is employed. The receiving substrate, glass substrate, is washed by sonication in deionized water, toluene, acetone, and isopropanol. Yb³⁺ femtosecond laser pulses at $\lambda = 1050$ nm with energy around 50 nJ is tightly focused by 10x objective with numerical aperture (NA) of 0.26. According to the relation $d \approx \frac{1.22\lambda}{NA}$, the diameter of the beam focal spot is approximately 5 µm. Previously prepared perovskite film is used as the sample for nanoparticle fabrication. It is placed on a three-dimensional air-bearing translating stage driven by brushless servomotors (ABL1000, Aerotech), allowing translation of the sample with an accuracy higher than 100 nm. In the experiment, the nanoparticles were fabricated from a smooth surface (in a single-shot regime) in the forward-transfer (LIFT) geometry when the receiving substrate is placed under the film with a spacing of ~ 50 µm.¹⁷³ Morphology and size of the nanoparticles are studied by scanning electron microscopy (SEM) with an electron microscope (Crossbeam 1540 XB, Carl Zeiss). An SEM image of MAPbI₃ nanoparticles on a glass substrate is depicted in Figure 5.1, which shows half-spherical shaped particles with radius of tens to hundreds of nanometers. Optical properties of nanoparticles and nanostructures are sensitive to the variations of shape, size, composition, and surrounding medium. Thus, it is vital to know exact morphology of the structure for proper description and further predictions of optical properties. Concerning to the influence of surrounding medium, it has been demonstrated that the presence of a silica glass substrate does not affect dramatically the mode excitation and spectral position of the resonances of a single high-index spherical nanoparticle.¹⁷⁵

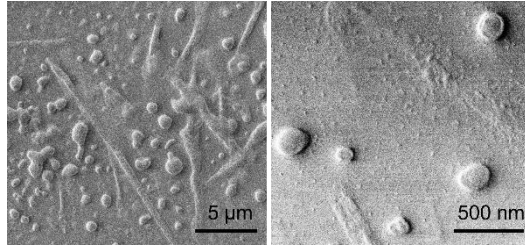


Figure 5.1 Scanning electron microscope image of MAPbI₃ particles fabricated by laser ablation.

Figure 5.2 shows the dielectric function ϵ of MAPbI₃ material measured by ellipsometry in previous works.^{176, 177} A pronounced onset is observed near the material bandgap at 1.642 eV. The imaginary part of ϵ , normally associated with the absorption component, can be decomposed by spectral fitting to an excitonic resonance and a continuum background as illustrated in figure 5.2 (b).

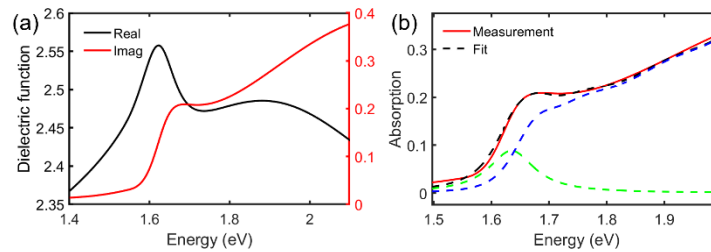


Figure 5.2 (a) Real (blue curve) and imaginary (red curve) parts of dielectric function for all perovskite nanoparticles composition MAPbI₃. (b) The imaginary part (red curve) is denoted as a combination of the excitonic resonance at 1.642 eV (green dashed line) and a continuum background (blue dashed line).

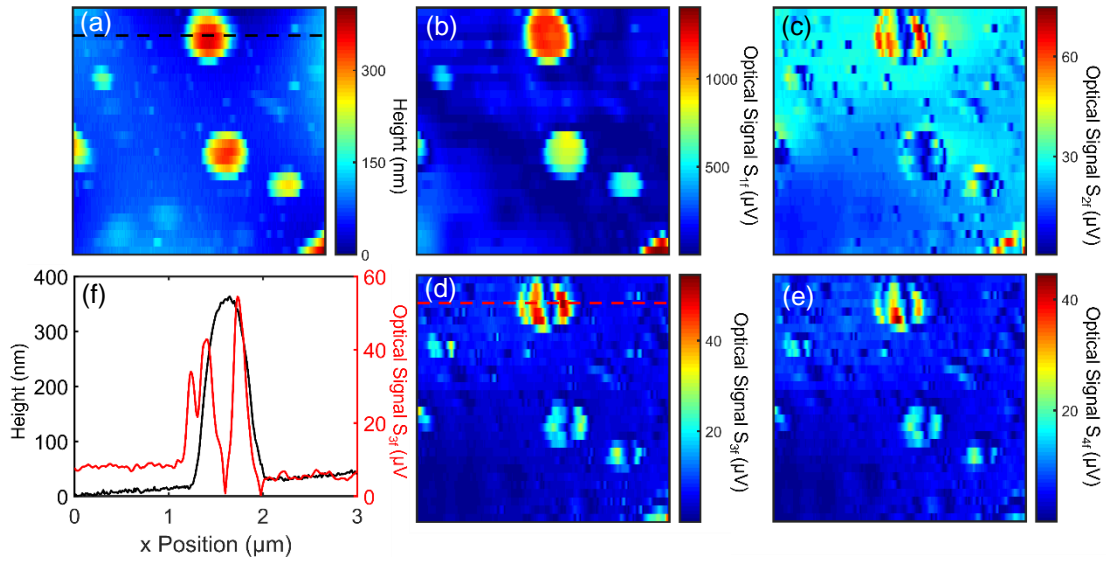


Figure 5.3 (a) Topography image of a $3\ \mu\text{m} \times 3\ \mu\text{m}$ area of a sample with laser-ablated MAPbI_3 nanoparticles on a glass cover slip. (b-e) Map of the optical near-field signal recorded for broadband excitation of the sample with a 6-fs Ti:sapphire laser and detected on an avalanche photodiode (APD). The signal is demodulated at the (b) first, (c) second, (d) third and (e) fourth harmonic of the tip modulation frequency. The fundamental order optical signal S_{1f} shows a stronger strength on the particles, which is originated from their high scattering cross section in far-field. Higher harmonic maps, S_{2f} , S_{3f} and S_{4f} , show dipolar field enhancement on the nanoparticle surface. It can be clearly depicted by the cross-section contrast, in panel (f), between the topography (black curve) and the S_{3f} optical signal (red curve) along dashed lines labeled in panel (a) and (d). The optical near-field signal displays evident enhancement within three stripe areas.

Figure 5.3 (a-e) display a SNOM scan of a typical area in the sample. The topographic image in panel (a) is acquired by scanning the sample as the tuning fork amplitude was adjusted to 12 nm and the tip-sample distance held at 4 nm. The nanostructures revealed by the AFM topography are correspondingly observed in the optical image S_{1f} (panel (b)). The signal strength on particles is evidently higher than that on the substrate, which benefits from the higher dielectric function of the halide perovskite in comparison with the glass substrate. Moreover, the near-field enhancement on the particles is stronger for the

large particles. This is because the near-field enhancement is directly related to the polarizability of the object which is, as indicated by the Keilmann dipole coupling model, proportional to the volume for a nanoparticle. For higher demodulation order, the optical image of each particle displays two lobes regardless of size and shape, which indicates that dipolar mode arises in MAPbI₃ particles under linearly polarized light excitation. As the demodulation order increases, optical contrast is improved. The near-field contrast in the signal S_{3f} is maximized. Cuts through of the topographic image and the S_{3f} map along the dashed lines in Figure 5.3 (a) and (d) are plotted together in panel (f). The topography contour (black curve) is a basically symmetric cone, and the S_{3f} signal outlines the dipolar mode, in which the signal increases as the tip reaches the particle edge and extremely decreases when it approaches to the center. An obvious dip can be observed within the left lobe which corresponds to the additional field enhancement near the particle rim in the S_{3f} image.

Such mode profile is demonstrated by an FDTD simulation of a MAPbI₃ half sphere as illustrated in figure 5.4. The simulated particle has comparable dimensions of the particle in the measurement as labeled by a black dash line in figure 5.3 (a). Optical images of the half sphere as shown in figure 5.4 (a-c) manifest that the optical modes for both x- and z-component have a dipolar mode profile under a linear polarized light excitation. Distinguishably, the x-component is tightly confined at the structural rim, while the dipolar mode for the z-component locates in the particle and exhibits an additional outer ring at the structural edges which coincides with the near-field mode feature probed in the measurement. Hence, we conclude that the tip in the measurement mainly probes the z-component of the particle. An overall signal as shown in figure 5.4(f), by integrating all three components with a larger proportion of the z-direction field distribution ($E_x:E_y:E_z = 1:1:6$), is employed to mimic the measured near-field mode distribution of individual MAPbI₃ nanoparticle.

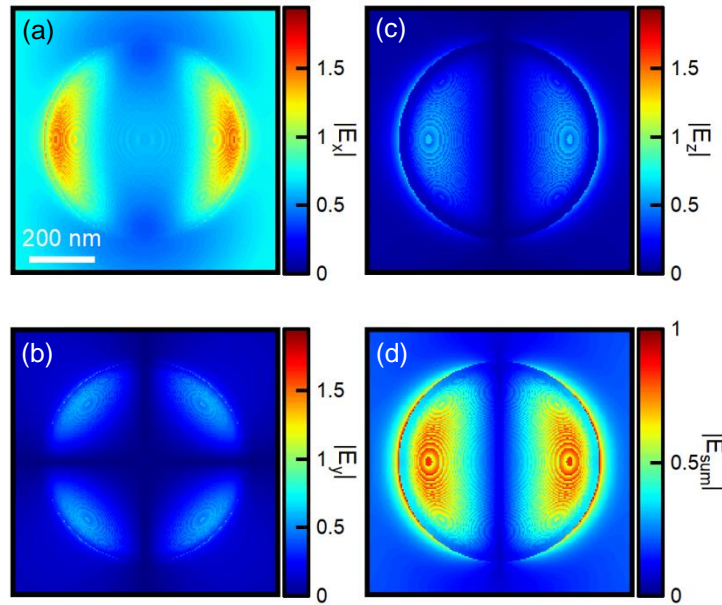


Figure 5.4 Map of the (a) x -, (b) y - and (c) z - component of the local optical near-field enhancement, averaged over a spectral range from 680 to 880 nm, at the surface of the MAPbI₃ nanoparticle. The field enhancement is simulated on a perovskite half sphere with radius of 300 nm and height of 300 nm, excited with an x -polarized plane wave. (d) Normalized absolute total electric field distribution around the particle where the different field components contribute with the of $E_x:E_y:E_z = 1:1:6$. In qualitative agreement with experiment, the integrated field shows a dipolar enhancement on the surface of the particle and a secondary field enhancement near the rim.

5.2 Near-field spectra

To understand the resonance property of the dipolar mode, we employ the broadband interference SNOM, as described in chapter 3, to study the near field spectrum of individual MAPbI₃ nanoparticle.

5.2.1 Measurement results

The local spectrum within an individual MAPbI₃ particle is measured by the fast camera employing homodyne interferometric detection. Figure 5.5(a) shows 60,000 spectra

$S(\omega, t)$ recorded consecutively at one position on the MAPbI₃ particle, by adapting the fast camera. The maximum readout speed of the camera is 210 kHz which corresponds to a line period of 4.6 μ s. Each horizontal line of the data image represents a spectrum, and the count per pixel is color-coded. The vertical straight stripes with a spacing of about 2 nm express the spectral interference fringes detuned by the optical path length difference of $\Delta L_R \approx 326$ nm. Each vertical line accumulates the pixelwise time series $S_\omega(t)$ integrated in 276 ms. Demodulated interferograms are obtained by performing discrete Fourier transformation of $S_\omega(t)$ for each specific energy ω (detailed information can be found in chapter 3). Figure 5.5 (b) and (c) depict the demodulated interferogram at n th order harmonic of tip frequency f , $S_{nf}(\omega)$, with demodulation order of $n = 0, 1, 2, 3, 4$.

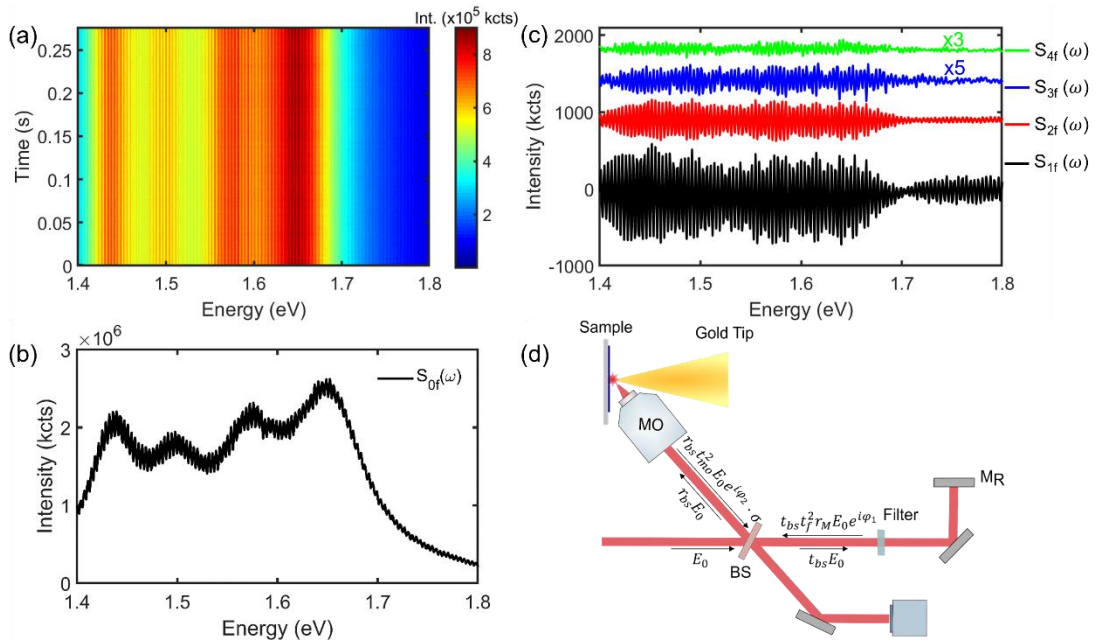


Figure 5.5 Near-field spectrum within the dipolar mode of a MAPbI₃ particle. (a) Counts collected by the fast line camera, color-coded as a function of energy and time $S(\omega, t)$. (b,c) Demodulated interferogram $S_{nf}(\omega)$ obtained by extracting the n th order ($n = 0, 1, 2, 3, 4$) Fourier series of the signal at each pixel plotted with a shift of dc-intensity offsets between orders for visibility. (d) A sketch of the interferogram in the BISNOM setup. The field propagating to the beam splitter (BS) is assumed as an incident field $E_0(\omega)$, and is

divided by the BS into two paths. The field expressions on the beam path are labeled where r and t denoting the reflection and transmission coefficients of optical elements, σ is the response parameter of the tip-sample area.

Recall the setup scheme as sketched in figure 5.5 (d), for an incident electric field $E_0(\omega)$, the detected output signal of the interferogram $S(\omega, t)$ is generally composed of three parts: near-field $E_{NF}(\omega)$ scattered from the tip apex, background field $E_B(\omega)$ scattered from the tip shaft, and reference field $E_R(\omega)$ reflected from the reference arm. As illustrated in panel (d), three fields can be expressed by the incident field and the optical properties of each element in the setup as follows:

$$\begin{aligned}
 E_R(\omega) &= t_{bs}(\omega)r_{bs}(\omega)t_f^2(\omega)r_M(\omega)E_0(\omega)e^{i\varphi_1(\omega)} \\
 E_B(\omega) &= t_{bs}(\omega)r_{bs}(\omega)t_{mo}^2(\omega)E_0(\omega)e^{i\varphi_2(\omega)} \cdot \sigma_S(\omega) \\
 E_{NF}(\omega) &= t_{bs}(\omega)r_{bs}(\omega)t_{mo}^2(\omega)E_0(\omega)e^{i\varphi_2(\omega)} \cdot \sigma_T(\omega)
 \end{aligned} \tag{5.1}$$

The reflection and transmission efficiency of BS, the transmission efficiencies of MO and gray filter, as well as the reflection efficiency of silver mirror has been measured and demonstrated to be wavelength independent as shown in the Appendix. Hence three fields can be simplified as:

$$\begin{aligned}
 E_R(\omega) &= h_1 E_0(\omega) e^{i\varphi_1(\omega)} \\
 E_B(\omega) &= h_2 E_0(\omega) e^{i\varphi_2(\omega)} \cdot \sigma_S(\omega) \\
 E_{NF}(\omega) &= h_2 E_0(\omega) e^{i\varphi_2(\omega)} \cdot \sigma_T(\omega)
 \end{aligned} \tag{5.2}$$

Here $\sigma_S(\omega) = |\sigma_S(\omega)|e^{i\varphi_S}$ and $\sigma_T(\omega) = |\sigma_T(\omega)|e^{i\varphi_T}$ denote the near-field and background field scattering response. $\varphi_{1,2}(\omega)$ is the phase of electric field from two arms in comparison to the phase of incident field $E_0(\omega)$ at the BS.

Therefore, the detected signal is the interference of three fields:

$$S(\omega) \propto |E_{NF}(\omega) + E_B(\omega) + E_R(\omega)|^2 \tag{5.3}$$

When the reference field is extremely strong, the interference signal demodulated at higher order ($n \geq 2$) harmonics is dominated by the product of near-field and reference field, for example:

$$S_{2f}(\omega) \propto \text{Re}\{h_1 h_2 \cdot |E_0(\omega)|^2 \cdot |\sigma_T(\omega)| \cdot e^{i(\Delta\varphi(\omega))}\} \quad (5.4)$$

where the phase delay $\Delta\varphi(\omega) = \varphi_1(\omega) - \varphi_2(\omega) = \frac{\omega(\Delta L)}{c_0}n$ is caused by the path length difference between reference field and near-field, and n is the refractive index of the medium on the optical path. In the case of propagation in air ($n = 1$), the phase delay is linearly proportional to frequency, $\omega\Delta L/c_0$. When n is frequency dependent, $\Delta\varphi(\omega)$ becomes a nonlinear function of frequency. Hence the phase term of $\Delta\varphi(\omega)$ can be written in two parts,

$$\Delta\varphi(\omega) = \omega \frac{\Delta L}{c_0} + \Delta\varphi_{NL}(\omega) = \omega\tau_0 + \Delta\varphi_{NL}(\omega) \quad (5.5)$$

According to the shift theorem of Fourier transformation, a linear phase in frequency domain corresponds to a time shift in time domain. Fourier transformation of $S_{2f}(\omega)$ therefore carries three components:

$$s_{2f}(t) = s_{2f}^-(t + \tau_0) + s_{2f}^0(t) + s_{2f}^+(t - \tau_0) \quad (5.6)$$

Three components correspond to three parts in the spectral interferogram signal $S_{2f}(\omega)$. For instance, the positive side peak in $s_{2f}(t)$ can be expressed as:

$$s_{2f}^+(t - \tau_0) = FT^{-1}\{h_1 h_2 \cdot |E_0(\omega)|^2 \cdot |\sigma_T(\omega)| \cdot e^{i\Delta\varphi(\omega)}\} \quad (5.7)$$

where FT^{-1} denotes inverse Fourier transform.

Figure 5.6 (a) shows the Fourier transformation of the interferogram $S_{2f}(\omega)$ on a logarithmic scale which contains one DC peak that centers at $t = 0$, and two symmetric AC peaks sitting at $t = -\tau_0$ and $t = +\tau_0$. The positive and negative AC peaks have identical absolute values and reversed phase signs. Applying rectangular windows, as indicated by dashed lines in panel (a), isolates the DC and AC components, then performing inverse Fourier transform to the positive AC peak $s_{2f}^+(t - \tau_0)$ yields the 2f

spectrum as shown in panel (b):

$$S_{2f}^-(\omega) = h_1 h_2 \cdot |E_0(\omega)|^2 \cdot \sigma_T(\omega) \cdot e^{i(\Delta\varphi(\omega))} \quad (5.8)$$

The essential information of the complex near-field response function is encoded in the $S_{2f}^-(\omega)$. From equation (5.8), the near-field response function $\sigma_T(\omega)$ amplitude and phase can be achieved by:

$$|\sigma_T(\omega)| = \frac{|S_{2f}^-(\omega)|}{h_1 h_2 \cdot |E_0(\omega)|^2} \propto \frac{|S_{2f}^-(\omega)|}{|E_0(\omega)|^2} \quad (5.9)$$

$$\varphi_T(\omega) = \text{Arg}(S_{2f}^-(\omega)) - \Delta\varphi(\omega) \quad (5.10)$$

Obviously, to realize the amplitude $|\sigma_T(\omega)|$ and phase $\varphi_T(\omega)$, both laser spectrum $|E_0(\omega)|^2$ and the phase delay $\Delta\varphi(\omega)$ are required, respectively.

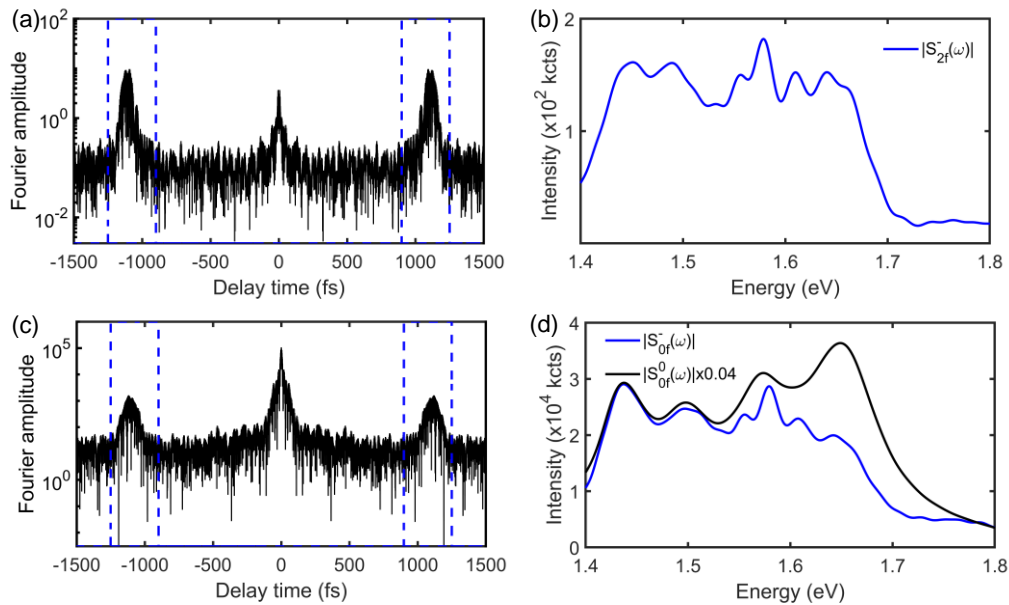


Figure 5.6 Normalized Fourier transform of (a) $S_{2f}(\omega)$ and (c) $S_{0f}(\omega)$ in logarithm which own one DC peak and two AC peaks, respectively. Applying two window boxes divides $s(t)$ data into three segments. Inverse Fourier transform of one side peak in $s_{2f}(t)$ and $s_{0f}(t)$ yield unmodulated spectrum (b) $S_{2f}^-(\omega)$ and (d) $S_{0f}^-(\omega)$, and Inverse Fourier transform the DC peak in $s_{0f}(t)$ yield the spectrum of $S_{0f}^0(\omega)$.

In $S_{0f}(\omega)$ signal, the near-field $E_{NF}(\omega)$ is negligible because it is much weaker than background field $E_B(\omega)$ and reference field $E_R(\omega)$. S_{0f} is approximated as the interference between reference field and background field:

$$\begin{aligned}
S_{0f}(\omega) &\approx |E_R(\omega) + E_B(\omega)|^2 \\
&= |h_1 E_0(\omega) e^{i\varphi_1(\omega)} + h_2 E_0(\omega) e^{i\varphi_2(\omega)} \cdot \sigma_S(\omega)|^2 \\
&= |E_0(\omega)|^2 h_1^2 \cdot \left(1 + \left(\frac{h_2}{h_1}\right)^2 |\sigma_S(\omega)|^2 + 2 \frac{h_2}{h_1} \cdot |\sigma_S(\omega)| \cos(\Delta\varphi(\omega))\right) \quad (5.11)
\end{aligned}$$

In analogy to the interferogram signal $S_{2f}(\omega)$, performing a Fourier transformation of $S_{0f}(\omega)$ leads to three components:

$$s_{0f}(t) = s_{0f}^-(t + \tau_0) + s_{0f}^0(t) + s_{0f}^+(t - \tau_0) \quad (5.12)$$

When three components are isolated as depicted in figure 5.6(c), separately performing inverse Fourier transformation of the isolated terms $s_{0f}^-(t + \tau_0)$ and $s_{0f}^0(t)$ results in the individual spectrum of $S_{0f}^-(\omega)$, $S_{0f}^0(\omega)$ as listed below:

$$S_{0f}^-(\omega) = |E_0(\omega)|^2 h_1^2 \cdot \left[\frac{h_2}{h_1} \cdot \sigma_S(\omega) e^{i\Delta\varphi(\omega)}\right] \quad (5.13)$$

$$S_{0f}^0(\omega) = |E_0(\omega)|^2 h_1^2 \cdot \left(1 + \left(\frac{h_2}{h_1}\right)^2 |\sigma_S(\omega)|^2\right) \quad (5.14)$$

A normalization of $|S_{0f}^-(\omega)|/|S_{0f}^0(\omega)|$ eliminates the coefficients of the laser spectrum $|E_0(\omega)|^2$ and gives a relationship of:

$$\frac{|S_{0f}^-(\omega)|}{|S_{0f}^0(\omega)|} = \frac{\frac{h_2}{h_1} \cdot |\sigma_S(\omega)|}{1 + \left(\frac{h_2}{h_1}\right)^2 |\sigma_S(\omega)|^2} \quad (5.15)$$

which forms a quadratic equation in terms of $\frac{h_2}{h_1} \cdot |\sigma_S(\omega)|$:

$$R \left(\frac{h_2}{h_1} |C_S(\omega)|\right)^2 - \frac{h_2}{h_1} |C_S(\omega)| + R = 0 \quad (5.16)$$

with $R = \frac{|S_{0f}^-(\omega)|}{|S_{0f}^0(\omega)|}$. Solving the quadratic equation results in two solutions:

$$|\sigma_S(\omega)| \propto \frac{1 \pm \sqrt{1-4R^2}}{2R} \quad (5.17)$$

This means that the background field scattering response amplitude can be calculated from the spectral shape ratio of R , and owns two solutions $|\sigma_S^+(\omega)| \propto \frac{1+\sqrt{1-4R^2}}{2R}$ and $|\sigma_S^-(\omega)| \propto \frac{1-\sqrt{1-4R^2}}{2R}$. Correspondingly, the laser spectrum can be obtained from equation (5.13):

$$|E_0(\omega)|^2 = \frac{|S_{0f}^-(\omega)|}{|\sigma_S(\omega)|} \quad (5.18)$$

Figure 5.7 (a) display the resulted laser spectrum $|E_0(\omega)|^2$ from two possible solutions $|\sigma_S^{\pm}(\omega)|$. The solid black curve resulted from the positive solution $|\sigma_S^+(\omega)|$ matches the laser spectral shape measured by the spectrometer, therefore $|E_0(\omega)|^2 = \frac{|S_{0f}^-(\omega)|}{|\sigma_S^+(\omega)|}$. Moreover, the laser spectrum further helps to calculate the near-field response function amplitude according to equation (5.9), $|\sigma_T(\omega)| \propto \frac{|S_{2f}^-(\omega)|}{|E_0(\omega)|^2}$ as shown in black curve in figure 5.7(d). An absorption shape is observed in $|\sigma_T(\omega)|$, and an evident spectral dip appears at around 1.72 eV.

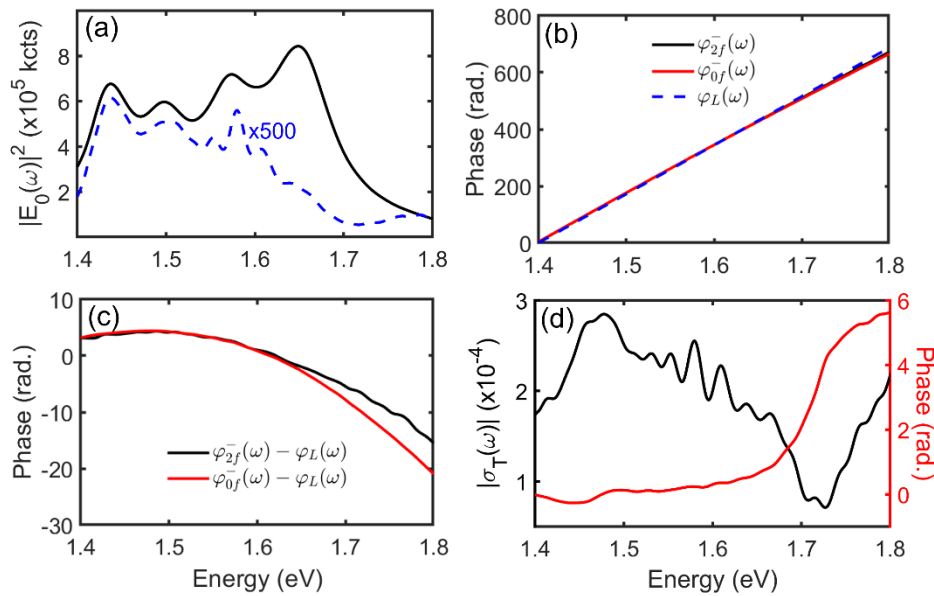


Figure 5.7 Retrieved (a) Spectrum of the incident light, (b) near-field response function

amplitude (black circles) and phase (red circles) of individual nanoparticle.

Regarding the phase of the near-field response function, it is encoded in the 2f spectral phase $Arg(S_{2f}^-(\omega)) = \varphi_T(\omega) + \Delta\varphi(\omega)$. The phase delay $\Delta\varphi(\omega)$ appears in the 0f spectral phase as well, $Arg(S_{0f}^-(\omega)) = \varphi_S(\omega) + \Delta\varphi(\omega)$, together with the phase term $\varphi_S(\omega)$ that stems from the reflection of the gold tip shaft. Because the dielectric function of gold in the energy range of 1.4eV-1.8eV shows small variations, it is taken as a constant. Therefore, the reflection phase $\varphi_S(\omega)$ of a gold surface is regarded as an offset in the 0f spectral phase. Hence, the near-field response function phase is approximated by $\varphi_T(\omega) \approx Arg(S_{2f}^-(\omega)) - Arg(S_{0f}^-(\omega))$.

Figure 5.7(b) displays the spectral phase of $S_{0f}^-(\omega)$ and $S_{2f}^-(\omega)$, both of which display a strong linear behavior. It is because of the reference arm and sample arm length difference caused linear phase delay $\omega\tau_0$ in the phase terms $\Delta\varphi(\omega)$. As indicated in figure 5.6(c), the time delay τ_0 can be determined from the Fourier transform of the interferogram. Therefore, the linear phase given by $\omega\tau_0$ is plotted in blue dashed curve in figure 5.7(b). Subtracting the linear portion from the spectral phase of $S_{0f}^-(\omega)$ and $S_{2f}^-(\omega)$, remaining phase components display a parabolic shape. Such nonlinear phase term of $\Delta\varphi(\omega) - \omega\tau_0$ originates from optical elements on the optical beam path that own frequency dependent refractive index, for example, the thick gray filter on the reference arm. Distinctly, the subtracted 2f spectral phase $\varphi_{2f}^-(\omega) - \varphi_L(\omega)$ has a step rising at around 1.7eV based on the parabolic curve. Hence, the near-field response function phase is given by $\varphi_T(\omega) \approx Arg(S_{2f}^-(\omega)) - Arg(S_{0f}^-(\omega))$ as depicted in figure 5.7(d). An obvious 2π phase jump is visualized at the absorptive dip position of $|\sigma_T(\omega)|$. Such amplitude dip and the phase jump behavior at around 1.7 eV indicates that a local resonance is probed. While conventional Lorentzian or Gaussian resonances display the characteristic phase jump by π . The retrieved 2π phase jump here originates from a Fano resonance which can be understood by considering the interference between two resonators. A detailed explanation of the observed resonance will be discussed in the next part.

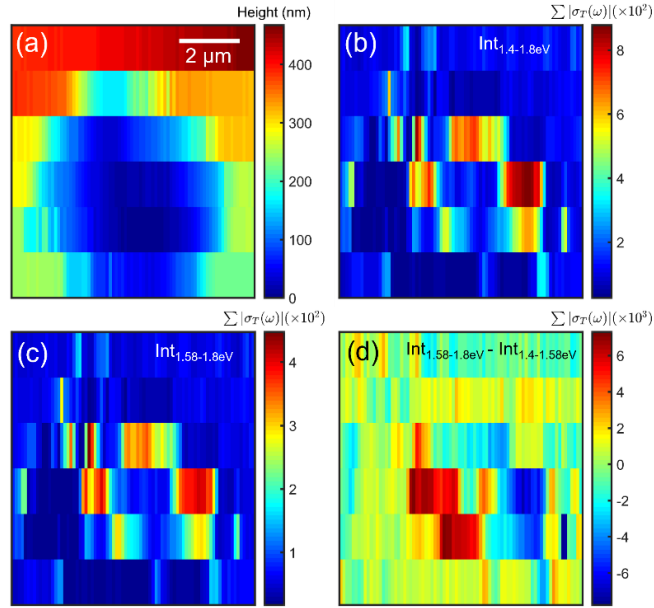


Figure 5.8 (a) Topography of a 400*480*450 nm MAPbI₃ nanoparticle. (b,c) Calculated near-field response function strength distribution of the MAPbI₃ nanoparticle obtained by integrating $|\sigma_T(\omega)|$ in the energy range of 1.4-1.8 eV, and (c) in the resonance energy range of 1.58-1.8 eV. (d) the resonance distribution obtained by subtracting the background of integration $|\sigma_T(\omega)|$ between 1.4-1.58 eV from the integration between 1.58-1.8 eV.

Based on the complex function $\sigma_T(\omega)$ reconstruction method, two dimensional spectral interferogram maps are studied. The fast camera data flow is recorded when the tip raster scans across an 800-nm by 900-nm area around the nanoparticle. The simultaneously probed topography is depicted in figure 5.8(a). Again, the demodulated interferogram $S_{0f}(\omega)$ and $S_{2f}(\omega)$ are used to retrieve the complex function $\sigma_T(\omega)$ at every position in the scan area. The images in figure 5.8(b) show the near-field response amplitude of the particle, which is obtained by spectrally integrating the $|\sigma_T(\omega)|$ in the spectral range and in a 2D area. In analogy to the near-field distribution shown in figure 5.3 (d), such response map mainly probes a dipolar mode and displays about x10 field enhancement within two lobes. Moreover, a more precise distribution of $|\sigma_T(\omega)|$ integrated in the resonance range between 1.58 and 1.8 eV is mapped in figure 5.8(c). The dominating

dipole feature is observed, and the noise level is smaller than panel (b). To further reveal the dipole mode contrast, the distribution image of $|\sigma_T(\omega)|$ beyond the resonance range, namely integrated from 1.4eV to 1.58eV, is subtracted from the image in panel (c). The response map shown in figure 5.8 (d) clearly sketches a dipolar mode profile with positive and negative poles.

5.3.3 Fano interference in a MAPbI₃ nanoparticle

Interference in Physics is generally an interaction of coherent waves, resulting in intensity variation (monochromatic light source) or spectral interference pattern (broad bandwidth light source) in a symmetric spectral shape. However, in certain cases, an asymmetric resonance can be obtained as a result of interference between a narrow spectrum from the discrete state and a broad spectral resonator mediated by continua states under light excitation, which is known as the famous Fano resonance. Such resonances are normally regarded as quantum mechanical phenomena. As illustrated in figure 5.9 (a), under excitation light, the transition from the ground state $|0\rangle$ to excited states can be realized by two alternative ways. For example, the continuum state $|C_i\rangle$ can be directly coupled to the ground state $|0\rangle$ by the incident light as depicted by the black arrows, or the incident photon is absorbed to the excited state $|1\rangle$ followed by a transition from $|1\rangle$ to the continuum state $|C_i\rangle$ via energy transfer as indicated by the blue arrow, vice versa. Therefore, the overall transition polarizability is the superposition of the polarizability amplitude through each channel, which could give rise to a constructive or destructive interference and produce asymmetric Fano profile as formulated by:

$$f(\varepsilon) = \frac{(q+\varepsilon)^2}{1+\varepsilon^2} \quad (5.19)$$

with the energy parameter $\varepsilon = 2 \frac{E-E_0}{\Gamma}$ with the incident light energy E and resonance energy E_0 and spectral width Γ of the discrete state,^{178, 179} $q = -\cot\left(\frac{\varphi}{2}\right)$ is the so-called Fano's asymmetry parameter, namely the Fano-type spectra have 4 characteristic shapes depending on the phase of the Lorentzian resonance from the discrete state in comparison to the broad bandwidth spectrum from the continuum. As shown in figure 5.9 (b-c), for the specific value of $q = 0$, the Fano spectrum shows a symmetric absorption

shape; for the extreme case of $q \rightarrow \pm\infty$, the spectrum has a symmetric Lorentzian peak, which indicates that the background continuum excitation vanishes; for a moderate value, $0 < q < \infty$ or $-\infty < q < 0$, the profile has asymmetric profile that is mirrored for opposite sign of q .

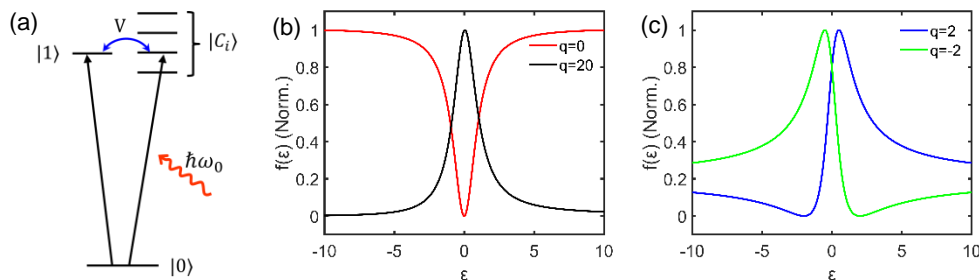


Figure 5.9 (a) Energy diagram describing the coupling scheme in a Fano resonance, where $|1\rangle$ and $|0\rangle$ are the excited and ground state respectively, $|C_i\rangle$ represents continuum states and V is the coupling strength. (b,c) Plots of Fano's formula as function of the reduced energy ϵ for different values of the parameter q . When q is very large, the Fano profile is basically a symmetric peak, and when q approaches to 0, a symmetric absorption window type resonance appears. For intermediate values, the Fano resonance shows asymmetric peak profiles.

Such characteristic spectral profiles can also be found in classical systems as described by the coupled harmonic oscillators (CHO), which is also called 'classical Fano resonance'. Apart from the similarity of spectral peak shape, the physical mechanism of the Fano parameter q was also clarified in the CHO.^{180, 181} Figure 5.10 illustrates the equivalent classical system where the continua and the discrete resonance are simulated as a damped oscillator S_1 and a harmonic oscillator S_2 . Two oscillators are fixed to walls and connected by a weak spring with constant K .

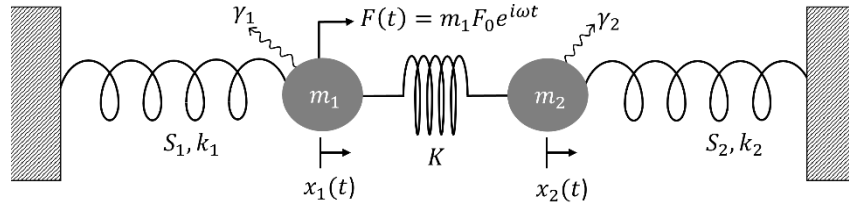


Figure 5.10 Two coupled harmonic oscillators. $k_{1,2}$ are the spring constants, $\gamma_{1,2}$ are the damping factors and $\gamma_1 > \gamma_2$, $x_{1,2}$ are the displacements from the equilibrium, K is the coupling spring constant between oscillator S_1 and S_2 , $F = m_1 F_0 e^{i\omega t}$ is the oscillatory external force.

Starting from Newton's equations of motion for point masses m_1 and m_2 , one gets the motion of the system of $m_1 \ddot{x}_1 = F_1$ and $m_2 \ddot{x}_2 = F_2$ where $F_{1,2}$ are the total force on the masses. For the oscillator S_1 , $F_1 = F_{1R} + F_{1D} + F_C + F_{ext1}$ where the restoring force is $F_{1R} = -kx_1$, the friction force $F_{1D} = -m_1 \gamma_1 \dot{x}_1$, the coupling force $F_C = K(x_1 - x_2)$, and the external force $F_{ext1} = m_1 F_0 e^{-i\omega t}$. For the oscillator S_2 , $F_2 = F_{2R} + F_{2D} - F_C + F_{ext2}$ where the restoring force is $F_{2R} = -kx_2$, the friction force $F_{2D} = -m_2 \gamma_2 \dot{x}_2$, and the external force $F_{ext2} = 0$. Hence the equations of motion are:

$$\begin{aligned} m_1 \ddot{x}_1 + m_1 \gamma_1 \dot{x}_1 + k_1 x_1 + K(x_1 - x_2) &= m_1 F_0 e^{i\omega t} \\ m_2 \ddot{x}_2 + m_2 \gamma_2 \dot{x}_2 + k_2 x_2 - K(x_1 - x_2) &= 0 \end{aligned} \quad (5.20 \text{ a})$$

For simplification, one assumes that $m_1 = m_2 = m$, and sets $\omega_1 = \sqrt{(k_1 + K)/m}$ and $\omega_2 = \sqrt{(k_2 + K)/m}$ as the uncoupled eigenfrequency, $v_{12} = -K/m$, then equation (5.20a) is given by:

$$\begin{aligned} \ddot{x}_1 + \gamma_1 \dot{x}_1 + \omega_1^2 x_1 + v_{12} x_2 &= F_0 e^{i\omega t} \\ \ddot{x}_2 + \gamma_2 \dot{x}_2 + \omega_2^2 x_2 + v_{12} x_1 &= 0 \end{aligned} \quad (5.20 \text{ b})$$

Taking the solution with the format of $x_1(t) = c_1(\omega) e^{i\omega t}$ and $x_2(t) = c_2(\omega) e^{i\omega t}$, and

substituting the solutions into equation (5.20 b), the amplitudes of steady state oscillation are obtained:

$$c_1(\omega) = \frac{\omega_2^2 - \omega^2 + i\gamma_2\omega}{(\omega_1^2 - \omega^2 + i\gamma_1\omega)(\omega_2^2 - \omega^2 + i\gamma_2\omega) - v_{12}^2} F_0 \quad (5.21)$$

$$c_2(\omega) = \frac{-v_{12}}{(\omega_1^2 - \omega^2 + i\gamma_1\omega)(\omega_2^2 - \omega^2 + i\gamma_2\omega) - v_{12}^2} F_0 \quad (5.22)$$

For the limit of vanishing coupling $v \rightarrow 0$, the amplitude $c_2(\omega) = 0$ is not visible (dark mode) and only the damped oscillator $c_1(\omega)$ is excited:

$$c_1(\omega) = \frac{1}{(\omega_1^2 - \omega^2 + i\gamma_1\omega)} F_0 \quad (5.23)$$

which is a single Lorentzian resonance showing a peak shape amplitude and a phase shift of $-\text{acot}((\omega^2 - \omega_1^2)/\gamma_1\omega)$ with respect to the external force. Therefore, for a weak coupling strength, the spectrum of $c_1(\omega)$ has response at frequency around $\omega = \omega_2$ due to the influence of the resonance $c_2(\omega)$, and such spectral response provides asymmetric resonance profiles. Analogy to the Fano profile depending on the q values, the asymmetric profile at $\omega = \omega_2$ is mainly determined by the intrinsic damping factor γ_1 of oscillator S_1 , according to the definition concluded in previous work,¹⁸⁰ $q = \frac{1}{\gamma_1\omega_2}(\omega_2^2 - \omega_1^2)$. When the coefficient γ_1 is large enough, namely q is super small, window type resonance emerges. This is coincident with the Fano profile as illustrated in figure 5.9.

Recall the transfer function spectral shape shown in figure 5.7, the spectral dip centered around 1.72 eV implies a Fano resonance in the individual MAPbI₃ perovskite nanoparticle. It has been demonstrated that such particles support strong excitonic resonances in the visible range.^{121, 182} In the nanoparticles, excitons are coupled to the Mie resonances of the dielectric nano resonator. The optical spectra of these hybrid nanoparticles therefore show two distinct types of shape resonances. In the first case, for the spectral region below the bandgap, far field light couples to the regular Mie resonances of a high-refractive index dielectric nano resonator. On the other hand, above the bandgap (about 1.61 eV for MAPbI₃), the Mie resonances are efficiently coupled to

the excitons of the material, making these nanoparticles an interesting antenna for enhancing light-exciton interaction. This gives rise to (a) distinct Kerker resonances¹⁸³⁻¹⁸⁵ reflecting the destructive interference in backward scattering direction between different Mie resonances in the region below the bandgap, (b) Fano resonances^{182, 186} due to exciton-Mie resonance coupling above the bandgap. Together, these phenomena result in rather complex single particle scattering spectra which have recently been studied for the first time.¹⁸² While dark field spectra of MAPbBr₃ particles in this work indeed showed some signatures of the expected Fano resonances, a definite assignment of spectral features around the bandgap to exciton Mie-resonance coupling is challenging due to the rather complex geometric shape of the individual particles. This is also a motivation for investigating these resonances in more detail in the present work.

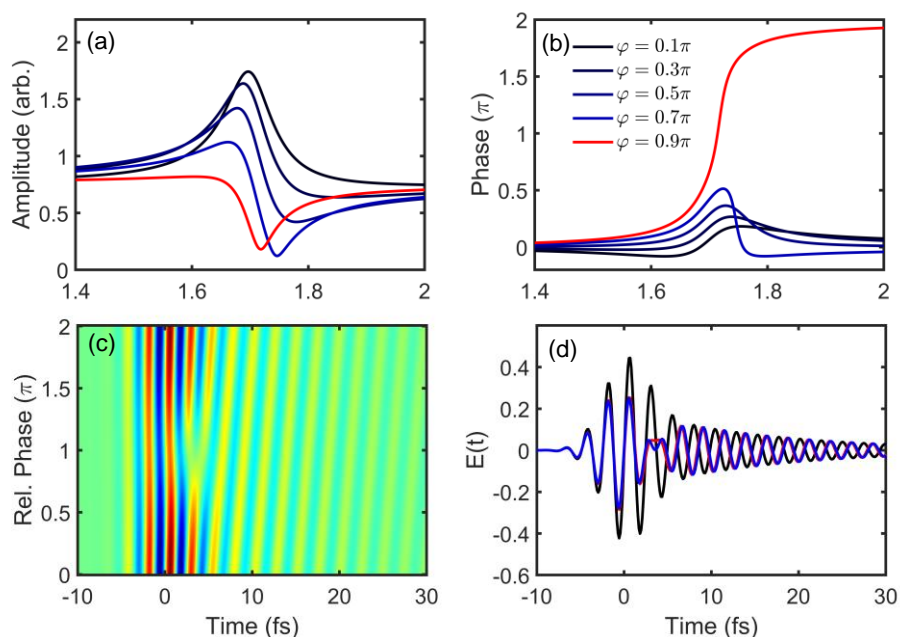


Figure 5.11. (a,b) Amplitude and spectral phase of a Fano-type response function (see equation (5.24)) with different relative phase between a spectrally sharp Lorentzian resonance and a broad background. The resonance parameters are chosen to match the light-scattering spectra from those of individual MAPbI₃ particles. When the amplitude of the Lorentzian resonance exceeds that of the background, a distinct phase jump of 2π is seen in the case of destructive interference, $\varphi = 0.9\pi$. (c) Time structure of the Fano-type response function after excitation with a broadband 6-fs Gaussian pulse for various

relative phase values. A dip in the time structure at around 5 fs for $\varphi = \pi$ is the signature of a destructive Fano-type interference between Lorentzian resonance and background, as illustrated in the inset of (d).

A distinct signature of such Fano resonances is their peculiar profile of their spectral phase. While conventional Lorentzian or Gaussian resonances display the characteristic phase jump by π , the spectral phase profile of the Fano resonances depends sensitively on the details of the coupling between the involved quasi particles. We can understand the spectral shape of a Fano resonance by considering the interference between the light from a quantum emitter coupled to the light that is emitted from the continuum.¹⁸⁷ Equation (5.24) expresses a simplified model of a Fano resonance, in which the phase of the light emitted from the continuum states is spectrally flat while that of the quantum emitter shows the characteristic π phase jump of a Lorentzian resonance. Thus, the relative phase between the fields changes as the color is tuned across the resonance, resulting in a complex amplitude and phase profile that depends sensitively on the relative amplitude and phase shift between resonance and continuum (figure 5.11 (a,b)). A particularly interesting case of a Fano resonance appears if quantum emitter and continuum interfere destructively at ω_0 . If the on-resonance amplitude of the emitter exceeds that of the background, the spectral phase shows a characteristic phase jump of 2π , as opposed to π phase jump for a single resonance. Such a destructive interference situation has in fact been anticipated for the investigated halide perovskite nanoparticles, when probing light scattering in backward direction.¹⁸² This makes it particularly interesting to probe amplitude and phase of the backscattered field from such particles in attempts to prove their Fano resonance behavior and to access the field dynamics. To gain more insights into the Fano resonance dynamics, we simulated the time- and relative phase-dependent field emitted from a Fano resonator, $f(t) * E_0(t)$ (figure 5.11(c)). The incident field $E_0(\omega)$ is a Gaussian pulse with a pulse duration of 6 fs and the resonant parameters of the Fano profile are described in figure 5.11 (a,b). A prominent dip appears after $f(t)$ and $E_0(t)$ overlap when the relative phase in the Fano resonance drops in the range of π to 2π , namely destructive interference occurs between the background and the Lorentzian resonance.

$$f(\omega) = iA_{bg} - \frac{A_L e^{i\varphi\gamma}}{\omega - \omega_0 + i\gamma} + \frac{A_L e^{-i\varphi\gamma}}{\omega + \omega_0 + i\gamma} \quad (5.24)$$

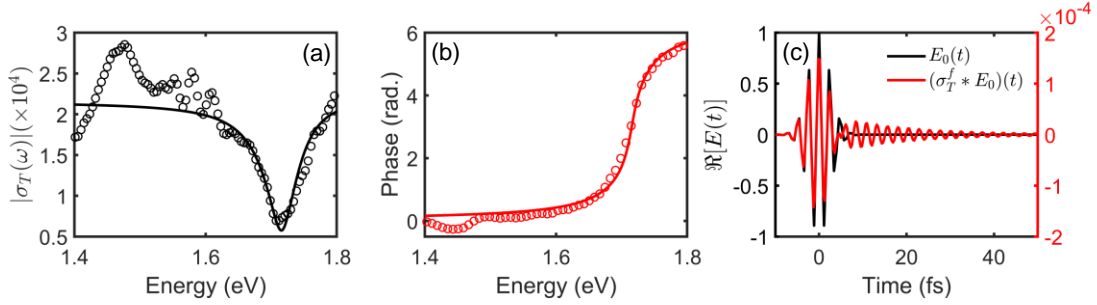


Figure 5.12 Transfer function $\sigma_T(\omega)$ (a) amplitude (black circles) and (b) phase (red circles) of the nanoparticle and fitted (solid lines) to a Fano-resonance line shape model $\sigma_T^f(\omega)$ as formulated in equation (5.24). (c) The time structure of a simulated incident Gaussian pulse $E_0(t)$, as well as the corresponding field dynamics of the MAPbI₃ nanoparticle $(\sigma_T^f * E_0)(t)$.

As claimed in figure 5.7, the retrieved near-field response function of a MAPbI₃ indicates a Fano resonance with destructive interference between the discrete mode and continuum background. At last, the complex function $\sigma_T(\omega)$ is fitted by the Fano model as depicted in figure 5.13. The fitting result $\sigma_T^f(\omega)$ reveals that the dipolar resonant mode in the MAPbI₃ particle is termed as the destructive interference between a background (Mie resonance) and a Lorentzian resonance (Excitonic resonance) that is specifically characterized by a resonant energy of $\hbar\omega_0 = 1.72 \text{ eV}$ and line width of $\hbar\gamma = 42 \text{ meV}$. Correspondingly, the field dynamic is calculated from $(\sigma_T^f * E_0)(t)$ where we assume the incident laser in frequency domain $E_0(\omega)$ is a Gaussian pulse centered at $\hbar\omega_0 = 1.72 \text{ eV}$ with pulse duration of 6 fs. In frequency domain, the Fano profile of the transfer function comprises a constant background and a Lorentzian resonance, which in time domain corresponds to a delta function and an exponential function decaying with a dephasing time $1/\gamma$ of about 15 fs. Therefore, the re-emitted field dynamics of the sample is a convolution of a Gaussian pulse and an exponential function together with a delta function as illustrated in figure 5.12(c).

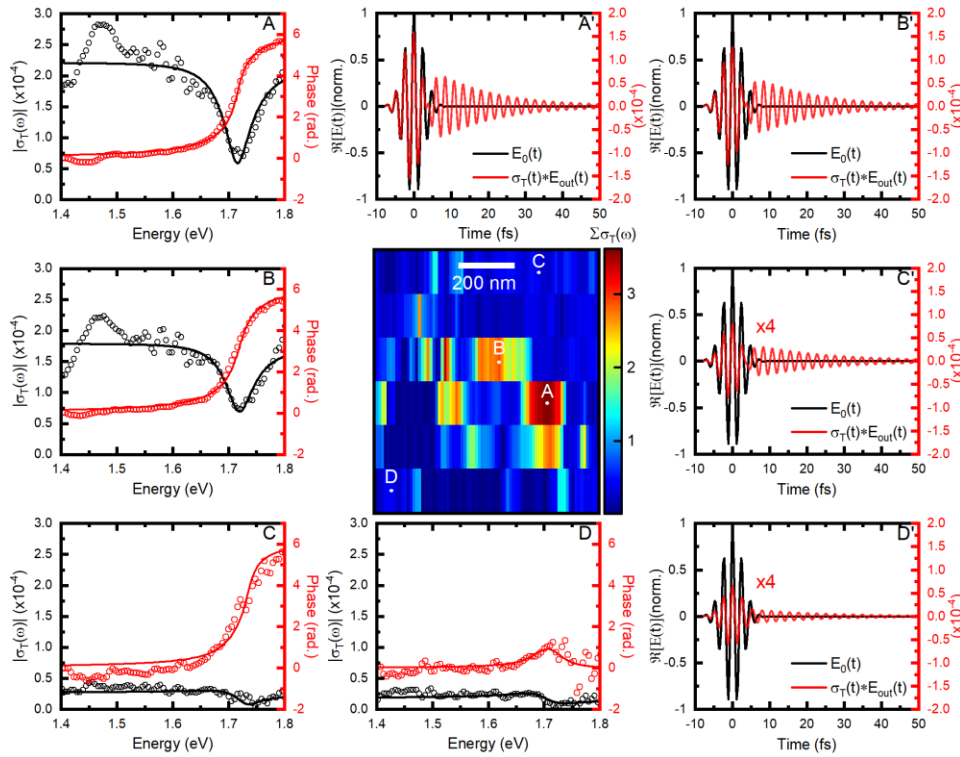


Figure 5.13 Calculated transfer function strength distribution of the MAPbI_3 nanoparticle. The white dashed curve roughly outlines the particle position. (A-D) Reconstructed (circles) and fitted (solid curves) complex transfer function at different positions. (A'-D') The corresponding field dynamics of the MAPbI_3 nanoparticle $(E_0 * \sigma_T^f)(t)$ as well as the simulated incident Gaussian pulse $E_0(\omega)$.

Figure 5.13 A,B display the reconstructed transfer functions on the particle as well as the fit results, which demonstrate that the particle response σ_T in the dipolar mode consistently shows a clear absorption line curve with a 2π phase jump. At the edge of the particle (position C) away from the dipolar mode, the absorptive contrast of the transfer function reduces while the 2π phase jump holds. In contrast, at the position on the substrate (position D), the response function shows a noisy curve due to the low near-field enhancement. Figure 5.13 A'-D' exhibit unified exponential profiles, and the intriguing dip at around 3fs is observed in the dipolar mode, which as proposed is caused by the destructive interference between the Mie resonance and the exciton.

In this chapter, we have analyzed single MAPbI₃ perovskite nanoparticles by employing broad-bandwidth interferometric near-field spectroscopy. We observe a dipolar mode profile on every individual particle. In agreement with FDTD simulations, the observed near-field image dominantly probes the z-component of the particle resonance.

By employing the Fourier technique, both amplitude and phase of the near-field response are reconstructed from the measured spectral interferometry. The complex response function reveals a Fano resonance which shows an absorptive spectral amplitude centered at about 1.72 eV and 2π jump in the phase. This Fano resonance stems from the featured coupling of the excitons and the Mie resonances in the Halide Perovskite nanoparticle. Moreover, we identified a distinct destructive interference dip in the time structure of the reconstructed optical near-field as the distinct signature of these Fano resonances. It has been demonstrated that such resonance arises when the on-resonance amplitude of the emitter exceeds that of the background, which reveals that in individual MAPbI₃ nanoparticle the excitons have stronger resonance. This is rarely observed because in far-field detection the Mie resonances have much higher scattering efficiency.

6 Conclusion and Outlook

In this thesis, a new interferometrically detected scanning near-field optical spectroscopy technique with a broad bandwidth in the near-infrared is realized. We have identified and designed a near-field microscope in a Michelson interferometer for homodyne mixing and boosting the weak near-field signal that allows disentangling near-field and background-related signal contributions by mixing the near field with a strength adjustable reference field. We have shown that this efficiently amplifies the near field and suppresses the background light, such that when demodulating the signal with the second or third harmonic of the tip modulation frequency mainly the near field is detected.

The key to this method is a fast CCD line camera capable of recording complete spectra with a readout rate of more than eight times the tip modulation frequency such that near-field spectra demodulated at the fourth order can be obtained in postprocessing. With the homodyne detection scheme and with the fast line camera, we have measured pure near-field spectra over a broad bandwidth in the visible spectral region. Our measured and calculated optical signals verify and demonstrate the challenging effect of background signals in scattering-type SNOM. Interference between light that is reflected from the sample and light that is scattered from the tip shaft dominates the measured signal. For broad-bandwidth spectroscopy, this results in spectral interference that basically determines the shape of the measured spectra. In this thesis, we have shown that a reference field of sufficient amplitude can achieve efficient background suppression. The reference field then amplifies the near field such that at demodulation at the second or third harmonic of the tip modulation frequency results in the very precise detection of the near field.

We have demonstrated the potential of broad-bandwidth interferometric near-field spectroscopy by experimentally investigating the optical modes supported by individual Sb_2S_3 nanodots deposited on an Sb_2S_3 thin film. The near-field measurements reveal mode profiles reminiscent of low-order optical modes typical for more idealized cylindrical

waveguides. These modes are seen in near-field spectra across the entire bandwidth supported by our laser while we find no clear signatures for spectrally sharp Fabry–Perot resonances of the nanodots. These results show that the Sb_2S_3 nanodots can act as high refractive-index dielectric waveguides with low losses in a broad spectral range below the bandgap. Together with their high above-bandgap absorption, their high photoconductivity, and the possibility for easy 2D and 3D structuring, this makes them promising candidates as switchable metamaterials. It will be highly interesting to investigate their nonlinear properties in future works.

More intriguingly, we utilized this technique to reconstruct the amplitude and phase of the linear optical near-field response from the hot spots of a single MAPbI_3 perovskite nanoparticle with high spatial resolution, and further resolved a destructive interference dip in the time structure of the reconstructed optical near-field as the distinct signature of these Fano resonances. We show that this destructive interference dip in the time domain response of the particle is the distinct signature of a Fano resonance that arises from the coupling of the excitons to the Mie resonances of the particle. Our technique provides a general approach for measuring the response functions of nanostructures in the visible and near-infrared spectral range with femtosecond temporal and nanometer spatial resolution.

In summary, we have made considerable progress towards broadband s-SNOM spectroscopy in the visible spectral range. We have realized an homodyne interferometer for mixing the near field with a strong reference field by depositing a thin gold film on the sample substrate and covering it with a thin dielectric layer. We have shown that this efficiently amplifies the near field and suppresses the background light. Using a fast line camera, we have recorded complete spectra in tip-modulated s-SNOM. By post-measurement extraction of spectra demodulated with the fourth-order harmonic frequency we have acquired pure near-field spectra in over a broad bandwidth of the visible spectral region. Employing Fourier-transform technique, we retrieved the inherent resonance property in an individual nanoparticle and further, Our results open up a new

approach towards quantitative, ultrahigh resolution, broadband near-field scattering spectroscopy.

Appendix A: Wavelength dependency of optical elements in the BISNOM setup

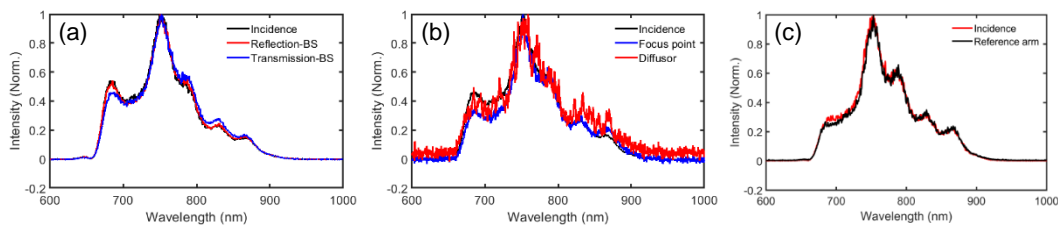


Figure S5.1 Spectral shape comparison between the incident light and the light (a) reflected and transmitted by the beam splitter, (b) focused by the reflecting objective, in which the focused spectrum is measured by two approaches, either positioning the spectrometer at the focus point or detecting the scattering light using a diffusor. (c) Spectral shape comparison between the incident light and the incident light reflected by the reference arm.

The spectral shape of light transmitting the beam splitter resembles the incident laser spectrum and the reflected spectrum. Therefore, in our spectral range, the reflection and transmission of the beam splitter are wavelength independent and can be set as a constant. For the reflecting objective, the transmitted focusing light is measured either by a diffusor or by positioning the fiber detector at the focused position. The resulting spectral shapes are identical and resemble the incident spectrum. This demonstrates that the transmission of the reflecting objective is a constant in the detected wavelength range. The transmission of the ND filter is demonstrated in panel (c). When the sample arm is blocked, the reflected light on the reference arm at the detector position shows an unchanged spectral shape (black curve) compared to the incident spectrum (red curve). Hence the transmission of the filter is also wavelength independent.

References

1. Novotny, L.; Hecht, B., *Principles of nano-optics*. Cambridge university express: Cambridge, 2006.
2. Abbe, E. A., Beiträge zur Theorie des Mikroskops und der mikroskopischen Wahrnehmung. *Arch. Mikrosk. Anat.* **1873**, *9*, 413-468.
3. Syngé, E. H., A suggested method for extending microscopic resolution into the ultra-microscopic region. *Philos. Mag.* **1928**, *6* (35), 356-362.
4. Binnig, G.; Rohrer, H.; Gerber, C.; Weibel, E., Tunneling through a controllable vacuum gap. *Appl. Phys. Lett* **1982**, *40* ((2).), 178-180.
5. Lewis, A.; Isaacson, M.; Harootunian, A.; Muray, A., Development of a 500-a spatial resolution light microscope. *Ultramicroscopy* **1984**, *13*, 227-231.
6. Pohl, D. W.; Denk, W.; Lanz, M., Optical stethoscopy: Image recording with resolution $\lambda/20$. *Applied Physics Letters* **1984**, *44* (7), 651-653.
7. Betzig, E.; Lewis, A.; Harootunian, A.; Isaacson, M.; Kratschmer, E., Near field scanning optical microscopy (NSOM): development and biophysical applications. *Biophys. J.* **1986**, *49*, 269-279.
8. Harootunian, A.; Betzig, E.; Isaacson, M.; Lewis, A., Super - resolution fluorescence near - field scanning optical microscopy. *Applied Physics Letters* **1986**, *49* (11), 674-676.
9. Dürig, U.; Pohl, D. W.; Rohner, F., Near - field optical - scanning microscopy. *Journal of Applied Physics* **1986**, *59* (10), 3318-3327.
10. Betzig, E.; Chichester, R. J., Single Molecules Observed by Near-Field Scanning Optical Microscopy. *Science* **1993**, *262*, 1422-1425.
11. Trautman, J. K.; Macklin, J. J.; Brus, L. E.; Betzig, E., Near-field spectroscopy of single molecules at room temperature. *Nature* **1994**, *369*, 40-42.
12. Xie, X. S.; Dunn, R. C., Probing Single Molecule Dynamics. *Science* **1994**, *265*, 361-364.
13. Zenhausern, F.; O' Boyle, M. P.; Wickramasinghe, H. K., Apertureless near - field optical microscope. *Applied Physics Letters* **1994**, *65* (13), 1623-1625.
14. Bachelot, R.; Gleyzes, P.; Boccara, A. C., Near-field optical microscope based on local perturbation of a diffraction spot. *Opt. Lett.* **1995**, *20*, 1924-1926.
15. Inoué, Y.; Kawata, S., Near-field scanning optical microscope with a metallic probe tip. *Opt. Lett.* **1994**, *19*, 159-161.
16. Zenhausern, F.; Martin, Y.; Wickramasinghe, H. K., Scanning Interferometric Apertureless Microscopy: Optical Imaging at 10 Angstrom Resolution. *Science* **1995**, *269*, 1083-1085.

17. Kawata, S.; Inouye, Y., Scanning probe optical microscopy using a metallic probe tip. *Ultramicroscopy* **1995**, *57*, 313-317.
18. Kohei, I.; Tetsuhiko, N.; Hiromi, O., Imaging of Surface Plasmon and Ultrafast Dynamics in Gold Nanorods by Near-Field Microscopy. *J. Phys. Chem. B* **2004**, *108*, 16344-16347.
19. Imaeda, K.; Hasegawa, S.; Imura, K., Imaging of Plasmonic Eigen Modes in Gold Triangular Mesoplates by Near-Field Optical Microscopy. *The Journal of Physical Chemistry C* **2018**, *122* (13), 7399-7409.
20. Xu, Y.; Tucker, E.; Boreman, G.; Raschke, M. B.; Lail, B. A., Optical Nanoantenna Input Impedance. *ACS Photonics* **2016**, *3* (5), 881-885.
21. Hillenbrand, R.; Keilmann, F., Optical oscillation modes of plasmon particles observed in direct space by phase-contrast near-field microscopy. *Applied Physics B* **2014**, *73* (3), 239-243.
22. Krachmalnicoff, V.; Cao, D.; Caze, A.; Castanie, E.; Pierrat, R.; Bardou, N.; Collin, S.; Carminati, R.; De Wilde, Y., Towards a full characterization of a plasmonic nanostructure with a fluorescent near-field probe. *Opt Express* **2013**, *21* (9), 11536-45.
23. Alonso-Gonzalez, P.; Albella, P.; Neubrech, F.; Huck, C.; Chen, J.; Golmar, F.; Casanova, F.; Hueso, L. E.; Pucci, A.; Aizpurua, J.; Hillenbrand, R., Experimental verification of the spectral shift between near- and far-field peak intensities of plasmonic infrared nanoantennas. *Phys Rev Lett* **2013**, *110* (20), 203902.
24. Alonso-Gonzalez, P.; Schnell, M.; Sarriugarte, P.; Sobhani, H.; Wu, C.; Arju, N.; Khanikaev, A.; Golmar, F.; Albella, P.; Arzubiaga, L.; Casanova, F.; Hueso, L. E.; Nordlander, P.; Shvets, G.; Hillenbrand, R., Real-space mapping of Fano interference in plasmonic metamolecules. *Nano Lett* **2011**, *11* (9), 3922-6.
25. Rang, M.; Jones, A. C.; Zhou, F.; Li, Z.-Y.; Wiley, B. J.; Xia, Y.; Raschke, M. B. J. N. I., Optical near-field mapping of plasmonic nanoprisms. *Nano Lett* **2008**, *8* (10), 3357-3363.
26. Olmon, R. L.; Krenz, P. M.; Jones, A. C.; Boreman, G. D.; Raschke, M. B., Near-field imaging of optical antenna modes in the mid-infrared. *Optics express* **2008**, *16* (25), 20295-20305.
27. Esteban, R.; Vogelgesang, R.; Dorfmueller, J.; Dmitriev, A.; Rockstuhl, C.; Etrich, C.; Kern, K. J. N. I., Direct near-field optical imaging of higher order plasmonic resonances. **2008**, *8* (10), 3155-3159.
28. Imura, K.; Nagahara, T.; Okamoto, H., Near-field optical imaging of plasmon modes in gold nanorods. *J Chem Phys* **2005**, *122* (15), 154701.
29. S., D.; Z., F.; Q., M.; S., R. A.; M., W.; S., M. A.; K., L. M.; W., G.; W., R.; K., W.; T., T.; M., T.; G., D.; H., C. N. A.; A., Z.; F., K.; P., J.-H.; M., F. M.; N., B. D., Tunable Phonon Polaritons in Atomically Thin van der Waals Crystals of Boron Nitride. *Science* **2014**, *343*, 1125-1129.
30. Gerber, J. A.; Berweger, S.; O'Callahan, B. T.; Raschke, M. B., Phase-resolved surface plasmon interferometry of graphene. *Phys Rev Lett* **2014**, *113* (5), 055502.

31. Woessner, A.; Lundeberg, M. B.; Gao, Y.; Principi, A.; Alonso-Gonzalez, P.; Carrega, M.; Watanabe, K.; Taniguchi, T.; Vignale, G.; Polini, M.; Hone, J.; Hillenbrand, R.; Koppens, F. H., Highly confined low-loss plasmons in graphene-boron nitride heterostructures. *Nat Mater* **2015**, *14* (4), 421-5.
32. Hu, D.; Yang, X.; Li, C.; Liu, R.; Yao, Z.; Hu, H.; Corder, S. N. G.; Chen, J.; Sun, Z.; Liu, M.; Dai, Q., Probing optical anisotropy of nanometer-thin van der waals microcrystals by near-field imaging. *Nat Commun* **2017**, *8* (1), 1471.
33. Ma, W.; Alonso-Gonzalez, P.; Li, S.; Nikitin, A. Y.; Yuan, J.; Martin-Sanchez, J.; Taboada-Gutierrez, J.; Amenabar, I.; Li, P.; Velez, S.; Tollan, C.; Dai, Z.; Zhang, Y.; Sriram, S.; Kalantar-Zadeh, K.; Lee, S. T.; Hillenbrand, R.; Bao, Q., In-plane anisotropic and ultra-low-loss polaritons in a natural van der Waals crystal. *Nature* **2018**, *562* (7728), 557-562.
34. Fei, Z.; Rodin, A. S.; Andreev, G. O.; Bao, W.; McLeod, A. S.; Wagner, M.; Zhang, L. M.; Zhao, Z.; Thiemens, M.; Dominguez, G.; Fogler, M. M.; Castro Neto, A. H.; Lau, C. N.; Keilmann, F.; Basov, D. N., Gate-tuning of graphene plasmons revealed by infrared nano-imaging. *Nature* **2012**, *487* (7405), 82-5.
35. Göttinger, S.; Demmerer, S.; Benson, O.; Sandoghdar, V., Mapping and manipulating whispering gallery modes of a microsphere resonator with a near-field probe. *J. Microsc.* **2001**, *202*, 117–121.
36. Balistreri, M. L. M.; Gersen, H.; Korterik, J. P.; Kuipers, L.; van Hulst, N. F., Tracking Femtosecond Laser Pulses in Space and Time. *Science* **2001**, *294*, 1080–1082.
37. Intonti, F.; Vignolini, S.; Riboli, F.; Vinattieri, A.; Wiersma, D. S.; Colocci, M.; Balet, L.; Monat, C.; Zinoni, C.; Li, L. H.; Houdré, R.; Francardi, M.; Gerardino, A.; Fiore, A.; Gurioli, M., Spectral tuning and near-field imaging of photonic crystal microcavities. *Physical Review B* **2008**, *78* (4).
38. Frolov, A. Y.; Verellen, N.; Li, J.; Zheng, X.; Paddubrouskaya, H.; Denkova, D.; Shcherbakov, M. R.; Vandenbosch, G. A. E.; Panov, V. I.; Van Dorpe, P.; Fedyanin, A. A.; Moshchalkov, V. V., Near-Field Mapping of Optical Fabry-Perot Modes in All-Dielectric Nanoantennas. *Nano Lett* **2017**, *17* (12), 7629-7637.
39. Habteyes, T. G.; Staude, I.; Chong, K. E.; Dominguez, J.; Decker, M.; Miroshnichenko, A.; Kivshar, Y.; Brener, I., Near-Field Mapping of Optical Modes on All-Dielectric Silicon Nanodisks. *ACS Photonics* **2014**, *1* (9), 794-798.
40. Kravtsov, V.; Ulbricht, R.; Atkin, J. M.; Raschke, M. B., Plasmonic nanofocused four-wave mixing for femtosecond near-field imaging. *Nat Nanotechnol* **2016**, *11* (5), 459-64.
41. Schmidt, O.; Piglosiewicz, B. r.; Sadiq, D.; Shirdel, J.; Lee, J. S.; Vasa, P.; Park, N.; Kim, D.-S.; Lienau, C., Adiabatic Nanofocusing on Ultrasoother Single-Crystalline Gold Tapers Creates a 10-nm-Sized Light Source with Few-Cycle Time Resolution. *ACS Nano* **2012**, *6*, 6040–6048.
42. Ropers, C.; Neacsu, C. C.; Elsaesser, T.; Albrecht, M.; Raschke, M. B.; Lienau, C., Grating-coupling of surface plasmons onto metallic tips: a nanoconfined light source. *Nano Lett* **2007**, *7* (9), 2784-8.

43. Neacsu, C. C.; Berweger, S.; Olmon, R. L.; Saraf, L. V.; Ropers, C.; Raschke, M. B., Near-field localization in plasmonic superfocusing: a nanoemitter on a tip. *Nano Lett* **2010**, *10* (2), 592-6.
44. Esmann, M.; Becker, S. F.; Witt, J.; Zhan, J.; Chimeh, A.; Korte, A.; Zhong, J.; Vogelgesang, R.; Wittstock, G.; Lienau, C., Vectorial near-field coupling. *Nature Nanotechnology* **2019**, *14* (7), 698-704.
45. Esmann, M.; Chimeh, A.; Korte, A.; Zhong, J.-H.; Stephan, S.; Witt, J.; Wittstock, G.; Talebi, N.; Lienau, C., Plasmonic nanofocusing spectral interferometry. *Nanophotonics* **2020**, *9* (2), 491-508.
46. Schmidt, S.; Piglosiewicz, B.; Sadiq, D.; Shirdel, J.; Lee, J. S.; Vasa, P.; Park, N.; Kim, D.-S.; Lienau, C., Adiabatic nanofocusing on ultrasmooth single-crystalline gold tapers creates a 10-nm-sized light source with few-cycle time resolution. *ACS Nano* **2012**, *6*, 6040-6048.
47. Ash, E.; Nicholls, G., Super-resolution aperture scanning microscope. *Nature* **1972**, *237*, 510-512.
48. Sasaki, Y.; Sasaki, H., Heterodyne detection for the extraction of the probe-scattering signal in scattering-type scanning near-field optical microscope. *Jpn. J. Appl. Phys.* **2000**, *39*, L321-L323.
49. Hillenbrand, R.; Knoll, B.; Keilmann, F., Pure optical contrast in scattering-type scanning near-field microscopy. *J. Microsc.* **2001**, *202*, 77-83.
50. Hillenbrand, R.; Keilmann, F., Complex optical constants on a subwavelength scale. *Phys. Rev. Lett.* **2000**, *85*, 3029-3032.
51. Hermann, P.; Hoehl, A.; Ulrich, G.; Fleischmann, C.; Hermelink, A.; Kastner, B.; Patoka, P.; Hornemann, A.; Beckhoff, B.; Ruhl, E.; Ulm, G., Characterization of semiconductor materials using synchrotron radiation-based near-field infrared microscopy and nano-FTIR spectroscopy. *Opt Express* **2014**, *22* (15), 17948-58.
52. Amenabar, I.; Poly, S.; Goikoetxea, M.; Nuansing, W.; Lasch, P.; Hillenbrand, R., Hyperspectral infrared nanoimaging of organic samples based on Fourier transform infrared nanospectroscopy. *Nat Commun* **2017**, *8*, 14402.
53. Muller, E. A.; Pollard, B.; Raschke, M. B., Infrared Chemical Nano-Imaging: Accessing Structure, Coupling, and Dynamics on Molecular Length Scales. *J Phys Chem Lett* **2015**, *6* (7), 1275-84.
54. Fei, Z.; Andreev, G. O.; Bao, W.; Zhang, L. M.; A, S. M.; Wang, C.; Stewart, M. K.; Zhao, Z.; Dominguez, G.; Thiemens, M.; Fogler, M. M.; Tauber, M. J.; Castro-Neto, A. H.; Lau, C. N.; Keilmann, F.; Basov, D. N., Infrared nanoscopy of dirac plasmons at the graphene-SiO₂ interface. *Nano Lett* **2011**, *11* (11), 4701-5.
55. Zhang, L. M.; Andreev, G. O.; Fei, Z.; McLeod, A. S.; Dominguez, G.; Thiemens, M.; Castro-Neto, A. H.; Basov, D. N.; Fogler, M. M., Near-field spectroscopy of silicon dioxide thin films. *Physical Review B* **2012**, *85* (7).

56. Liu, M.; Sternbach, A. J.; Wagner, M.; Slusar, T. V.; Kong, T.; Bud'ko, S. L.; Kittiwatanakul, S.; Qazilbash, M. M.; McLeod, A.; Fei, Z.; Abreu, E.; Zhang, J.; Goldflam, M.; Dai, S.; Ni, G.-X.; Lu, J.; Bechtel, H. A.; Martin, M. C.; Raschke, M. B.; Averitt, R. D.; Wolf, S. A.; Kim, H.-T.; Canfield, P. C.; Basov, D. N., Phase transition in bulk single crystals and thin films of VO₂ by nanoscale infrared spectroscopy and imaging. *Physical Review B* **2015**, *91* (24).
57. Wagner, M.; Fei, Z.; McLeod, A. S.; Rodin, A. S.; Bao, W.; Iwinski, E. G.; Zhao, Z.; Goldflam, M.; Liu, M.; Dominguez, G.; Thiemens, M.; Fogler, M. M.; Castro Neto, A. H.; Lau, C. N.; Amarie, S.; Keilmann, F.; Basov, D. N., Ultrafast and nanoscale plasmonic phenomena in exfoliated graphene revealed by infrared pump-probe nanoscopy. *Nano Lett* **2014**, *14* (2), 894-900.
58. Ocelic, N.; Huber, A.; Hillenbrand, R., Pseudoheterodyne detection for background-free near-field spectroscopy. *Applied Physics Letters* **2006**, *89* (10).
59. Kuznetsov, A. I.; Miroshnichenko, A. E.; Brongersma, M. L.; Kivshar, Y. S.; Luk'yanchuk, B., Optically resonant dielectric nanostructures. *Science* **2016**, *354* (6314).
60. Kruk, S.; Kivshar, Y., Functional meta-optics and nanophotonics governed by Mie resonances. *ACS Photonics* **2017**, *4* (11), 2638-2649.
61. Staude, I.; Schilling, J., Metamaterial-inspired silicon nanophotonics. *Nature Photonics* **2017**, *11* (5), 274.
62. Zhao, Q.; Zhou, J.; Zhang, F.; Lippens, D., Mie resonance-based dielectric metamaterials. *Materials today* **2009**, *12* (12), 60-69.
63. Kondrotas, R.; Chen, C.; Tang, J., Sb₂S₃ Solar Cells. *Joule* **2018**, *2* (5), 857-878.
64. Versavel, M. Y.; Haber, J. A., Structural and optical properties of amorphous and crystalline antimony sulfide thin-films. *Thin Solid Films* **2007**, *515* (18), 7171-7176.
65. Wang, W.; Pfeiffer, P.; Schmidt - Mende, L., Direct Patterning of Metal Chalcogenide Semiconductor Materials. *Advanced Functional Materials* **2020**, *30* (27).
66. Choi, Y. C.; Seok, S. I., Efficient Sb₂S₃-Sensitized Solar Cells Via Single-Step Deposition of Sb₂S₃ Using S/Sb-Ratio-Controlled SbCl₃-Thiourea Complex Solution. *Advanced Functional Materials* **2015**, *25* (19), 2892-2898.
67. Shcherbakov, M. R.; Liu, S.; Zubyuk, V. V.; Vaskin, A.; Vabishchevich, P. P.; Keeler, G.; Pertsch, T.; Dolgova, T. V.; Staude, I.; Brener, I.; Fedyanin, A. A., Ultrafast all-optical tuning of direct-gap semiconductor metasurfaces. *Nat Commun* **2017**, *8* (1), 17.
68. Sutter-Fella, C. M.; Li, Y.; Amani, M.; Ager, J. W., 3rd; Toma, F. M.; Yablonovitch, E.; Sharp, I. D.; Javey, A., High Photoluminescence Quantum Yield in Band Gap Tunable Bromide Containing Mixed Halide Perovskites. *Nano Lett* **2016**, *16* (1), 800-6.
69. Yin, W.-J.; Shi, T.; Yan, Y., Unusual defect physics in CH₃NH₃PbI₃ perovskite solar cell absorber. *Applied Physics Letters* **2014**, *104* (6).

70. deQuilettes, D. W.; Koch, S.; Burke, S.; Paranj, R. K.; Shropshire, A. J.; Ziffer, M. E.; Ginger, D. S., Photoluminescence Lifetimes Exceeding 8 μ s and Quantum Yields Exceeding 30% in Hybrid Perovskite Thin Films by Ligand Passivation. *ACS Energy Letters* **2016**, *1* (2), 438-444.
71. Osipov, A. V.; Tretyakov, S. A., *Modern electromagnetic scattering theory with applications*. Wiley 2017.
72. Nie, S.; Emory, S. R., Probing Single Molecules and Single Nanoparticles by Surface-Enhanced Raman Scattering. *Science* **1997**, *275*, 1102-1106.
73. Jäckel, F.; Kinkhabwala, A. A.; Moerner, W. E., Gold bowtie nanoantennas for surface-enhanced Raman scattering under controlled electrochemical potential. *Chemical Physics Letters* **2007**, *446* (4-6), 339-343.
74. Chan, J.; Fore, S.; Wachsmann-Hogiu, S.; Huser, T., Raman spectroscopy and microscopy of individual cells and cellular components. *Laser & Photonics Review* **2008**, *2* (5), 325-349.
75. Dykman, L.; Khlebtsov, N., Gold nanoparticles in biomedical applications: recent advances and perspectives. *Chem Soc Rev* **2012**, *41* (6), 2256-82.
76. Antonio, K. A.; Schultz, Z. D., Advances in biomedical Raman microscopy. *Anal Chem* **2014**, *86* (1), 30-46.
77. Tan, J. M.; Ruan, J. J.; Lee, H. K.; Phang, I. Y.; Ling, X. Y., A large-scale superhydrophobic surface-enhanced Raman scattering (SERS) platform fabricated via capillary force lithography and assembly of Ag nanocubes for ultratrace molecular sensing. *Phys Chem Chem Phys* **2014**, *16* (48), 26983-90.
78. Huang, J.-A.; Zhang, Y.-L.; Ding, H.; Sun, H.-B., SERS-Enabled Lab-on-a-Chip Systems. *Advanced Optical Materials* **2015**, *3* (5), 618-633.
79. Zheng, P.; Li, M.; Jurevic, R.; Cushing, S. K.; Liu, Y.; Wu, N., A gold nanohole array based surface-enhanced Raman scattering biosensor for detection of silver(I) and mercury(II) in human saliva. *Nanoscale* **2015**, *7* (25), 11005-12.
80. Alessandri, I.; Lombardi, J. R., Enhanced Raman Scattering with Dielectrics. *Chem Rev* **2016**, *116* (24), 14921-14981.
81. Gwo, S.; Wang, C.-Y.; Chen, H.-Y.; Lin, M.-H.; Sun, L.; Li, X.; Chen, W.-L.; Chang, Y.-M.; Ahn, H., Plasmonic Metasurfaces for Nonlinear Optics and Quantitative SERS. *ACS Photonics* **2016**, *3* (8), 1371-1384.
82. Taylor, A. B.; Zijlstra, P., Single-Molecule Plasmon Sensing: Current Status and Future Prospects. *ACS Sens* **2017**, *2* (8), 1103-1122.
83. Kinkhabwala, A.; Yu, Z.; Fan, S.; Avlasevich, Y.; Müllen, K.; Moerner, W. E., Large single-molecule fluorescence enhancements produced by a bowtie nanoantenna. *Nature Photonics* **2009**, *3* (11), 654-657.
84. Bharadwaj, P.; Beams, R.; Novotny, L., Nanoscale spectroscopy with optical antennas. *Chem. Sci.* **2011**, *2* (1), 136-140.

85. Giannini, V.; Fernandez-Dominguez, A. I.; Heck, S. C.; Maier, S. A., Plasmonic nanoantennas: fundamentals and their use in controlling the radiative properties of nanoemitters. *Chem Rev* **2011**, *111* (6), 3888-912.
86. Acuna, G. P.; Moller, F. M.; Holzmeister, P.; Beater, S.; Lalkens, B.; Tinnefeld, P., Fluorescence enhancement at docking sites of DNA-directed self-assembled nanoantennas. *Science* **2012**, *338*, 506-510.
87. Busson, M. P.; Rolly, B.; Stout, B.; Bonod, N.; Bidault, S., Accelerated single photon emission from dye molecule-driven nanoantennas assembled on DNA. *Nat Commun* **2012**, *3*, 962.
88. Ming, T.; Chen, H.; Jiang, R.; Li, Q.; Wang, J., Plasmon-Controlled Fluorescence: Beyond the Intensity Enhancement. *The Journal of Physical Chemistry Letters* **2012**, *3* (2), 191-202.
89. Punj, D.; Regmi, R.; Devilez, A.; Plauchu, R.; Moparthi, S. B.; Stout, B.; Bonod, N.; Rigneault, H.; Wenger, J., Self-Assembled Nanoparticle Dimer Antennas for Plasmonic-Enhanced Single-Molecule Fluorescence Detection at Micromolar Concentrations. *ACS Photonics* **2015**, *2* (8), 1099-1107.
90. Akselrod, G. M.; Weidman, M. C.; Li, Y.; Argyropoulos, C.; Tisdale, W. A.; Mikkelsen, M. H., Efficient Nanosecond Photoluminescence from Infrared PbS Quantum Dots Coupled to Plasmonic Nanoantennas. *ACS Photonics* **2016**, *3* (10), 1741-1746.
91. Kress, S. J. P.; Cui, J.; Rohner, P.; Kim, D. K.; Antolinez, F. V.; Zaininger, K.-A.; Jayanti, S. V.; Richner, P.; McPeak, K. M.; Poulikakos, D.; Norris, D. J., A customizable class of colloidal-quantum-dot spasers and plasmonic amplifiers. *Sci. Adv.* **2016**, *3*, e1700688.
92. Siraj, N.; El-Zahab, B.; Hamdan, S.; Karam, T. E.; Haber, L. H.; Li, M.; Fakayode, S. O.; Das, S.; Valle, B.; Strongin, R. M.; Patonay, G.; Sintim, H. O.; Baker, G. A.; Powe, A.; Lowry, M.; Karolin, J. O.; Geddes, C. D.; Warner, I. M., Fluorescence, Phosphorescence, and Chemiluminescence. *Anal Chem* **2016**, *88* (1), 170-202.
93. Koenderink, A. F., Single-Photon Nanoantennas. *ACS Photonics* **2017**, *4* (4), 710-722.
94. Li, J. F.; Li, C. Y.; Aroca, R. F., Plasmon-enhanced fluorescence spectroscopy. *Chem Soc Rev* **2017**, *46* (13), 3962-3979.
95. Trofymchuk, K.; Reisch, A.; Didier, P.; Fras, F.; Gilliot, P.; Mely, Y.; Klymchenko, A. S., Giant light-harvesting nanoantenna for single-molecule detection in ambient light. *Nat Photonics* **2017**, *11* (10), 657-663.
96. Khatua, S.; Paulo, P. M. R.; Yuan, H.; Gupta, A.; Zijlstra, P.; Orrit, M., Resonant Plasmonic Enhancement of Single-Molecule Fluorescence by Individual Gold Nanorods. *ACS Nano* **2014**, *8*, 4440-4449.
97. Punj, D.; Mivelle, M.; Moparthi, S. B.; van Zanten, T. S.; Rigneault, H.; van Hulst, N. F.; Garcia-Parajo, M. F.; Wenger, J., A plasmonic 'antenna-in-box' platform for enhanced single-molecule analysis at micromolar concentrations. *Nat Nanotechnol* **2013**, *8* (7), 512-6.

98. Chikkaraddy, R.; de Nijs, B.; Benz, F.; Barrow, S. J.; Scherman, O. A.; Rosta, E.; Demetriadou, A.; Fox, P.; Hess, O.; Baumberg, J. J., Single-molecule strong coupling at room temperature in plasmonic nanocavities. *Nature* **2016**, *535* (7610), 127-30.
99. Baranov, D. G.; Wersäll, M.; Cuadra, J.; Antosiewicz, T. J.; Shegai, T., Novel nanostructures and materials for strong light–matter interactions. *ACS Photonics* **2017**, *5* (1), 24-42.
100. Akselrod, G. M.; Argyropoulos, C.; Hoang, T. B.; Ciraci, C.; Fang, C.; Huang, J.; Smith, D. R.; Mikkelsen, M. H., Probing the mechanisms of large Purcell enhancement in plasmonic nanoantennas. *Nature Photonics* **2014**, *8* (11), 835-840.
101. Hoang, T. B.; Akselrod, G. M.; Mikkelsen, M. H., Ultrafast room-temperature single photon emission from quantum Dots Coupled to Plasmonic Nanocavities. *Nano Lett* **2016**, *16* (1), 270-5.
102. Straubel, J.; Filter, R.; Rockstuhl, C.; Slowik, K., Plasmonic nanoantenna based triggered single-photon source. *Physical Review B* **2016**, *93* (19), 195412.
103. Atwater, H. A.; Polman, A., Plasmonics for improved photovoltaic devices. *Nat Mater* **2010**, *9* (3), 205-13.
104. Spinelli, P.; Ferry, V. E.; van de Groep, J.; van Lare, M.; Verschuuren, M. A.; Schropp, R. E. I.; Atwater, H. A.; Polman, A., Plasmonic light trapping in thin-film Si solar cells. *Journal of Optics* **2012**, *14* (2), 024002.
105. Knight, M. W.; Sobhani, H.; Nordlander, P.; Halas, N. J., Photodetection with active optical antennas. *Science* **2011**, *332*, 702-704.
106. Zhang, S.; Bao, K.; Halas, N. J.; Xu, H.; Nordlander, P., Substrate-induced Fano resonances of a plasmonic nanocube: a route to increased-sensitivity localized surface plasmon resonance sensors revealed. *Nano Lett* **2011**, *11* (4), 1657-63.
107. Pellegrotti, J. V.; Cortés, E.; Bordenave, M. D.; Caldarola, M.; Kreuzer, M. P.; Sanchez, A. D.; Ojea, I.; Bragas, A. V.; Stefani, F. D., Plasmonic photothermal fluorescence modulation for homogeneous biosensing. *ACS Sensors* **2016**, *1* (11), 1351-1357.
108. Bohren, C. F.; Huffman, D. R., *Absorption and scattering of light by small particles*. John Wiley & Sons: New York, 1983.
109. Strutt, J. W., XV. On the light from the sky, its polarization and colour. *The London, Edinburgh, and Dublin Philosophical Magazine and Journal of Science* **2009**, *41* (271), 107-120.
110. Strutt, J. W., XXXVI. On the light from the sky, its polarization and colour. *The London, Edinburgh, and Dublin Philosophical Magazine and Journal of Science* **2009**, *41* (273), 274-279.
111. Strutt, J. W., LVIII. On the scattering of light by small particles. *The London, Edinburgh, and Dublin Philosophical Magazine and Journal of Science* **2009**, *41* (275), 447-454.
112. Mie, G., Beiträge zur Optik trüber Medien, speziell kolloidaler Metallösungen. *Ann. Phys.* **1908**, *330*, 377-445.

113. Schuller, J. A.; Brongersma, M. L., General properties of dielectric optical antennas. *Opt Express* **2009**, *17*, 24084-24095.
114. Grainger, R. G.; Lucas, J.; Thomas, G. E.; Ewen, G. B. L., Calculation of Mie derivatives. *Applied Optics* **2004**, *43*, 5386-5393.
115. Palik, E. D., *Handbook of Optical Constants of Solids*. Academic Press: 1998.
116. Johnson, P. B.; Christy, R. W., Optical constants of the noble metals. *Physical Review B* **1972**, *6* (12), 4370-4379.
117. Etchegoin, P. G.; Le Ru, E. C.; Meyer, M., An analytic model for the optical properties of gold. *J Chem Phys* **2006**, *125* (16), 164705.
118. Khurgin, J. B., Ultimate limit of field confinement by surface plasmon polaritons. *Faraday Discuss* **2015**, *178*, 109-22.
119. Khurgin, J. B., How to deal with the loss in plasmonics and metamaterials. *Nat Nanotechnol* **2015**, *10* (1), 2-6.
120. Krasnok, A.; Caldarola, M.; Bonod, N.; Alú, A., Spectroscopy and biosensing with optically resonant dielectric nanostructures. *Advanced Optical Materials* **2018**, *6* (5).
121. Tiguntseva, E. Y.; Zograf, G. P.; Komissarenko, F. E.; Zuev, D. A.; Zakhidov, A. A.; Makarov, S. V.; Kivshar, Y. S., Light-emitting halide perovskite nanoantennas. *Nano Lett* **2018**, *18* (2), 1185-1190.
122. Alù, A.; Engheta, N., Polarizabilities and effective parameters for collections of spherical nanoparticles formed by pairs of concentric double-negative, single-negative, and / or double-positive metamaterial layers. *Journal of Applied Physics* **2005**, *97* (9).
123. Luk'yanchuk, B.; Zheludev, N. I.; Maier, S. A.; Halas, N. J.; Nordlander, P.; Giessen, H.; Chong, C. T., The Fano resonance in plasmonic nanostructures and metamaterials. *Nat Mater* **2010**, *9* (9), 707-15.
124. Mitschke, F., *Fiber optics*. Springer: 2016.
125. Gloge, D., Weakly guiding fibers. *Applied Optics* **1971**, *10*, 2252-2258.
126. Carminati, R.; Sáenz, J. J., Scattering theory of bardeen's formalism for tunneling: new approach to near-field microscopy. *Phys. Rev. Lett.* **2000** *84*, 5156-5159.
127. Tersoff, J.; Hamann, D. R., Theory of the scanning tunneling microscope. *Phys Rev B Condens Matter* **1985**, *31* (2), 805-813.
128. Chicanne, C.; David, T.; Quidant, R.; Weeber, J. C.; Lacroute, Y.; Bourillot, E.; Dereux, A.; Colas Des Francs, G.; Girard, C., Imaging the local density of states of optical corrals. *Phys Rev Lett* **2002**, *88* (9), 097402.
129. Dereux, A.; Devaux, E.; Weeber, J. C.; Goudonnet, J. P.; Girard, C., Direct interpretation of near-field optical images. *Journal of Microscopy* **2000**, *202*, 320-331.

130. Binnig, G.; Rohrer, H.; Gerber, C.; Weibel, E., Surface Studies by Scanning Tunneling Microscopy. *Physical Review Letters* **1982**, *49* (1), 57-61.
131. Binnig, G.; Rohrer, H., Scanning tunneling microscopy. *Helvetica Physica Acta* **1982**, *55* 726-735.
132. Bardeen, J., Tunnelling from a many-particle point of view. *Physical Review Letters* **1961**, *6* (2), 57-59.
133. Crommie, M. F.; Lutz, C. P.; Eigler, D. M., Confinement of electrons to quantum corrals on a metal surface. *Science* **1993**, *262*, 218-220
134. Carminati, R.; Sáenz, J. J., Scattering theory of bardeen's formalism for tunneling: new approach to near-field microscopy. *Physical review letters* **2000**, *84*, 5156-5159.
135. Carminati, R.; Nieto-Vesperinas, M.; Greffet, J.-J., Reciprocity of evanescent electromagnetic waves. *J. Opt. Soc. Am. A* **1998**, *15*, 706-712.
136. Dereux, A.; Girard, C.; Weeber, J.-C., Theoretical principles of near-field optical microscopies and spectroscopies. *The Journal of Chemical Physics* **2000**, *112* (18), 7775-7789.
137. Colas Des Francs, G.; Girard, C.; Weeber, J. C.; Chicane, C.; David, T.; Dereux, A.; Peyrade, D., Optical analogy to electronic quantum corrals. *Phys Rev Lett* **2001**, *86* (21), 4950-3.
138. Carminati, R.; Cazé, A.; Cao, D.; Peragut, F.; Krachmalnicoff, V.; Pierrat, R.; De Wilde, Y., Electromagnetic density of states in complex plasmonic systems. *Surface Science Reports* **2015**, *70* (1), 1-41.
139. Glauber, R. J.; Lewenstein, M., Quantum optics of dielectric media. *Phys Rev A* **1991**, *43* (1), 467-491.
140. Babadjanyan, A. J.; Margaryan, N. L.; Nerkararyan, K. V., Superfocusing of surface polaritons in the conical structure. *Journal of Applied Physics* **2000**, *87* (8), 3785-3788.
141. Stockman, M. I., Nanofocusing of optical energy in tapered plasmonic waveguides. *Phys Rev Lett* **2004**, *93* (13), 137404.
142. Sasaki, Y.; Sasaki, H., Heterodyne Detection for the Extraction of the Probe-Scattering Signal in Scattering-Type Scanning Near-Field Optical Microscope. *Jpn. J. Appl. Phys.* **2000**, *39*, 321-323.
143. Hillenbrand, R.; Knoll, B.; Keilmann, F., Pure optical contrast in scattering-type scanning near-field microscopy. *J. Microsc.* **2001**, *202*, 77-83.
144. Esslinger, M.; Dorfmueller, J.; Khunsin, W.; Vogelgesang, R.; Kern, K., Background-free imaging of plasmonic structures with cross-polarized apertureless scanning near-field optical microscopy. *Rev Sci Instrum* **2012**, *83* (3), 033704.
145. Knoll, B.; Keilmann, F., Enhanced dielectric contrast in scattering-type scanning near-field optical microscopy. *Opt. Commun.* **2000**, *182*, 321-328
146. Ash, E. A.; Nicholls, G., Super-resolution aperture scanning microscope. *Nature* **1972**, *237*, 510-512.

147. Brauer, J.; Zhan, J.; Chimeh, A.; Korte, A.; Lienau, C.; Gross, P., In-line interferometer for broadband near-field scanning optical spectroscopy. *Opt Express* **2017**, *25* (13), 15504-15525.
148. Gomez, L.; Bachelot, R.; Bouhelier, A.; Wiederrecht, G. P.; Chang, S.-h.; Gray, S. K.; Hua, F.; Jeon, S.; Rogers, J. A.; Castro, M. E.; Blaize, S.; Stefanon, I.; Lerondel, G.; Royer, P., Apertureless scanning near-field optical microscopy: a comparison between homodyne and heterodyne approaches. *Journal of the Optical Society of America B* **2006**, *23* (5).
149. Zhan, J.; Wang, W.; Brauer, J. H.; Schmidt-Mende, L.; Lienau, C.; Groß, P., Spatial and spectral mode mapping of a dielectric nanodot by broadband interferometric homodyne scanning near-field spectroscopy. *Advanced Photonics* **2020**, *2* (04).
150. Qian, H. Tip-enhanced Near-Field Optical Spectroscopy on Single-Walled Carbon Nanotubes. Doctoral thesis, Ludwig-Maximilians-University, 2008.
151. Schmidt, S.; Piglosiewicz, B.; Sadiq, D.; Shirdel, J.; Lee, J. S.; Vasa, P.; Park, N.; Kim, D.-S.; Lienau, C., Adiabatic Nanofocusing on Ultrasoother Single-Crystalline Gold Tapers Creates a 10-nm-Sized Light Source with Few-Cycle Time Resolution. *ACS Nano* **2012**, *6* (7), 6040-6048.
152. Billot, L.; Berguiga, L.; de la Chapelle, M. L.; Gilbert, Y.; Bachelot, R., Production of gold tips for tip-enhanced near-field optical microscopy and spectroscopy: analysis of the etching parameters. *The European Physical Journal Applied Physics* **2005**, *31* (2), 139-145.
153. Ren, B.; Picardi, G.; Pettinger, B., Preparation of gold tips suitable for tip-enhanced Raman spectroscopy and light emission by electrochemical etching. *Review of Scientific Instruments* **2004**, *75* (4), 837-841.
154. Rugar, D.; Mamin, H. J.; Guethner, P., Improved fiber - optic interferometer for atomic force microscopy. *Applied Physics Letters* **1989**, *55* (25), 2588-2590.
155. Tarrach, G.; Bopp, M. A.; Zeisel, D.; Meixner, A. J., Design and construction of a versatile scanning near-field optical microscope for fluorescence imaging of single molecules. *Rev. Sci. Instrum.* **1995**, *66*, 3569-3575.
156. Betzig, E.; Finn, P. L.; Weiner, J. S., Combined shear force and near-field scanning optical microscopy. *Appl. Phys. Lett.* **1992**, *60*, 2484 ~1992.
157. Toledo - Crow, R.; Yang, P. C.; Chen, Y.; Vaez - Iravani, M., Near - field differential scanning optical microscope with atomic force regulation. *Applied Physics Letters* **1992**, *60* (24), 2957-2959.
158. Zhong, Q.; Inniss, D.; Kjoller, K.; Elings, V. B., Fractured polymer/silica fiber surface studied by tapping mode atomic force microscopy. *Surf. Sci. Lett.* **1993**, *290*, 688-692.
159. Karrai, K.; Grober, R. D., Piezo-electric tuning fork tip-sample distance control for near field optical microscopes. *Ultramicroscopy* **1995**, *61* 197-205.
160. Karrai, K.; Grober, R. D., Piezoelectric tip - sample distance control for near field optical microscopes. *Applied Physics Letters* **1995**, *66* (14), 1842-1844.

161. Qin, Y.; Reifenberger, R., Calibrating a tuning fork for use as a scanning probe microscope force sensor. *Rev Sci Instrum* **2007**, *78* (6), 063704.
162. Mooney, J.; Kambhampati, P., Get the basics right: Jacobian conversion of wavelength and energy scales for quantitative analysis of emission spectra. *The Journal of Physical Chemistry Letters* **2013**, *4* (19), 3316-3318.
163. Wang, W.; Strössner, F.; Zimmermann, E.; Schmidt-Mende, L., Hybrid solar cells from Sb₂S₃ nanoparticle ink. *Solar Energy Materials and Solar Cells* **2017**, *172*, 335-340.
164. Choi, Y. C.; Lee, Y. H.; Im, S. H.; Noh, J. H.; Mandal, T. N.; Yang, W. S.; Seok, S. I., Efficient Inorganic-Organic Heterojunction Solar Cells Employing Sb₂(S_x/Se_{1-x})₃ Graded-Composition Sensitizers. *Advanced Energy Materials* **2014**, *4* (7).
165. Wang, G.; Wang, S.; Cui, Y.; Pan, D., A Novel and Versatile Strategy to Prepare Metal–Organic Molecular Precursor Solutions and Its Application in Cu(In,Ga)(S,Se)₂ Solar Cells. *Chemistry of Materials* **2012**, *24* (20), 3993-3997.
166. Wang, X.; Li, J.; Liu, W.; Yang, S.; Zhu, C.; Chen, T. J. N., A fast chemical approach towards Sb₂S₃ film with a large grain size for high-performance planar heterojunction solar cells. *Nanoscale* **2017**, *9* (10), 3386-3390.
167. Knoll, B.; Keilmann, F., Enhanced dielectric contrast in scattering-type scanning near-field optical microscopy. *Optics communications* **2000**, *182* (4-6), 321-328.
168. Buchler, B.; Kalkbrenner, T.; Hettich, C.; Sandoghdar, V., Measuring the quantum efficiency of the optical emission of single radiating dipoles using a scanning mirror. *Phys. Rev. Lett.* **2005**, *95* (6), 063003.
169. Castanié, E.; Krachmalnicoff, V.; Cazé, A.; Pierrat, R.; De Wilde, Y.; Carminati, R., Distance dependence of the local density of states in the near field of a disordered plasmonic film. *Opt. Lett.* **2012**, *37* (14), 3006-3008.
170. Zhang, Z.; Satpathy, S., Electromagnetic wave propagation in periodic structures: Bloch wave solution of Maxwell's equations. *Phys. Rev. Lett.* **1990**, *65* (21), 2650.
171. Grésillon, S.; Aigouy, L.; Boccara, A.; Rivoal, J.; Quelin, X.; Desmarest, C.; Gadenne, P.; Shubin, V.; Sarychev, A.; Shalaev, V. M., Experimental observation of localized optical excitations in random metal-dielectric films. *Phys. Rev. Lett.* **1999**, *82* (22), 4520.
172. Zhong, J.; Chimeh, A.; Korte, A.; Schwarz, F.; Yi, J.; Wang, D.; Zhan, J.; Schaaf, P.; Runge, E.; Lienau, C., Strong Spatial and Spectral Localization of Surface Plasmons in Individual Randomly Disordered Gold Nanosponges. *Nano Lett* **2018**, *18* (8), 4957-4964.
173. Dmitriev, P. A.; Makarov, S. V.; Milichko, V. A.; Mukhin, I. S.; Gudovskikh, A. S.; Sitnikova, A. A.; Samusev, A. K.; Krasnok, A. E.; Belov, P. A., Laser fabrication of crystalline silicon nanoresonators from an amorphous film for low-loss all-dielectric nanophotonics. *Nanoscale* **2016**, *8* (9), 5043-8.

174. Jeon, N. J.; Noh, J. H.; Kim, Y. C.; Yang, W. S.; Ryu, S.; Seok, S. I., Solvent engineering for high-performance inorganic-organic hybrid perovskite solar cells. *Nat Mater* **2014**, *13* (9), 897-903.
175. Permyakov, D.; Sinev, I.; Markovich, D.; Ginzburg, P.; Samusev, A.; Belov, P.; Valuckas, V.; Kuznetsov, A. I.; Luk'yanchuk, B. S.; Miroshnichenko, A. E.; Neshev, D. N.; Kivshar, Y. S., Probing magnetic and electric optical responses of silicon nanoparticles. *Applied Physics Letters* **2015**, *106* (17).
176. Phillips, L. J.; Rashed, A. M.; Treharne, R. E.; Kay, J.; Yates, P.; Mitrovic, I. Z.; Weerakkody, A.; Hall, S.; Durose, K., Dispersion relation data for methylammonium lead triiodide perovskite deposited on a (100) silicon wafer using a two-step vapour-phase reaction process. *Data Brief* **2015**, *5*, 926-8.
177. Brittnan, S.; Garnett, E. C., Measuring n and k at the Microscale in Single Crystals of $\text{CH}_3\text{NH}_3\text{PbBr}_3$ Perovskite. *The Journal of Physical Chemistry C* **2015**, *120* (1), 616-620.
178. Rybin, M. V.; Kapitanova, P. V.; Filonov, D. S.; Slobozhanyuk, A. P.; Belov, P. A.; Kivshar, Y. S.; Limonov, M. F., Fano resonances in antennas: General control over radiation patterns. *Physical Review B* **2013**, *88* (20).
179. Limonov, M. F.; Rybin, M. V.; Poddubny, A. N.; Kivshar, Y. S., Fano resonances in photonics. *Nature Photonics* **2017**, *11* (9), 543-554.
180. Iizawa, M.; Kosugi, S.; Koike, F.; Azuma, Y., The quantum and classical Fano parameter q . *Physica Scripta* **2021**, *96* (5).
181. Ott, C.; Kaldun, A.; Raith, P.; Meyer, K.; Laux, M.; Evers, J.; Keitel, C. H.; Greene, C. H.; Pfeifer, T., Lorentz Meets Fano in Spectral Line Shapes: A Universal Phase and Its Laser Control. *Science* **2013**, *340* (6133), 5.
182. Tiguntseva, E. Y.; Baranov, D. G.; Pushkarev, A. P.; Munkhbat, B.; Komissarenko, F.; Franckevicius, M.; Zakhidov, A. A.; Shegai, T.; Kivshar, Y. S.; Makarov, S. V., Tunable hybrid fano resonances in halide perovskite nanoparticles. *Nano Lett* **2018**, *18* (9), 5522-5529.
183. M. Kerker; D. S. Wang; Giles, C. L., Electromagnetic scattering by magnetic spheres. *J. Opt. Soc. Am.* **1983**, *73*, 3.
184. Liu, W.; Kivshar, Y. S., Generalized Kerker effects in nanophotonics and meta-optics [Invited]. *Opt Express* **2018**, *26* (10), 13085-13105.
185. Zhou, Z.-X.; Ye, M.-J.; Yu, M.-W.; Yang, J.-H.; Su, K.-L.; Yang, C.-C.; Lin, C.-Y.; Babicheva, V. E.; Timofeev, I. V.; Chen, K.-P., Germanium Metasurfaces with Lattice Kerker Effect in Near-Infrared Photodetectors. *ACS Nano* **2022**.
186. Franceschini, P.; Carletti, L.; Pushkarev, A. P.; Preda, F.; Perri, A.; Tognazzi, A.; Ronchi, A.; Ferrini, G.; Pagliara, S.; Banfi, F.; Polli, D.; Cerullo, G.; De Angelis, C.; Makarov, S. V.; Giannetti, C., Tuning the Ultrafast Response of Fano Resonances in Halide Perovskite Nanoparticles. *ACS Nano* **2020**, *14* (10), 13602-13610.

187. Ogut, B.; Talebi, N.; Vogelgesang, R.; Sigle, W.; van Aken, P. A., Toroidal plasmonic eigenmodes in oligomer nanocavities for the visible. *Nano Lett* **2012**, *12* (10), 5239-44.

List of Publications

1. **Jinxin Zhan**, Wei Wang, Jens Brauer, Lukas Schmidt-Mende, Christoph Lienau, and Petra Groß. (2020) Spatial and spectral mode mapping of a dielectric nanodot by broadband interferometric homodyne scanning near-field spectroscopy. *Advanced Photonics*
2. Martin Esmann, Simon Fabian Becker, ulia Witt, **Jinxin Zhan**, Abbas Chimeh, Anke Korte, Jinhui Zhong, Ralf Vogelgesang, Gunther Wittstock and Christoph Lienau. (2019) Vectorial near-field coupling. *Nature Nanotechnology*
3. Jinhui Zhong, Abbas Chimeh, Anke Korte, Felix Schwarz, Juemin Yi, Dong Wang, **Jinxin Zhan**, Peter Schaaf, Erich Runge, and Christoph Lienau. (2018) Strong Spatial and Spectral Localization of Surface Plasmons in Individual Randomly Disordered Gold Nanosponges
4. Jens Brauer, **Jinxin Zhan**, Abbas Chimeh, Anke Korte, Christoph Lienau, and Petra Gross. (2017) In-line interferometer for broadband near-field scanning optical spectroscopy. *Optical Express*
5. **Jinxin Zhan**, Hongxing Dong, Shulin Sun, Xiaodong Ren, Jianjun Liu, Zhanghai Chen, Christoph Lienau , and Long Zhang. (2015) Surface-Energy-Driven Growth of ZnO Hexagonal Microtube Optical Resonators. *Advanced Optical Materials*

Conferences

- (2019) Talk 'Near field spectroscopy on a Sb_2S_3 nanodot' in Dresden, Deutsche Physikalische Gesellschaft Annual Meeting. Regensburg
- (2018) Poster 'Local near-field spectroscopy of squaraine J-aggregates', Surface Micro-Spectroscopy and Spectro-Microscopy of Electrical Phenomena: Advanced methodologies for nano-characterization of electronic surface phenomena. Rehovot Israel
- (2018) Talk 'Local spectroscopy of squaraine J-aggregates' in Dresden, Deutsche Physikalische Gesellschaft Annual Meeting. Berlin
- (2017) Poster 'Polymer Orientation Sensitive Scanning Near-field Optical Microscopy' in Dresden, Deutsche Physikalische Gesellschaft Annual Meeting. Dresden

Acknowledgements

I want to express my gratitude to Prof. Christoph Lienau, group leader of the Ultrafast Nano-Optics (UNO) at University Oldenburg, for supervising my thesis. I thank him for guiding me to understand the physics behind optical phenomena, encouraging me to discuss and cooperate with other group members.

I thank Priv.-Doz. Dr. Petra Gross, for her help to carry out my experiments in the scanning near-field optical microscopy and spectroscopy, for teaching me scientific presenting and writing in my PhD project. I am thankful to all members in the 'SNOM lab', including Dr. Jens Bauer, Dr. Martin Esmann, Dr. Anke Korte, Dr. Abbas Chimeh, Tom Jehle, and Sam Steven Nochowicz for valuable discussions and experimental cooperation. Special thanks to my work partner Dr. Jens Brauer, for working together on the 'In-line interferometer SNOM' establishing in the first three years of my PhD project.

I want to thank all members of UNO, for providing a great environment to conduct scientific work. Especially I want to thank Sven Stephan and Vladimir Smirnov for great theoretical and to Dipl.-Phys. Raimond Angermann for technical support.

I want to thank all collaborators, especially Dr. Wei Wang, Prof. Lukas Schmidt-Mende, Dr. Ekaterina Y. Tiguntseva, Prof. Sergey Makarov who contributed to the projects within this thesis.

Finally, I want to thank my family and husband Wei Wang for all the support before and during this thesis, my mother in law who took care of my daughter while I managed to finalize this thesis, and my daughter who gives me the chance to experience new beauty in my life.

Selbstständigkeitserklärung

Hiermit versichere ich, dass ich die vorliegende Arbeit selbstständig verfasst und nur die angegebenen Hilfsmittel verwendet habe. Außerdem versichere ich, dass ich die allgemeinen Prinzipien wissenschaftlicher Arbeit und Veröffentlichung, wie sie in den Leitlinien guter wissenschaftlicher Praxis der Carl von Ossietzky Universität Oldenburg festgelegt sind, befolgt habe.

Oldenburg, den

.....

(Jinxin Zhan)